Turbulence, Sediment Transport, Erosion, and Sandbar Beach Failure Processes

In Grand Canyon

by

Laura Verónica Alvarez Rueda

A Dissertation Presented in Partial Fulfillment
of the Requirements for the Degree
Doctor of Philosophy

Approved April 2015 by the
Graduate Supervisory Committee:

Mark W. Schmeeckle, Chair
Ronald I. Dorn
Anthony J. Brazel
Paul E. Grams
David J. Topping

ARIZONA STATE UNIVERSITY

May 2015

ABSTRACT

This research examines lateral separation zones and sand bar slope stability using two methods: a parallelized turbulence resolving model and full-scale laboratory experiments. Lateral flow separation occurs in rivers where banks exhibit strong curvature, for instance canyon rivers, sharp meanders and river confluences. In the Colorado River, downstream Glen Canyon Dam, lateral separation zones are the principal storage of sandbars. Maximum ramp rates have been imposed to Glen Canyon Dam operation to minimize mass loss of sandbars. Assessment of the effect of restricting maximum ramp rates in bar stability is conducted using multiple laboratory experiments. Results reveal that steep sandbar faces would rapidly erode by mass failure and seepage erosion to stable slopes, regardless of dam discharge ramp rates. Thus, continued erosion of sand bars depends primarily of turbulent flow and waves. A parallelized, three-dimensional, turbulence resolving model is developed to study flow structures in two lateral separation zones located along the Colorado River in Grand Canyon. The model employs a Detached Eddy Simulation (DES) technique where variables larger than the grid scale are fully resolved, while Sub-Grid-Scale (SGS) variables are modeled. The DES-3D model is validated using ADCP flow measurements and skill metric scores show predictive capabilities of simulated flow. The model reproduces the patterns and magnitudes of flow velocity in lateral recirculation zones, including size and position of primary and secondary eddy cells and return current. Turbulence structures with a predominately vertical axis of vorticity are observed in the shear layer, becoming three-dimensional without preferred orientation downstream. The DES-3D model is coupled with a sediment advection-diffusion formulation, wherein advection is provided by the

DES velocity field minus particles settling velocity, and diffusion is provided by the SGS. Results show a lateral recirculation zone having a continuous export and import of sediment from and to the main channel following a pattern of high frequency pulsations of positive deposition fluxes. These high frequency pulsations play an important role to prevent an oversupply of sediment within the lateral separation zones. Improved predictive capabilities are achieved with this model when compared with previous two- and three-dimensional quasi steady and steady models.

DEDICATION

To my husband Hernan for the long hours of patience, help and love during this endeavor. To my family in Colombia and their noble support in pursue of my happiness.

ACKNOWLEDGMENTS

I want to express gratitude to my supervisor, Prof. Mark Schmeeckle who was abundantly helpful and offered invaluable assistance, support and guidance. Deepest gratitude to the members of my PhD committee, Prof. Ronald Dorn, Prof. Anthony Brazel, Dr. Paul Grams and Dr. David Topping, whose knowledge and assistance helped the good course of my research studies.

I acknowledge Scott Wright from U.S. Geological Survey, Sacramento, California, Matt Kaplinski and Joseph Hazel from Northern Arizona University, and David Topping and Tom Sabol for providing field survey data. The data was provided upon personal request.

I thank to the Grand Canyon Monitoring and Research Center, Arizona State University's Graduate College Dissertation Fellowship and the School of Geographical Sciences and Urban Planning at Arizona State University for funding this doctoral thesis.

Finally I want to express my deepest gratitude to my beloved husband Hernan Alonso whose support and constructive feedback has been essential for my professional career. To my family members in Colombia, Jenny, Carlos Mario, John Jairo, Miguel Angel and Raquel for believing that my dreams can become a reality.

TABLE OF CONTENTS

Page

CHAPTER Page

LIST OF TABLES

LIST OF FIGURES

Figure Page

Figure Page

Figure Page

Figure Page

Figure Page

CHAPTER 1

INTRODUCTION AND BACKGROUND

Rivers are essential features of the landscape that provide natural water resources and habitat for aquatic and riverine ecosystems. The current state of knowledge of fluvial geomorphology has proven difficulties to accurately predict river morphologic changes. Many rivers, particularly in the Western United States have been dammed producing extensive changes in riverine environments (Howard and Dolan 1981; Beus et al.1992; Schmidt et al. 1995; Schmidt et al. 1998). As a result, their geomorphology, sediment balances, riparian vegetation, fisheries habitat and river ecosystem services have been largely impacted (Turner and Karpiscak 1980; Dodrill et al. 2015). Sustainable management of rivers requires substantial enhancement of theoretical and modeling abilities. Some research studies elucidate that explicit representation of turbulence structures can become a key factor to estimate instantaneous changes in flow field and suspended sediment and, therefore, changes in river channel morphology (Zedler and Street 2001; Cao and Carling 2002; Nelson et al. 2003; Tseng and Ferziger 2004; Keylock et al. 2005; Passalacqua et al. 2006; Kirkil et al. 2009; Keylock et al. 2011; Keylock et al. 2012). This doctoral study investigates the turbulence, sediment transport, erosion and sandbar beach failure processes in regulated rivers by means of turbulence resolving models and full-scaled laboratory experiments.

The lower Colorado River, downstream the Glen Canyon Dam, spanning along the Marble and Grand Canyons has been chosen as the study area for its complex river morphology, ecological and economical values. The Glen Canyon Dam, located in northern Arizona, was commissioned by the Colorado River Storage Project Act of 1956.

Operation of the dam, since 1963, has the primary purpose of water supply to the states of California, Arizona, Nevada and has a major contribution of hydroelectric power. However, benefits on hydroelectric and water use have come with significant environmental cost (U.S Department of the Interior 1988 and 1995). Closure of the dam eliminated sediment supplied from the upper Colorado River Basin, reducing the mean annual supply of fine-sediment in Grand Canyon by 81% to 85% (Topping et al. 2000a and Topping 2000b). Two tributaries, the Paria River and Little Colorado River are the only significant sources of fine sediment to the Colorado River in Grand and Marble Canyons after the closure of the dam (Schmidt and Graf 1990; Schmidt et al.1998; Topping et al. 2000a). As a consequence, post-dam conditions have led to erosion of sandbars (Kearsley et al. 1994; Cluer 1995; Webb et al. 2002; Hazel et al. 2006b).

The Glen Canyon Dam Adaptive Management Program (GCDAMP), established in 1995 to advise the United States Department of Interior on the operation of Glen Canyon Dam (U.S Department of the Interior 1996), considers sandbars to be an important resource. Sandbars may possibly play a role in the habitat of native endangered fish species, such the Humpback Chub Gila Cypha, providing return back waters for their subsistence (Dodrill et al. 2014; Gerig et al. 2014). Likewise, sandbars are the substrate for riparian vegetation (Turner and Karpiscak 1980) and the aeolian source of fine sediment for the preservation of archaeological sites (Draut and Rubin 2008). These bars are also cultural ecosystem services used for tourist as campsites (Kearsley et al. 1994). Sandbars can erode by a combination of seepage erosion, mass failure, and removal of sediment at the toe of the slope by turbulent flow (Beus et al. 1992). The laboratory experiments conducted in this thesis have the purpose to study the mass failures and

seepage erosion of sandbar faces due to flow stage fluctuations induced by dam operation criteria.

This thesis also combines the experimental work with numerical modeling. The gist of the numerical modeling component is the development and application of a parallelized, three-dimensional, turbulence resolving model coupled with a continuum formulation of suspended sediment, at the scale of a river-reach, to study lateral separation zones which are characterized by large scale flow separation, strong recirculation zones and free shear layers. One of the gaps in the scientific knowledge of numerical models in river system is the low predictive capabilities of traditional numerical models in complex river settings (Zedler and Street 2001; Tseng and Ferziger 2004; Keylock et al. 2005; Kirkil et al. 2009; Keylock et al. 2012).

A number of two- and three-dimensional models are currently available to estimate flow, sediment transport and channel change in rivers. Depth-averaged, two dimensional models typically rely on simple closures relating boundary stress to roughness and depth-averaged velocity. Two-and three-dimensional steady and quasi-steady fluvial models operate by using time-averaged or ensemble time-averaged time derivatives at scales greater than an integral-time scale. The studies of Nikora et al. (2007) and Sinha et al. (1998) exemplify these steady and quasi-steady models. In relatively simple channels these models have good predictive capabilities, but they can perform poorly in river channel changes featured by lateral separation zones (Cao and Carling 2002; Nelson et al. 2003; Keylock et al. 2012). Canyon rivers, sharp meanders, river confluences, channel constrictions, some engineering structures, vegetation and, certain types of bedforms all cause flow separation, secondary recirculation and free

shear layers (Best 1988; Schmidt 1990; Rhoads and Kenworthy 1995; Bradbrook et al. 2000a; Sukhodolov et al. 2002; Ferguson et al. 2003; Van Balen et al. 2010; Chang et al. 2013). A turbulence resolving model may predict, with better fidelity, turbulence structures and sediment transport in complex river systems, but at a substantially larger computational cost. With parallelization, turbulence-resolving models can now be developed and applied to challenging fluvial morphodynamic problems (Keylock et al. 2005).

A turbulence resolving model is developed and tested in two lateral separation zones located in two pools, Eminence Break (EM) and Willie Taylor (WT), along the Colorado River in Grand Canyon. This turbulence-resolving model has been developed to enhance and improve the simulation of turbulent flow and sediment supply in the eddy zone. Other two-and three dimensional quasi-steady and steady flow and sediment models have been tested and assessed using multi-beam surveys in the same lateral separation zones (EM and WT). These models have shown predictability of erosion at the river axis (thalweg) but they have not achieved enough predictive capabilities in the lateral recirculation zones resulting in over-supply of sediment within the primary eddy (Sloff et al. 2009; Logan et al. 2010; Sloff et al. 2012). Models applied to Grand Canyon separation zones generally predict greater deposition and less erosion than is observed. One reason is that these models operate by solving the flow field using time or ensemble-time averaged equations, missing to reproduce the unsteady eddy vortices (Cao and Carling 2002; Keylock et al. 2005), which play a fundamental role in turbulent flow and sediment transport in lateral separation zones.

A Detached Eddy Simulation (DES) technique is employed in this turbulence resolving model. Numerical methods based on DES techniques can have better predictive capabilities since they resolve time-dependent eddy vortices. DES is a hybrid between Reynold Averaged Navier Stokes (RANS) equations and Large Eddy Simulation (LES) technique. RANS is applied to the near-bed grid cells, where grid resolution is not sufficient to fully resolve wall turbulence. LES is applied further from the bed and banks and can integrate the spatially-filtered Navier-Stokes equations where eddies larger than the grid scale are fully resolved, while Sub-Grid Scale (SGS) eddies are modeled. The rough wall extension of the Spalart Allmaras (S-A) turbulence closure model is used to model the unresolved SGS stress tensor (Ferziger 1976; Ferziger and Peric 2002, Aupoix and Spalart 2003). The S-A model has the advantage of being a non-zonal technique implying that one single momentum equation is used with no *a priori* declaration of RANS versus LES zones (Squires 2004).

This doctoral study also addresses the evaluation of the performance of this parallelized, three-dimensional, Detached Eddy Simulation (DES-3D) model of flow and sediment at a scale of a river-reach. Some studies have applied DES and LES techniques, but most of the work has been developed at the scale of a laboratory set up (Bradbrook et al., 2000a; Zedler and Street 2001; Tseng and Ferziger 2004; Constantinescu et al. 2011a; Keylock et al. 2011; Keylock et al. 2012; Papanicolaou et al. 2012). Few fluvial models based on DES or LES have been developed at the scale of a river reach. Some of these field-scale DES or LES models have been applied to the study of meandering rivers (Kang and Sotiropoulos 2011), stream confluences (Constantinescu et al. 2011b) and flow around a circular pier (Kirkil et al. 2009).

In summary, the general objective of this thesis is to achieve a better understanding of turbulent flow patterns and how their behavior is related to sediment fluxes and sandbar failures. This is one of the first field-scale turbulence resolving models developed, validated and applied to the study of lateral separation zones. This study also recognizes the importance of sandbars and their ecological and economical values. Thus, a precise understanding of erosion processes of sandbars is a principal component of this research.

The content of this thesis is structured in five chapters. Chapters 2 to 4 correspond to either published, submitted or in preparation articles whose titles and authors appear below:

Chapter 2: Alvarez, L.V., Schmeeckle, M.W., 2013. Erosion of river sandbars by diurnal stage fluctuation in the Colorado River in the Marble and Grand Canyons: full-scale laboratory experiments, River Res. Applic. 29, 839-854, doi: 10.1002/rra.2576.

Chapter 3: Alvarez, L.V., Schmeeckle, M.W., Grams, P.E., (submitted). Turbulence resolving modeling of lateral separation zones along a large canyon-bound river using Detached Eddy Simulation technique, J. Geophys. Res.

Chapter 4: Alvarez, L.V., Schmeeckle, M.W., Grams, P.E., (in preparation). Concentration of suspended sediment modeling of lateral separation zones using the Dettached Eddy Simulation technique at the scale of a river-reach.

Chapter 5 presents a synthesis of the preceding chapters and provides insights of future work.

CHAPTER 2

EROSION OF RIVER SANDBARS BY DIURNAL STAGE FLUCTUATIONS IN THE COLORADO RIVER IN MARBLE AND GRAND CANYONS: FULL-SCALE LABORATORY EXPERIMENTS

INTRODUCTION

The stability of river banks and emergent bars is an important determinant of channel width (Darby and Thorne 1996) and pattern (Schumm and Khan 1972). River bar and bank stability also influences the downstream delivery of contaminants (Malmon et al. 2005), the concentration of fine sediments and turbidity (Green et al. 1999), and riparian vegetation patterns and biodiversity (Piégay et al. 2000). Thus, it is essential to consider the major sources of bank instability in the management of rivers. One source of bank instability, considered in this study, is the fluctuation of river stage. River stage fluctuations can be caused by changes to the input of water to the river system, such as by snowmelt or rain. In some rivers, stage fluctuations are the result of the operation of human-built river structures, such as dams. Hydroelectric dams operated for daily peak demand of electricity often generate diurnal downstream stage fluctuations (Ray and Sarma 2010). The water table in river banks and emergent bars is often at a higher elevation than the river stage during rapid reduction in stage. This condition of an elevated water table leads to elevated pore pressures and exfiltration of water. Elevated pore pressures destabilize the banks and bars, and exfiltration can cause seepage erosion (Darby et al. 2007).

Glen Canyon Dam, located in northern Arizona, was commissioned by the Colorado River Storage Project Act of 1956 with the primary purpose of water storage

for Upper Basin States of the Colorado River Compact of 1922. Hydroelectric power generation was authorized in the act as a secondary, or incident, purpose to water storage. Operation of Glen Canyon Dam, since 1963, has caused erosion of fine-grained (sand, silt, and clay) alluvial deposits (Schmidt and Graf 1990; Kearsley et al. 1994; Cluer 1995; Webb et al. 2002; Hazel et al. 2006b). Closure of the dam eliminated sediment supplied from the upper Colorado River Basin, reducing the mean annual supply of fine-sediment in Grand Canyon by 81% to 85% (Topping et al. 2000b). Two tributaries, the Paria River and Little Colorado River, are the only significant post-dam sources of fine sediment to the Colorado River in Grand and Marble Canyons (Schmidt and Graf 1990; Schmidt et al. 1998; Topping et al. 2000a; Topping et al. 2000b). Furthermore, seasonal flow variability was largely replaced by daily discharge fluctuation cycles. As a consequence, the magnitude, frequency and duration of floods decreased (Howard and Dolan 1981; Schmidt et al. 1998; U.S Department of the Interior 2005; Wright et al. 2010).

Sandbars in Grand Canyon primarily occur in lateral separation eddies downstream of channel constrictions caused by tributary debris flow fans (Leopold 1969; Schmidt 1990). Most bars are formed in the vicinity of the points of separation and reattachment. These bars are primarily composed of sand but may contain small proportions of clay, silt and gravel. Prior to construction of Glen Canyon Dam in 1963, fine sediment supply followed a seasonal pattern (Howard and Dolan 1981; Topping et al. 2000a). The unregulated Colorado River in Grand Canyon had annual maximum daily flows values around 2265 m^3/s and minimum typically below 85 m^3/s. Peak discharges usually occurred in the spring snowmelt season from the Rocky Mountains (U.S Department of the Interior 2005) and carried the majority of the fine sediment. Mean

peak annual discharge was approximately 2600 m^3/s and mean annual suspended sediment load recorded near Grand Canyon was 83 ± 4 million tons/year (metric tons) during the period of 1949 to 1962 (Rubin et al. 1998; Schmidt et al. 1998; Topping et al. 2000b).

A significant monitoring and research effort has focused on the preservation and rehabilitation of the Colorado River ecosystem in Marble and Grand Canyons. The Glen Canyon Dam Adaptive Management Program (GCDAMP), established in 1995 to advise the United States Department of Interior on operation of Glen Canyon Dam (U.S Department of the Interior 1996), considers sandbars to be an important resource. Among the most substantial benefits is their capability to provide habitat for native fish species, especially the Humpback chub (*Gila cypha*), which is listed as endangered by the United States Fish and Wildlife Service (Converse et al. 1998; Korman et al. 2004). The sandbars also serve as the substrate of riparian vegetation (Turner and Karpiscak 1980), as an aeolian source of fine sediment that preserves archaeological sites (Hereford et al. 1993; Draut and Rubin 2008) and as campsites for river rafters (Kearsley et al. 1994). Three high flow experiments (HFE) have been conducted downstream of Glen Canyon dam, in part to research the efficacy of high flows to restore sandbars (Melis 2011). All three HFEs were successful in increasing the area and volume of sandbars above the lowest normal dam operation stage, but rapid sandbar erosion under normal dam operation was measured following these experiments (Hazel et al. 2010).

Sandbars are thought to erode by a combination of seepage erosion, mass failure, and turbulent sediment transport within the water column (Beus et al. 1992) that is often enhanced by water waves (Bauer and Schmidt 1993). Herein term seepage erosion is used

to encompass the erosion of sediment by water which exfiltrates from, and subsequently flows over, the bar face. The seepage flow cuts rills and rivulets into the bar surface as it entrains and transports sediment. The exfiltration of water is believed to enhance the entrainment of sediment by the surface flow; indeed, liquefaction occurs when the vertical seepage forces balance the weight of the overlying soil column (Major and Iverson 1999). The processes of seepage erosion, mass failure, and turbulent sediment transport interact. Erosion by turbulent flow and waves at the foot of sandbars may undercut and steepen sandbar faces, which in turn increases mass failure and seepage erosion (Bauer and Schmidt 1993). Our approach is to investigate these processes separately, and to combine the processes in future research after there is predictive ability of each process in isolation. In this study the processes of seepage erosion and mass failure induced by stage fluctuations are investigated.

HISTORICAL AND MLFF RAMP RATES

The policies for operation of Glen Canyon Dam have been adapted according to scientific findings on negative impacts on Colorado River resources during the last three decades. From 1964 to 1991, Glen Canyon Dam was operated to supply electricity at peak demand. Maximum historical releases ranged up to 892 m^3/s, and ramp rates were unrestricted, resulting in large river stage fluctuations downstream of the dam (U.S Department of the Interior 1995). The Glen Canyon Environmental Studies Report (U.S. Department of the Interior 1988) concluded that these large stage fluctuations were eroding sandbars and deteriorating the downstream ecosystem. Subsequently, the Grand Canyon Protection Act of 1992, passed by the US Congress and signed into law by US President George H.W. Bush, ordered the Department of Interior to prepare an

environmental impact statement, and to maintain interim operating criteria, adopted in 1991, while the environmental impact statement was prepared. This interim dam operating regime limited flows to range between 141.5 and 566 m^3/s. In February 1997, the Modified Low Fluctuating Flow (MLFF) operation criteria of the Environmental Impact Statement's Record of Decision (U.S Department of the Interior 1995; U.S Department of the Interior 1996) were implemented. Minimum releases were constrained to 226.5 m^3/s by day and 141.5 m^3/s by night, maximum releases to 708 m^3/s and maximum daily fluctuations within 24 hours to 226.5 m^3/s. Discharge ramp rates were confined to113 cm/h and 42.5 m^3/s along the rising and falling limbs respectively (U.S. Department of the Interior 2008). The experiments reported here are intended to assess whether these maximum ramp rates imposed on Glen Canyon Dam operations are necessary and/or sufficient to minimize mass loss in Grand Canyon sandbars due to mass failure and seepage erosion.

The current Record of Decision (U S Department of the Interior 1996) imposes restrictions on dam discharges, but local variations in the water surface elevation (i.e. river stage) drive mass failure and seepage erosion. Here historical discharge variations are translated into stage variations at individual sandbars to determine an envelope of stage ramp rates for our laboratory experiments. Analysis of upramp rates is excluded since seepage erosion is unlikely to occur during the rising river phase (Beus et al. 1992). In contrast, the downramp phase (i.e. decreasing stage) has been found to be one of the primary factors that induce seepage erosion (Budhu and Gobin 1994).

Stage fluctuations are evaluated at the 47 sites downstream of Glen Canyon Dam in the study of stage-discharge relations of Hazel et al. (2006a) (see Figure 2.1, Figure 2.2).

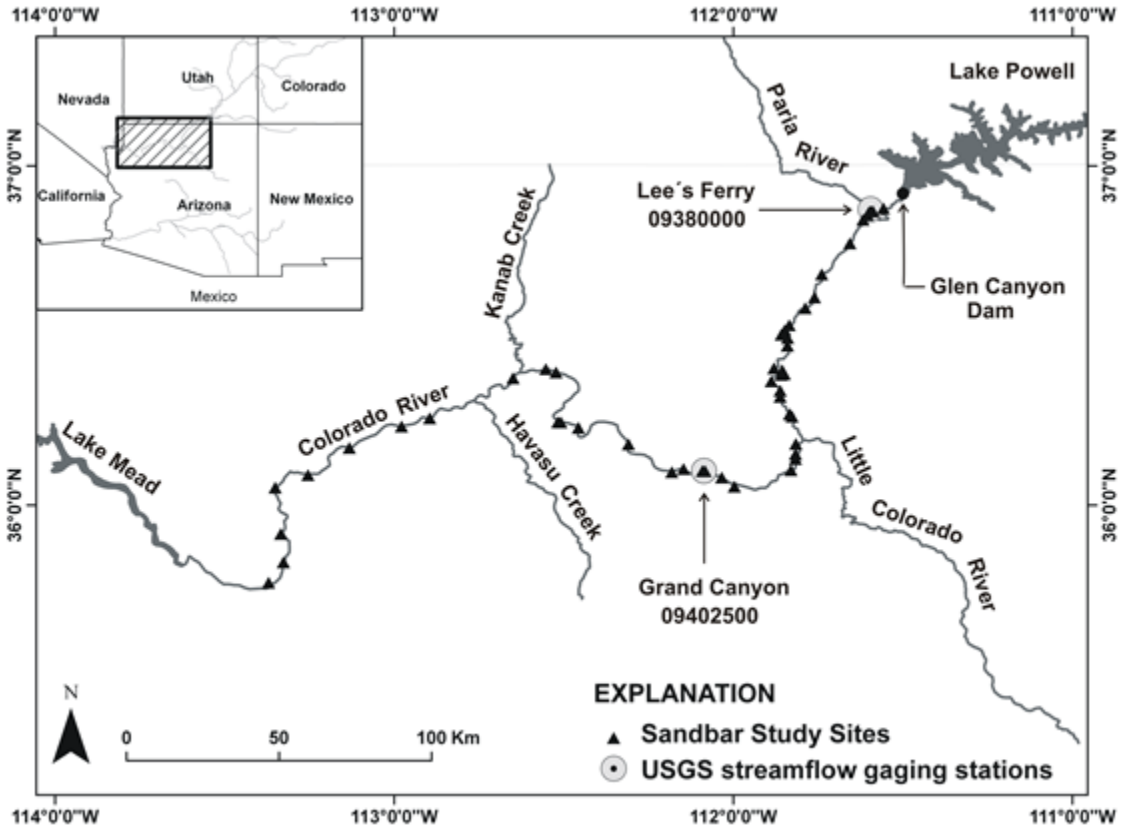

Figure 2.1. Map of the Colorado River and major tributaries between Lake Powell and Lake Mead. Shown are the sites surveyed by U.S. Geological Survey and Northern Arizona University (Hazel et al. 2006a) and U.S. Geological Survey gauging stations identify by ID number.

These sites extend from the dam to River Mile 225.5. The first site is located between the dam and Lees Ferry, sites 2 to 22 are located in Marble Canyon between the Paria River confluence and the Little Colorado confluence, and sites 23 to 47 are in Grand Canyon between the Little Colorado River and Diamond Creek confluences. Through the canyons, the river longitudinal profile is characterized by steep rapids in

shallow areas followed by flat pools in deep zones (Leopold 1969). Rapids are formed at channel constrictions caused by tributary debris fans. Recirculation zones (or eddies) typically form downstream of the rapids. Eddy sandbars are deposited in these recirculation zones along the channel margin (Schmidt and Graf 1990).

Figure 2.2. Downstream view of 30.8 RM sandbar, site code 9. The newly deposited sandbar slope shown is 26 degrees.

The method to estimate stage ramp rates from historical time series is as follows: (1) maximum and minimum discharge peaks are identified from instantaneous stream flow records gathered at Lees Ferry and Grand Canyon gauging stations during the period of 1988 to 2009;(2) Maximum and minimum discharges are used to estimate river stage at each study bar using stage-discharge relations found by Hazel et al. (2006a); (3) Ramp rates are calculated from consecutive minimum and maximum cyclic river stage values.

Discharge data from Lees Ferry were used to calculate stage ramp rates for sandbars located upstream of the Little Colorado River (i.e until site 22 at river mile 56.6). Alternatively, Grand Canyon gauging station data were utilized on sandbars downstream of the Little Colorado River since the Grand Canyon station incorporates discharges from this contributing stream. 1996, 2004 and 2008 high flow experiments were excluded from the analysis since these data represent outliers of the MLFF.

The decrease in stage downramp rates between unrestricted flows and MLFF is substantial, and downramp rates in Marble Canyon are significantly higher than Grand Canyon. Box and whisker diagrams of historical stage downramp rates at the 47 sites are shown in Figure 2.3. Stage downramp rates for years of 1988 to 1991, corresponding to dam operations prior to regulatory restrictions are shown in Figure 2.3(a) and MLFF ramp rates (years 1997 and 2009) are shown in Figure 2.3(b). The largest downramp rates are evidenced at sandbars 22.0R, 23.6L, 29.5L, 30.8R and 35.1L in Marble Canyon. Downramp rates corresponding to 99^{th} percentile at these sites range between 0.43 m/h and 0.51 m/h in the pre-restricted era. These sandbars are located in the Supai Gorge and Redwall Gorge geomorphic reaches, which are characterized by narrow canyon widths and high decrease in topographic elevation (i.e. steep slopes) (Schmidt and Graf 1990). Prior to ramp restrictions, 14 sites experienced downramp rates at the 75^{th} percentile below 0.1 m/h, 26 had 75^{th} percentile rates between 0.1 m/h and 0.2 m/h and 7 sites were between 0.2 m/h and 0.3 m/h at 75^{th} percentile. In contrast, downramp rates during MLFF operation years are significantly smaller at each study sandbar, 39 bars reported downramp rates values at 75^{th} percentile below 0.1 m/h, and only 8 bars had 75^{th} percentile downramp rates varying 0.1 m/h and 0.15 m/h. There are significant outliers

during MLFF operation. These are possibly the result of relatively local hydrological events imposed upon a reduced daily range. These could also have occurred during power plant capacity flows of 31,000 cubic feet per second, which were not excluded from our analysis. A compilation of the entire set of statistics characterizing the probability distribution of downramp rates at all sandbar sites is presented in Appendix A.

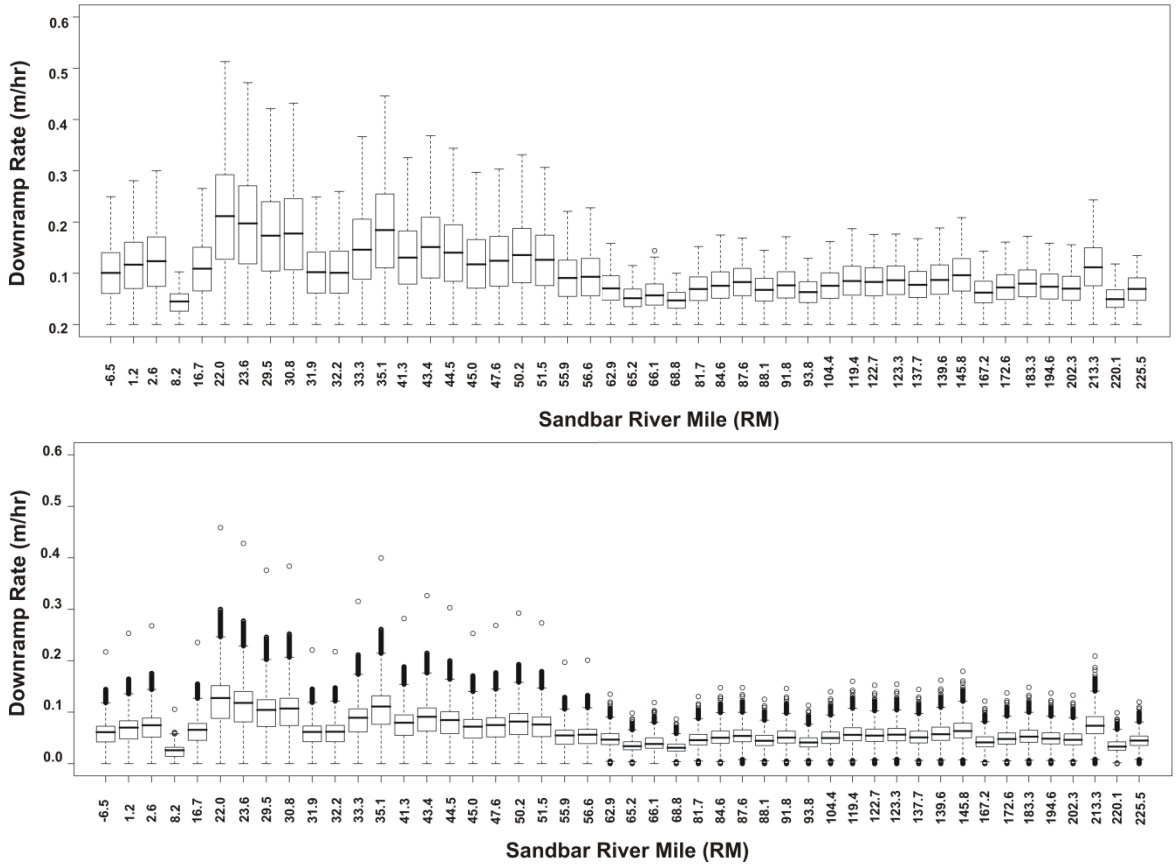

Figure 2.3. (a) Box plot and whisker diagrams of downramp rates records during historical dam operation criteria, year 1988 to 1991. (b) Boxplot and whisker diagrams of downramp rates records during MLFF dam operation criteria, year 1997 to 2009. Data outside of the inner fence and outer fence are represented by dots which are overlapping.

Laboratory experiments incorporate these results of historical downramp rates by including the entire range of historical downramp rates. Thus, ramp rates imposed in the

experiments vary between 0.1 m/h and 0.6 m/h. Ramp rate values from 0.1 m/h to 0.2 m/h primarily simulates current Record of Decision, MLFF operation criteria, while ramp rates over 0.3 m/h simulate maximum possible unrestricted downramp rates.

METHODOLOGY

Description of the Experiment and Instrumentation Details

In the laboratory, a range of river stage and groundwater fluctuations which occur, or could occur, in Marble Canyon and Grand Canyon sandbars are replicated. The main objective is to examine seepage erosion by means of a full scale sandbar physical model. This apparatus consists of a wooden and steel structure of 8 meters long, 2.5 meters high, and 0.5 meters wide and contains approximately four cubic meters of fine-grained sand (see section for soil properties). It is a two dimensional physical model capable of simulating erosion of sandbars under imposed river stage scenarios (see Figure 2.4).

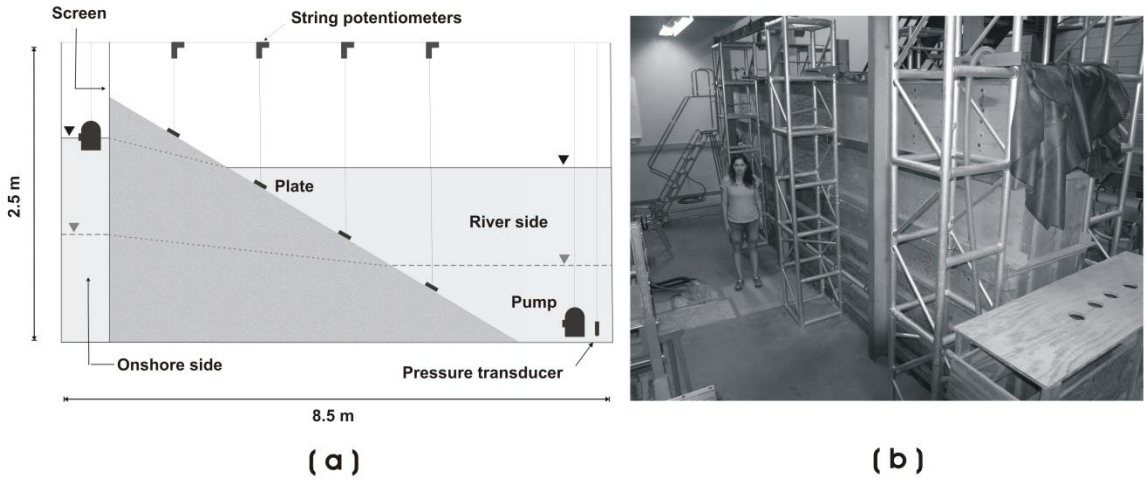

Figure 2.4. (a) Schematic representation of laboratory apparatus. (b) Outside view of sandbar model taken from onshore side of the sandbar.

The face of a sandbar is built up against a metal screen. The water level behind the screen can be adjusted to provide a time-varying groundwater level at the onshore end of the sandbar face.

Sensors and equipment installed at the bar were used to measure: (1) upramp and downramp rates (2) river and groundwater levels and (3) the topographic profile. A submerged pump and pressure transducer were placed at the onshore end of the sandbar face to monitor ramp rates and river levels. A circuit of valves was attached to the pump to control fluctuation rates, permitting continuous rising and falling river stages. The circuit allows water to drain or to recirculate back to the bar. Valves were manually operated and this operation was coordinated using a script in R programming language. The script reads data from the pressure transducer and calculates the ramp rate of the stage in the experiment. This measured rate is adjusted with valves to match the desired ramp rate. A second submerged pump was employed behind the screen in order to set the position of the groundwater level. This pump was manually operated using a winch. Manual operation of the winch led to groundwater fluctuations being approximated as a series of step functions (see Figure 2.5). Many of the experiments involved multiple downramp cycles. As soon as one downramp phase was completed, the apparatus was slowly filled to begin the next downramp phase. In this manner more than one cycle could be completed in a day. Finally, topographic profiles were measured every 0.2 m using a tape measure after each full cycle of river fluctuation.

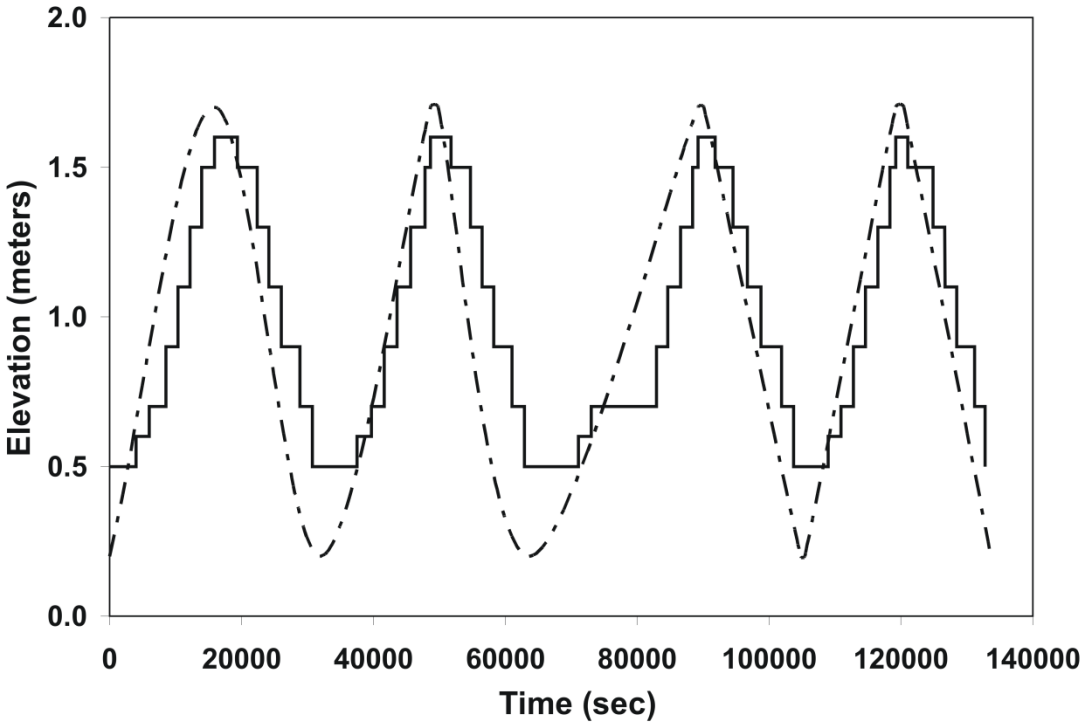

Figure 2.5. River stage and groundwater level corresponding to Experiment 10 at slope of 26 degrees and ramp rates between 0.3 and 0.4 m/h. Note: river stage piezometer is plotted with dashed line and groundwater level with solid line.

Soil Characteristics

Sediment used in the experiments was purchased from a sand and gravel mining operation along the Agua Fria River in Sun City, Arizona. Soil laboratory tests were performed to estimate relevant soil parameters, including: grain size distribution, specific gravity, permeability and direct shear stress. Results from these tests are summarized in Table 2.1. The sediment used in the experiments is classified as fine to very fine sand by the USDA system, based on soil size distribution (Figure 2.6). Trial 1 shows that 94% (>50%) of the soil particles passes sieve # 60 (0.25 mm) and only 6% passes sieve N° 200 (0.074mm). Trial 2 corroborates these results since 65% of the soil particles passed sieve # 60 and only 3 % passes sieve N° 200 (0.074mm).

Table 2.1. Summary of sediment properties.

	Trial 1	**Trial 2**		
D_{50} (mm)	0.18	0.2		
Specific gravity				
Gs	2.77			
Permeability				
Trial N	**1**	**2**	**3**	
Permeability *k* (*10^{-2} cm/s)	0.0083	0.003	0.0032	
Void ratio (*e*)	1.33	1.07	0.88	
Direct shear test unconsolidated undrained oven dried soil sample				
Trial N	**1**	**2**	**3**	**4**
Normal Stress (*Kpa*)	20	40	60	80
Maximum shear stress (*Kpa*)	31	50	72	83
Angle of internal friction (°)	41.7	Cohesion	14.5	

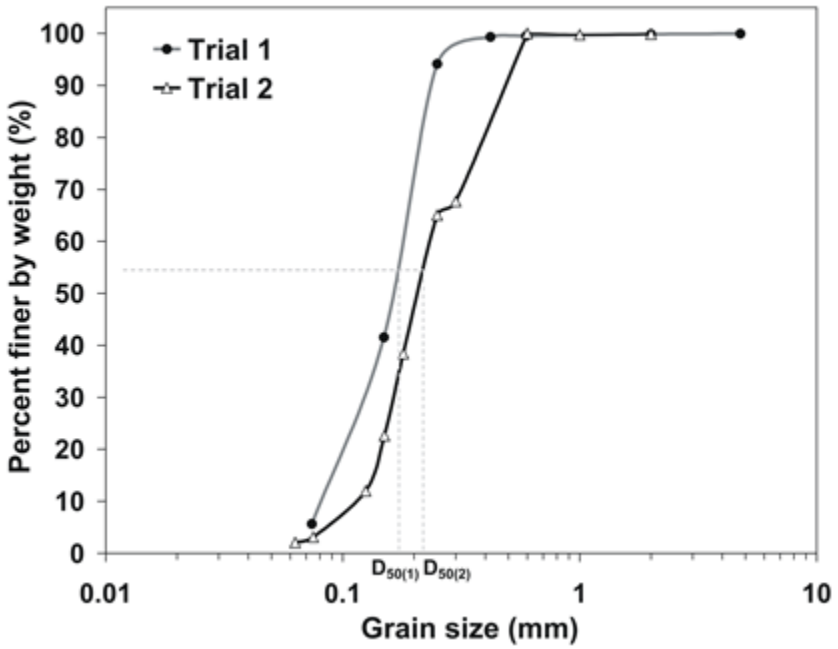

Figure 2.6. Grain-size distribution of two laboratory sediment samples.

In general, the size of the laboratory sediment ranged between 0.1 mm to 0.25 mm with a median grain size (D_{50}) between 0.18 and 0.2 mm. Topping et al. (2005) concluded that during 1983 to 2000 the median size of sediment on the surface of eddy sandbars in Marble and Upper Grand Canyons varied approximately between 0.13 mm and 0.27 mm. Eddy sandbar surfaces coarsened during the flood of 1983 from approximately 0.13 mm to 0.27 mm and have fined between 1986 and 1991 decreasing in median grain size diameter from 0.27 mm to 0.17 mm (Topping et al. 2005). Thus, based on these published field results, the sediment used in the laboratory is representative of sandbars in Marble and Grand Canyons.

Inputs to the Model: Groundwater Table and Initial Slope

A critical issue in the experiments is the imposed groundwater level at the onshore end of the laboratory sandbar face. The U.S. Geological Survey in cooperation with Northern Arizona University conducted a field study of groundwater table changes in the sandbar river mile 30.7 (Tom Sabol, U.S. Geological Survey, Flagstaff, Arizona, unpublished data). Piezometers were installed in a number of temporary wells in the sandbar during MLFF stage fluctuations. River stage was measured simultaneously. The data were collected continuously from January 1st, 2005 to March 8th, 2005. One particular well was selected as the best analog for the groundwater height at the onshore end of the laboratory slot since its location was at the sandbar crest and was within one meter, horizontally, from river shoreline at the peak stage. Also, the hydraulic conductivity of the well (0.08 m/day) closely matches the hydraulic conductivity of the laboratory sediment. These data show that ground-water fluctuations respond with a lag to the hydrograph (see Figure 2.7). This condition produced increases in pore water

pressures by exfiltrating groundwater during rapid drawdown in river stage, which results in seepage erosion, rilling and possible mass failures depending on sandbar topography (Beus et al. 1992; Budhu and Gobin 1994; Budhu and Gobin 1995). This pattern was simulated in the laboratory as a series of step functions (see Figure 2.5).

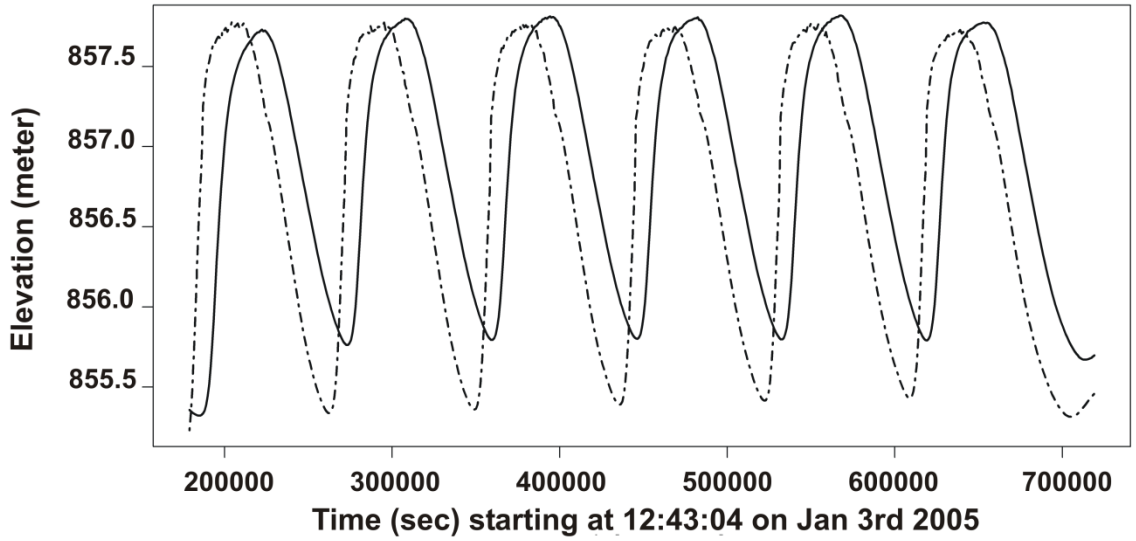

Figure 2.7. River stage and piezometric head corresponding to USGS field data at sandbar 30.7 RM starting on Jan 3rd 2005 to Jan 9th 2005. Note: river stage piezometer (US1) are plotted with dashed line and piezometric head at well 3D with solid line.

A total of 22 experiments were conducted under different slope and dam operation scenarios, 3 experiments were conducted at low (12 degrees) slopes, 6 experiments at intermediate (18 to 22 degrees) slopes and 13 experiments at steep (26 degrees) slopes (see Table 2.2 for details). 8 experiments were not reported in Table 2.2 since they were performed with the objective of testing sensors and equipment. Onshore groundwater levels in Experiments 1 to 11 (see Table 2.2) were controlled to match those found in the field by Sabol (Tom Sabol, U.S. Geological Survey, Flagstaff, Arizona, unpublished data) as described in the previous paragraph. Experiments 12 to 14 primarily tested intermediate and steep slopes and rapid downramp rates. Experiments 13 and 14

maintained onshore groundwater levels far in excess of field results for MLFF diurnal fluctuations. These "synthetic" experiments illustrate erosion rates in which the stage is maintained at a high level for a period of time (between 4 to 6 hours), followed by a precipitous drop in stage.

Table 2.2. Table of laboratory experiments. Experiment numbers 1 through 11 were conducted with an upslope groundwater boundary condition designed to match field results. Experiments 12 through 14 were conducted with differing upslope groundwater boundary conditions.

Experiment N°	Slope (°)	Ramp rate (m/h)
Exp 1	12	0.3-0.4
Exp 2	12	0.5-0.6
Exp 3	18	0.1-0.2
Exp 4	18	0.3-0.4
Exp 5	18	0.5-0.6
Exp 6	22	0.1-0.2
Exp 7	22	0.3-0.4
Exp 8	22	0.5-0.6
Exp 9	26	0.1-0.2
Exp 10	26	0.3-0.4
Exp 11	26	0.5-0.6
Exp 12	18	0.3-0.4
Exp 13	26	0.4
Exp14	26	0.5

The lower limit of slopes in the laboratory experiments follows the work of Budhu and Gobin (1994). They found that slopes of sandbars in Grand Canyon that were in the zone of stage fluctuations for an extensive period of time were in the range between 11 and 14 degrees. The internal friction angle of sand deposits in Grand Canyon is approximately 30 degrees. Budhu and Gobin (1994) found that maximum slopes following deposition were 26 degrees. Slopes at the sandbar were measured at several positions at river mile 30.7 following the high flow experiment of 2004 (Figure 2.2), and

all were found to be 26 degrees. Based on these observations the laboratory experiments were conducted in the range between 12 and 26 degrees.

RESULTS AND DISCUSSION

Influence of Slope and Ramp Rates on Sandbar Degradation

Below the effect of slope and stage ramp rates on sandbar erosion is discussed, based on results presented in Figure 2.8 through Figure 2.12. The discussion is organized by slope categories: low slopes (12 degrees), intermediate slopes (18 degrees and 22 degrees) and steep slopes (26 degrees). A detailed description of the experimental results is summarized in Table 2.3. Furthermore, Figure 2.8 presents a matrix of the experiments showing initial slope versus final slope at each scenario tested. This figure is arranged in a grid of 3 columns by 4 rows where sandbar slopes vary by rows and ramp rates vary by columns.

Table 2.3. Summary of statistics for erosion rate values (cm/cycle).

Exp #	Slope (degrees)	Drawdown (m/h)	Average erosion rate (cm/cycle)	Maximum values (cm/cycle)	Minimum values (cm/cycle)	Standard deviation (σ) (cm/cycle)
Exp 3	18	0.1 - 0.2	0.345	0.367	0.323	0.031
Exp 6	22	0.1 - 0.2	2.302	2.616	1.987	0.445
Exp 9	26	0.1 - 0.2	3.625	4.364	2.887	1.044
Exp 4	18	0.3 - 0.4	0.695	1.312	0.147	0.585
Exp 7	22	0.3 - 0.4	1.341	2.418	0.552	0.791
Exp 10	26	0.3 - 0.4	3.457	7.302	0.811	2.754
Exp 5	18	0.5 - 0.6	1.046	2.402	0.281	0.931
Exp 8	22	0.5 - 0.6	1.806	3.983	0.672	1.496
Exp 11	26	0.5 - 0.6	3.376	4.406	1.939	1.059

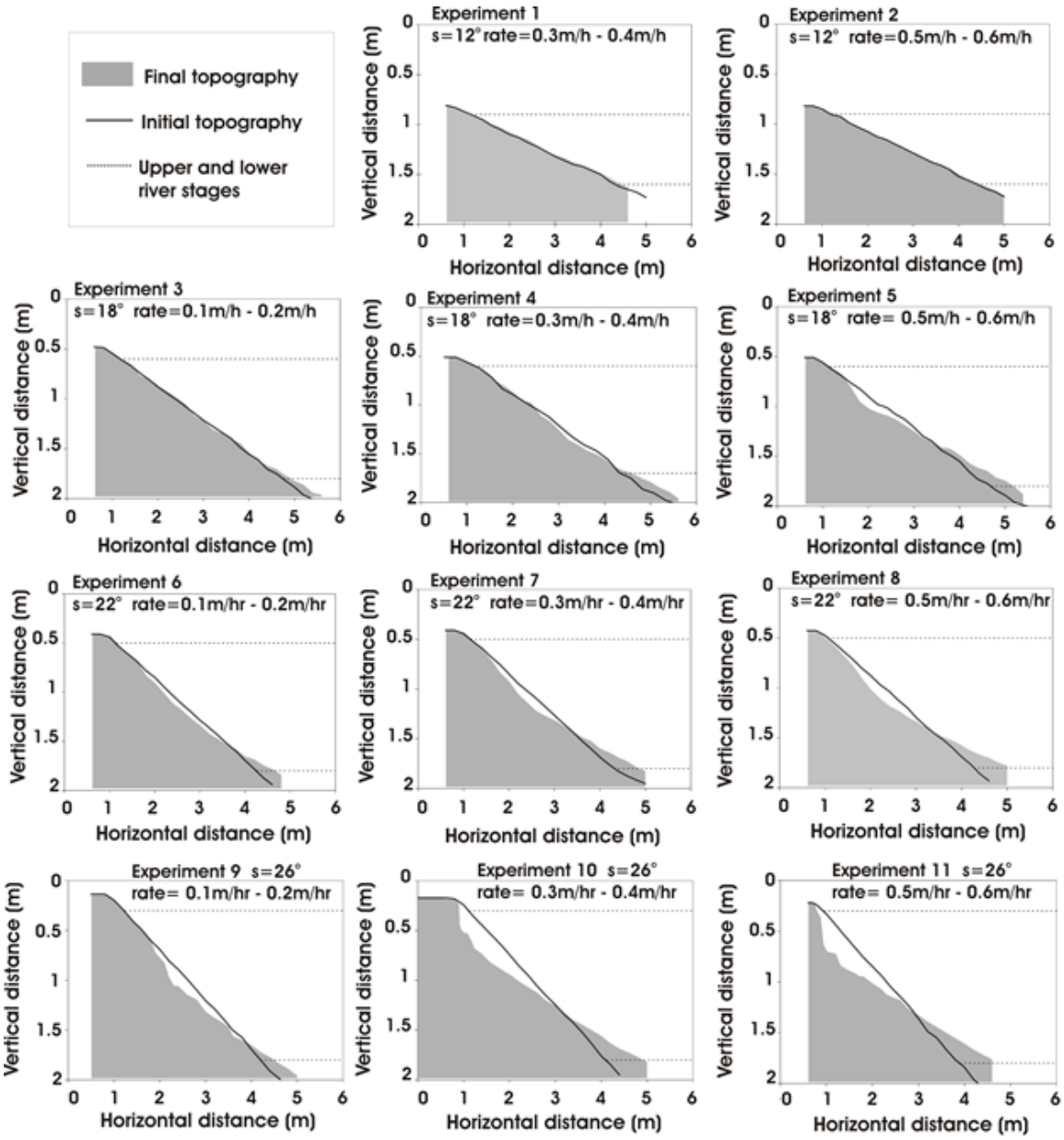

Figure 2.8. Initial and final topography of experiments tested at 12, 18, 22 and 26 degrees slopes and three ramp rates scenarios: 0.1m/h – 0.2m/h, 0.3m/h – 0.4m/h and 0.5m/h – 0.6m/h. The zero reference of vertical distance is located at the top of the bar.

Low Slopes

Low slopes (12 degrees) resulted in undetectable mass loss under all imposed ramp rates, as shown in Experiment 1 and Experiment 2 (Figure 2.8. and Table 2.2.).

Initial topography matched final topography in experiments conducted at rates of 0.3 m/h to 0.4 m/h and 0.5 m/h to 0.6 m/h, demonstrating the stability of 12 degree slopes at all tested ramp rates. This result is consistent with the studies of Budhu and Gobin (1994) and (1995). Although, mass loss was not large enough to be measured, a small amount of mass loss must have occurred because rills and rivulets were manifest on the bar surface at the completion of each downramp phase (see Figure 2.9(a)).

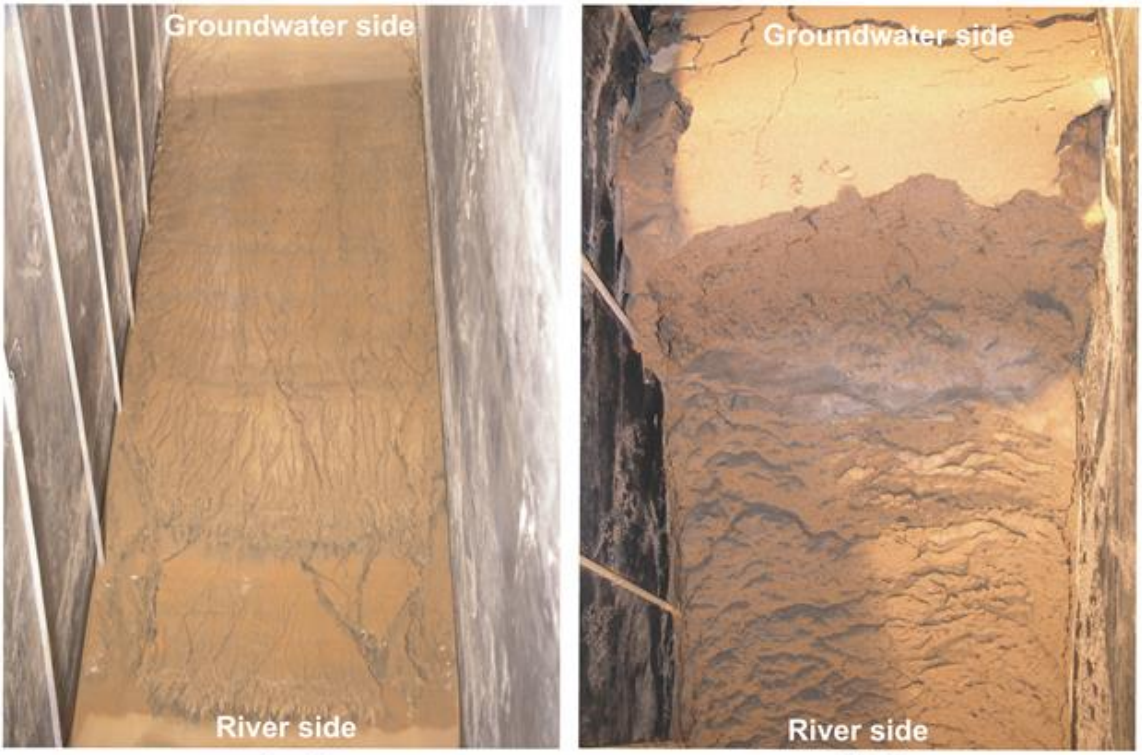

Figure 2.9. Contrast between seepage erosion and mass failures. (a) View of the bar surface at low slope (12 degrees) and maximum ramp rate tested (0.5m/h – 0.6 m/h), Experiment 2. Notice the formation of small rills. (b) View of mass failure at steep slope (26 degrees) and ramp rate equal to 0.3m/h – 0.4 m/h, Experiment 10.

These experimental ramp rates are as high or higher than any beaches have experienced in Grand Canyon due to dam operations, and they are far higher than any beaches experience under the current operating parameters of Glen Canyon Dam.

Sandbars with 12 degrees or lower slopes appear to be stable to mass failure and seepage erosion under any possible dam operation scenario.

Intermediate Slopes

Mass failures were not evidenced at any conducted experiment at intermediate slopes (18 degrees and 22 degrees). Experiments conducted at 18 degrees achieved slope stability at ramp rates 0.1 m/h – 0.2 m/h and below, resulting in minimum seepage erosion at the bar surface (Experiment 3) (Figure 2.8). Minimum mass loss was evidenced at ramp rates equal to 0.3 m/h and 0.4 m/h (only 743 cm^3/cm volume of erosion) (Experiment 4) (Figure 2.8) while significant mass loss ensued at ramp rates tested at 0.5 m/h – 0.6 m/h (Experiment 5) (Figure 2.8). The total volume of erosion in Experiment 5 (Figure 2.8) was 1490 cm^3/cm (Figure 2.10(a)) and it was driven by seepage erosion by exfiltrating groundwater.

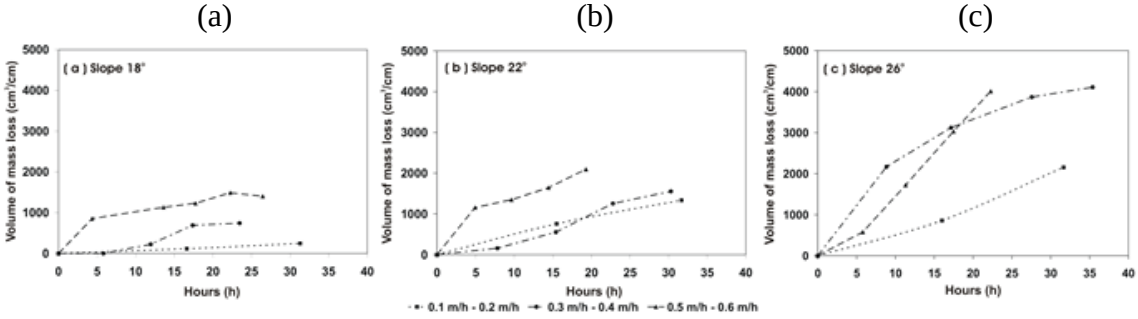

Figure 2.10. Volume of mass loss over time categorized by sandbar steepness. (a) Volume of mass loss at 18 degrees slope. (b) Volume of mass loss at 22 degrees slope. (c) Volume of mass loss at 26 degrees slope.

Mass loss was found at 22 degrees slope for all imposed downramp rates. Total volume of mass loss were reported as 1335 cm^3/cm, 1555 cm^3/cm and 2095 cm^3/cm for experiments 6, 7 and 8 (see Figure 2.8 and Figure 2.10(b)) respectively showing how erosion increases by a factor of 1.5 from minimum to maximum ramp rate scenarios.

In general, the dominant erosion process at intermediate slopes (18 and 22 degrees) was seepage erosion and sediment transport in rills at the bar face. Seepage occurred mostly during down ramp by exfiltrating groundwater. Mass loss per hour and total volume of mass loss showed some dependence to increases in imposed ramp rates at intermediate slopes (Figure 2.11).

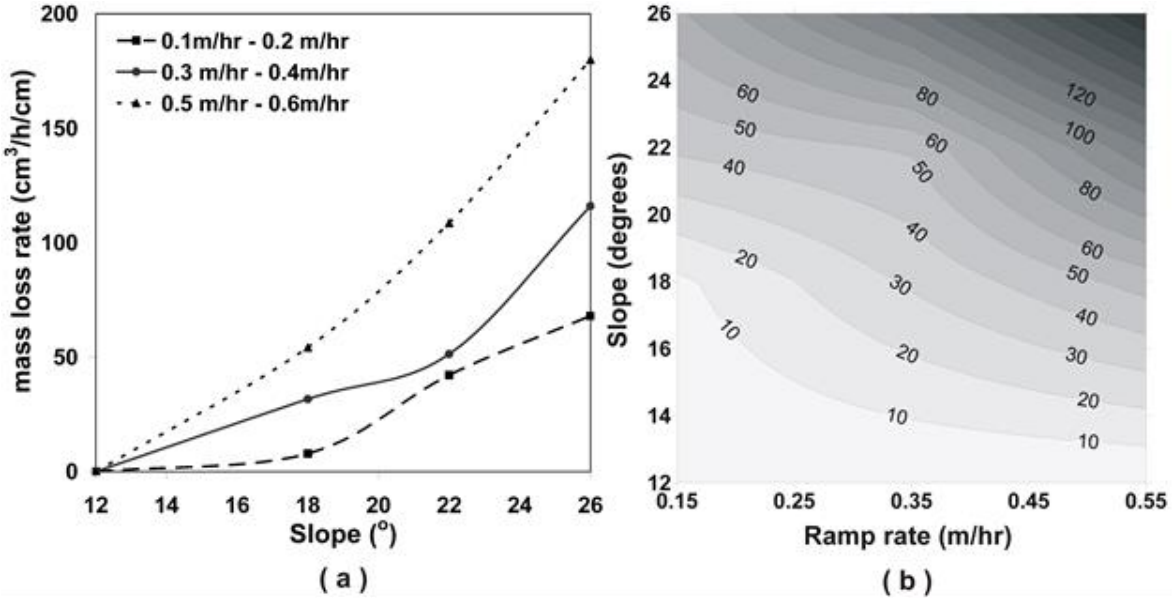

Figure 2.11. (a) Mass loss rate per hour. Ramp rate of 0.1m/h - 0.2 m/h are plotted with dashed line, 0.3 m/h - 0.4 m/h with solid line and 0.5 m/h - 0.6 m/h with dotted line. (b) Contour lines shown mass loss rate per hour at every slope and ramp rate tested. Linear method was the used to interpolate contour lines. Note: The mass loss rate in this figure is computed per downramp time and not per diurnal cycle as shown in Figure 2.12.

However, it is important to note that our experiments did not necessarily follow a daily cycle; as soon as one full cycle was complete, the next cycle began (see Figure 2.5, for example). Therefore, experiments with higher ramp rates had a greater number of cycles per unit time. To account for this data of Figure 2.11 were re-plotted the as erosion rate per cycle in Figure 2.12.

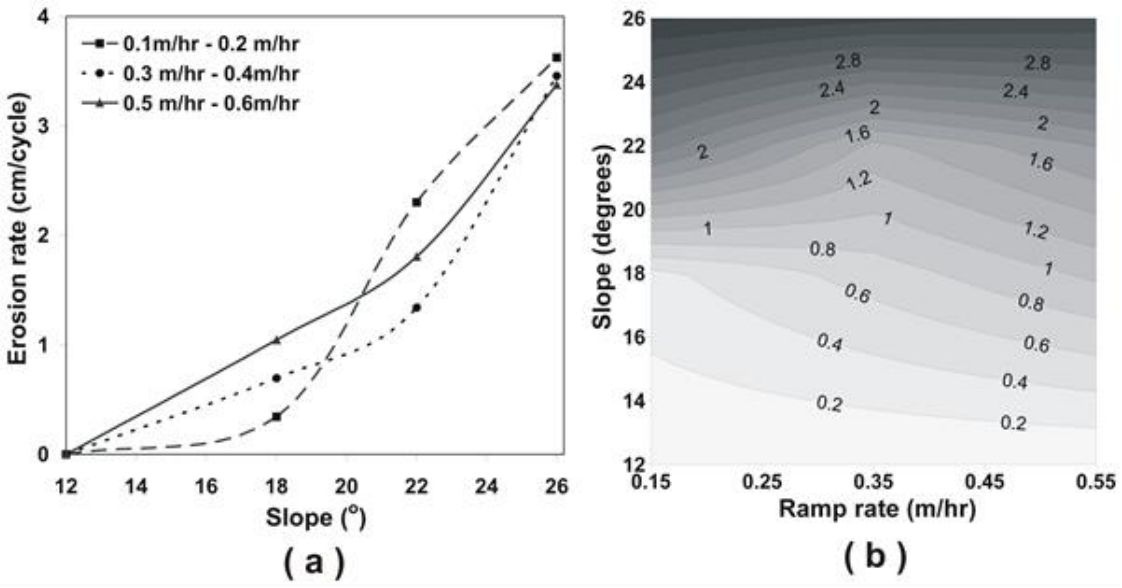

Figure 2.12. (a) Average erosion rate per cycle. Ramp rate of 0.1m/h - 0.2 m/h are plotted with dashed line, 0.3 m/h - 0.4 m/h with dotted line and 0.5 m/h - 0.6 m/h with solid line. (b) Contour lines shown erosion rate per fluctuation at every slope and ramp rate tested. Note: summary of erosion rate statistics is detailed in Table 2.3.

Figure 2.11 is useful to determine the erosion rate during a downramp phase. Figure 2.12 shows the erosion rate per diurnal cycle, and should be more useful than Figure 2.11 when considering the erosion rate under differing dam operation scenarios. The erosion rate per cycle at a given slope did not show a correlation with ramp rates. Erosion rate per diurnal cycle is not dependent on stage ramp rates in these experiments. Each experiment consisted of multiple cycles, and the erosion rate of each cycle was measured. The standard deviation of erosion rate is reported in Table 2.3 which shows the maximum and minimum erosion rate per cycle. Although no dependence of erosion rate per cycle on ramp rates at a given slope was found, there is a significant dependence of erosion rate on slope (Figure 2.12).

Steep Slopes

Experiments conducted at steep slopes (26 degrees) produced mass failures at all tested river stage fluctuations. These mass failures were inferred by large slumps at the top of the bar (see Figure 2.9(b)). The mass loss evidenced by steep slopes greatly exceeded the erosion at intermediate slopes. The total volume of mass loss per unit width was 2154 cm^2, 4107 cm^2, and 4011 cm^2 for Experiments 9, 10 and 11. The mass loss increased by a factor of 1.9 from minimum to maximum ramp rates scenarios (see Figure 2.8 and Figure 2.10(c)). Overall, steep slopes showed the same pattern observed at intermediate slopes, mass loss rate per hour presented high sensitivity to ramp rates increases (see Figure 2.11), but erosion rate per daily cycle remains almost constant at every tested ramp rates (see Figure 2.12 and Table 2.3). Mass failure is the primary process of degradation of steep beaches in these experiments.

The Nature of Seepage Erosion and Mass Failures Mechanisms

Topographic measurements were taken at the end of each fluctuation cycle (one cycle includes both rising and falling phase) in order to evaluate how seepage erosion evolved over time. Results based on volume of mass loss versus time (h) are shown in Figure 2.10.

For intermediate slopes, the bar evolves until reaching steady state. A pattern is observed of decreasing mass loss asymptotically, reaching an equilibrium slope at 14 degrees (Figure 2.10(a) and Figure 2.10(b)). Seepage erosion is the dominant process of mass loss at intermediate slopes (as discussed in previous sections). Therefore, these results showed that seepage erosion driven by exfiltrating groundwater and manifest as rilling is characterized by continuous but low erosion rates. For higher slopes, erosion

rates are significantly high compared with erosion rates presented at intermediate slopes (Figure 2.12). Experiments conducted at 26 degrees did not reach steady state except for Experiment 10 (Figure 2.8) performed at ramp rate 0.3 m/h – 0.4 m/h where the equilibrium slope reaches 13 degrees (Figure 2.10(c)).

The Effect of Exfiltrating Water

The previous sections studied seepage erosion and mass failures due to the influence of two main variables: slope and ramp rates using identical groundwater level conditions (details summarized in previous sections). In this section, the influence of exfiltrating groundwater on sandbar degradation is discussed. During the falling phase of river stage, the groundwater table becomes higher than the river stage exposing the bar to seepage erosion. The difference in level between groundwater and river stage will depend on how rapid the falling phase occurs as well as sandbar soil properties, primarily: hydraulic conductivity, specific storage, permeability, bulk density among others.

Experiment 12 was conducted at intermediate slopes (18 degrees) and it was compared with Experiment 4 (also at 18 degrees) (see Figure 2.13). Higher lag response from the groundwater was imposed on Experiment 12, thus, during the falling phase groundwater was maintained 0.5m on average higher than stage, while at Experiment 4, groundwater was positioned above river level by 0.2 m to 0.3 m. Results showed significant increases in mass erosion at higher groundwater levels. Experiment 4 (Figure 2.13) represents only 43% of the mass loss compared to Experiment 12 (Figure 2.13). Eroded mass presented at Experiment 12 (Figure 2.13) was 1720 cm3/cm while the mass loss of Experiment 4 was 743 cm3/cm. Higher groundwater levels lead to greater mass loss at intermediate slopes.

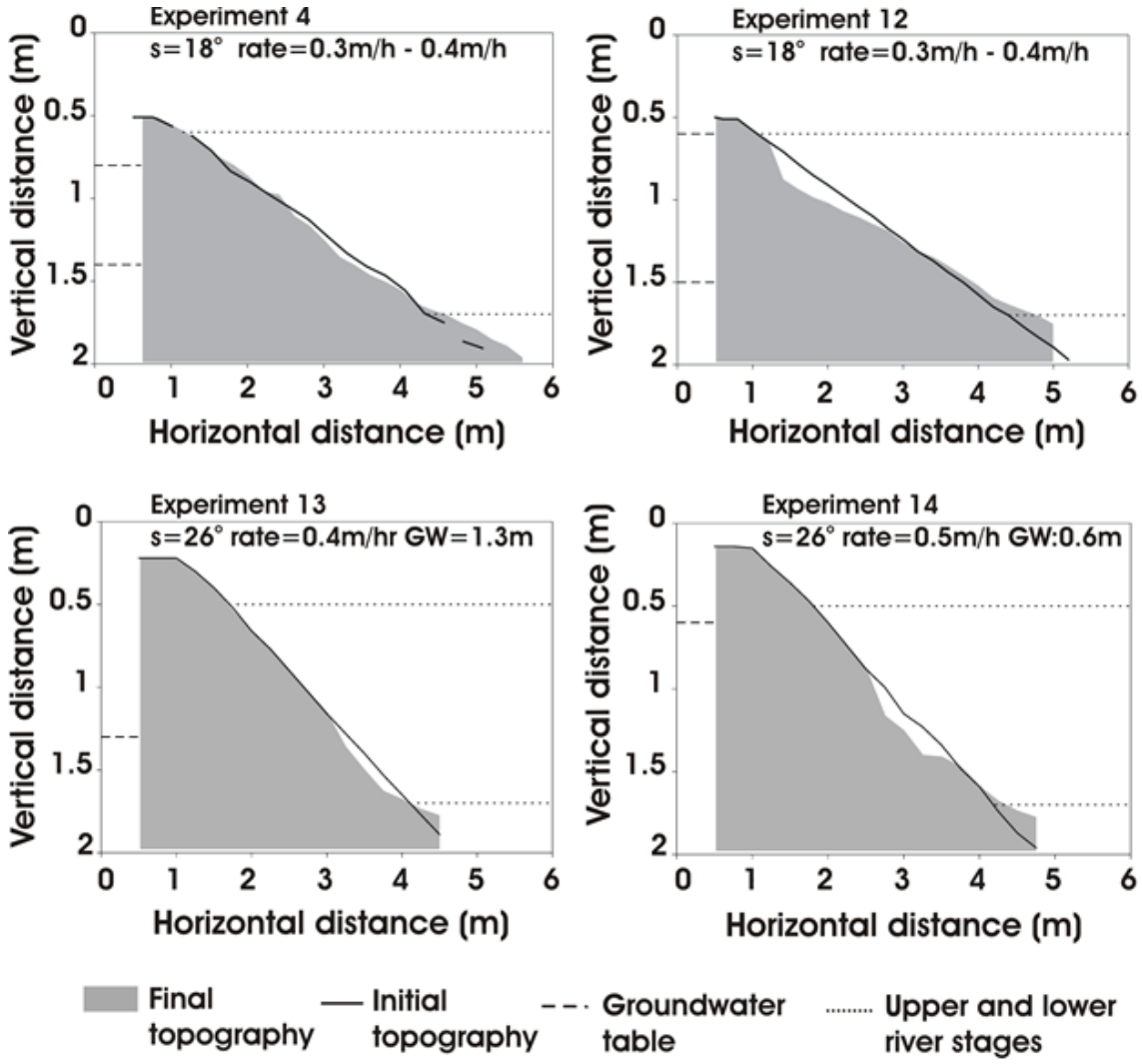

Figure 2.13. Initial and final topography of experiments 4, 12, 13 and 14. Groundwater table is variable at both Experiment 4 and Experiment 12. Upper and lower groundwater table are shown for these cases. Groundwater table was held constant in both Experiment 13 and Experiment 14.

At steep slopes, two further experiments (Experiments 13 and 14, Table 2.2) with synthetic river stage and upslope groundwater boundary conditions were performed keeping the groundwater table constant while dropping the river stage at the same intervals. These short experiments considered only one downramp cycle. Experiment 13 was performed at 0.4 m/h, while the onshore groundwater table level was held constant at

1.3 m with the river level at an initial stage of 0.5 m. Experiment 14 was performed at 0.5 m/h, constant groundwater level of 0.6 m, and river level initial stage 0.5 m. These experimental conditions are not currently experienced at Grand Canyon beaches, but they could occur in other river systems, for instance, for a watershed where the aquifer discharges to the river versus a watershed where the river infiltrates to the aquifer. The results show that seepage erosion was only present below the groundwater table where the groundwater becomes higher than river stage in Experiment 13. This confirms that seepage erosion occurs during the falling phase due to water exfiltration. Furthermore, mass failures did not occur in Experiment 13 (low groundwater conditions) while mass failures were evidenced in Experiment 14 (high groundwater levels) (see Figure 2.13). Low groundwater levels significantly diminished erosion. The volume of mass loss measured in the low groundwater table experiment was 54% of the mass volume eroded in the high groundwater experiment. The volume of mass loss resulted in 738 cm^3/cm and 1375 cm^3/cm for Experiment 13 and Experiment 14, respectively. In summary, the height of the groundwater at the onshore end of the bar face is important. If these groundwater levels are higher than currently occurs in Grand Canyon sandbars, the erosion rates would be higher.

CONCLUSIONS

Sandbars in Marble and Grand Canyons experienced significantly larger downramp rates prior to interim discharge restrictions (Appendix A and Figure 2.3). The largest stage fluctuations are found between river mile 22 and 35 where the canyon is narrow. Stage variations within the canyons differ depending on the geomorphic location (Kearsley et al. 1994). The sandbar at river mile 22.5 experienced the largest downramp

rates. Prior to interim restrictions this sandbar experienced downramp rates of 0.51 m/h at the 99th percentile, and under current MLFF operation criteria this sandbar experiences 99th percentile downramp rates of 0.24m/h.

It is concluded from the results obtained in these laboratory experiments that the effect of restricting maximum ramp rates is less significant for bar stability purposes than the effect of sandbar steepness (slope). Bar stability is achieved at the equilibrium slope (14 degrees for this study which is consistent with studies from Budhu and Gobin (1994) and (1995). Thus, the bar surface becomes insensitive to mass loss at each tested ramp rate once it reaches an equilibrium slope. In absence of other processes, almost any ramp rates would rapidly reduce newly deposited steep beach faces, in the range of stage variations, to equilibrium slopes, at which time erosion by mass failure and seepage processes would largely cease. Other processes, especially removal of sediment at the toe of these slopes by turbulent flow and waves could locally increase the slope, and, therefore, rejuvenate mass loss by mass failure and seepage erosion.

Seepage erosion by rilling was found at all slopes greater than the equilibrium slope. The rate of mass loss per diurnal cycle, at a given slope and at groundwater levels documented in Marble and Grand Canyon beaches, does not appear to be sensitive to ramp rates (Figure 2.12). Further, the relation between discharge ramp rates at the dam and stage ramp rates at sandbar sites is not linear. A large increase in dam discharge downramp rates results in only moderate increases in stage ramp rates at individual sites (Appendix B). Thus, greatly increased diurnal dam discharge ramp rates, above the current MLFF operation criteria, should have little effect on the mass loss of sandbars. It is important to note that this applies only to a change in ramp rates. If the total volume of

water released in a day was held constant and ramp rates were increased, the peak discharge and/or the duration of peak discharge would likely increase. Increasing the peak discharge or the duration of peak discharge would increase sediment transport capacity, potentially resulting in enhanced sandbar toe erosion.

It is important to remark that these conclusions are based on laboratory simulations which simplify the complexities of real Colorado River sandbars. The laboratory setup was for a two-dimensional bar face. There can be significant cross-bar topographic variations that can locally increase groundwater exfiltration. Also, the laboratory sediment was a homogenous mixture, whereas real sandbars have a complex, layered grain size structure. Thus, the permeability and internal friction of real sandbars are spatially variable.

Future work on erosion of Grand Canyon sandbars should be oriented to quantify the erosion of sandbars by turbulent flow and waves. This and previous work shows that erosion of sandbars in the zone of stage fluctuations that are greater than about 14 degrees is inevitable, and that after bars have reached this equilibrium slope, erosion by mass failure and seepage erosion is largely extinguished. Continued erosion of sandbars, thus, depends primarily on erosion of sandbars by the flow and waves below the water surface. The transport of sediment by turbulent flow depends upon such factors as the boundary shear stress and the median grain size; the rate of change of river discharge is not a primary factor. Therefore, dam discharge ramp rate, in itself, is probably not a key factor in sandbar erosion. However, factors, such as the time at peak discharge, the maximum discharge, and the discharge range, could be critical factors in determining the long-term erosion of sandbars.

CHAPTER 3

TURBULENCE RESOLVING MODELING OF LATERAL SEPARATION ZONES ALONG A LARGE CANYON-BOUND RIVER USING DETACHED EDDY SIMULATION TECHNIQUE

INTRODUCTION AND BACKGROUND

Prediction of geomorphic change in river channels is a goal of many investigations in both regulated and unregulated river systems. One approach often used to quantify and predict river systems is the numerical modeling. The majority of fluvial numerical models currently used are two- and three-dimensional quasi-steady or steady models. Some studies emphasize that fluvial numerical modeling requires an explicit representation of turbulence flow structures because a direct solution of flow allows a better fidelity in the computation of turbulence structures and suspended sediment (Bradbrook et al. 2000a; Zedler and Street 2001; Cao and Carling 2002; Nelson et al. 2003; Tseng and Ferziger 2004; Keylock et al. 2005; Passalacqua et al. 2006; Keylock et al. 2011; Grigoriadis et al. 2012; Keylock et al. 2012).

Depth-averaged, two dimensional models typically rely on simple closures relating boundary stress to roughness and depth-averaged velocity. Three-dimensional models are generally Reynolds-Averaged Navier-Stokes (RANS) models. Most two- and three-dimensional river models are steady or quasi-steady approximations, wherein bed stresses do not vary at the time-scale resolving large turbulent structures. In relatively simple channels these models have predictive capabilities, but they can have low predictability in presence of large scale flow separation and secondary flows (Keylock et al. 2012; Chang et al. 2013).

Turbulence-resolving flow and suspended sediment models may do better at predicting turbulence and channel change in complex channels, but at a substantially larger computational cost. With computational parallelization, turbulence-resolving models can now be developed and applied to complex river systems. Turbulence-resolving models based on Large Eddy Simulation (LES) techniques can resolve time-dependent eddy structures, including the nonperiodic pulses of eddy vortices (Akahori 2007). LES technique integrates the spatially-filtered Navier-Stokes equations, and eddies larger than the grid scale are resolved, while smaller, sub-grid scale (SGS) turbulence transport is modeled (e.g. Ferziger 1976). Among the most traditional SGS models are the Smagorinsky-Lilly and Germano dynamic models (Ferziger and Peric 2002; Shur et al. 2011a). LES techniques are well established methods of turbulence research and practice, with significant advances over the last two decades (e.g. Squires 2004; Tseng and Ferziger 2004; Spalart et al. 2006; Spalart 2009; Shur et al. 2011a). These techniques have been broadly used in aerospace engineering (Viswanathan et al. 2007; Keylock et al. 2011; Shur et al. 2011b), geophysics and atmospheric sciences (Mason 1989; Galperin and Orszag 1993; Kosovic and Curry 2000). Nonetheless, turbulence resolving models based on LES techniques are mostly an unfamiliar subject in the fluvial geomorphology field (Keylock et al. 2005). While a few studies have applied LES models to fluvial systems, most of the work has been developed at the scale of a laboratory set up (Bradbrook et al. 2000a; Zedler and Street 2001; Tseng and Ferziger 2004; Constantinescu et al. 2011a; Keylock et al. 2011; Keylock et al. 2012; Papanicolaou et al. 2012) and few LES models have been developed at the scale of a river reach. Some of these field-scale LES models have been applied to the study of meandering rivers (Kang

and Sotiropoulos 2011), stream confluences (Constantinescu et al. 2011b) and flow around a circular pier (Kirkil et al. 2009).

In this study, a turbulence resolving model using LES technique is applied to study lateral recirculation zones, which are characterized by flow separation and sediment storage. Lateral recirculation zones have been observed in a variety of river channel configurations. For instance, sharp meanders, river confluences, some engineering structures, and canyon rivers all cause flow separation, secondary recirculation and free shear layers. In sharp meanders, flow separation occurs at the inner bank boundary after the bend apex forming a lateral separation zone (Ferguson et al. 2003; Van Balen et al. 2010; Keylock et al. 2012). In river confluences, a lateral separation zone is observed at the inner bank of the tributary downstream of the confluence. Large scale turbulence structures and highly three-dimensional vortices represented by secondary recirculating eddies are formed downstream of the two confluent channels (Best 1988; Rhoads and Kenworthy 1995; Bradbrook et al. 2000b; Keylock et al. 2012). River engineering structures: such as groyne fields and bridge piers can also lead to flow separation and lateral recirculation downstream from these structures (Sukhodolov et al. 2002; Uijttewaal 2005; Chang et al. 2013). In rivers flowing within debris-fan dominated canyons, a lateral recirculation zone is the product of channel constriction exerted by the tributary debris fan and downstream channel expansion (Leopold 1969; Howard and Dolan 1981; Schmidt 1990).

The linkages between the hydraulic patterns and topographic features have been extensively documented for canyon rivers. This linkages and patterns have been studied using the concept of fan eddy complex for the case of the Colorado River in Grand

Canyon (Figure 3.1), as well as for other confined-bedrock rivers (Garrett et al. 1993; Schmidt and Rubin 1995; Schmidt et al. 1995; Grams and Schmidt 1999; Grams et al. 2007; Wright and Kaplinski 2011).

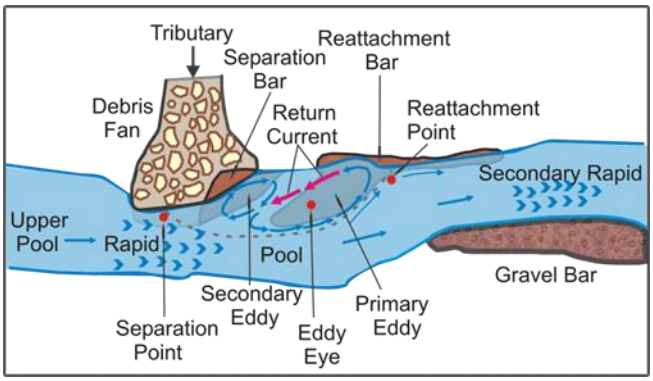

Figure 3.1. Conceptual diagram of a fan eddy complex showing the major lateral recirculation currents and the main geomorphic features. Adapted from Webb et al (1999).

The fan-eddy complex is a geomorphic assemblage composed of gravel bars, a debris fan, a lateral separation zone, and reattachment and separation bars (Figure 3.1). Debris fans are supplied by steep tributaries and are mainly composed of coarse-grained material. Rapids are formed at channel constrictions caused by tributary debris fans. The lateral separation zones are typically formed downstream of rapids and are the principal zone of fine sediment storage in canyon rivers. These zones feature large scale flow separation, secondary flow structures, return currents and free shear layers. Most sand bars are formed in the vicinity of separation and reattachment zones and gravel bars are located upstream of the debris fans or downstream of the recirculation at the channel bank opposite the debris fans (Figure 3.1).

Several quasi-steady two- and three-dimensional river models have been tested in areas of channel complex morphology. For the case of the Colorado River, Wiele et al.

(1996) developed a quasi-steady two-dimensional flow modeling to represent four eddy fan complexes located downstream from the Little Colorado River (Wiele et al. 1996). Miller (1994) developed a conceptual two-dimensional flow model to study the flow patterns in canyon rivers to be applied in the South Branch Potomac River and the Colorado River (Miller 1994). These models have not been validated against observations because flow field data were unavailable at that time. More recently, quasi-steady two- and three- dimensional models (DELFT2D and DELFT 3D) to simulate flow, sediment and channel change have been also tested in the Colorado River and assessed using multibeam surveys (Sloff et al. 2009; Sloff et al. 2012). These models have shown predictability of erosion at the river axis (thalweg) but have been inaccurate at lateral recirculation zones resulting in over-supply of sediment within the primary eddy cell (Sloff et al. 2012). Models applied to Grand Canyon separation zones generally predict greater deposition and less erosion than is observed.

The processes responsible for exporting sediment from lateral separation zones are key to reach accurate predictions of sediment patterns in lateral recirculation zones and complex river channel morphologies. Flow field velocities and laboratory experiments have revealed a pattern of nonperiodic eddy pulsation, mainly at the reattachment zone (Rubin and McDonald 1995). This nonperiodicity is characterized by low frequency temporal flow variability and can occur due to intrinsic behaviors, such as pulses in vortices, or due to external forcing, *i.e.* unsteady flows. The recirculation flow in lateral separation zones is typically weaker than main channel flow providing, an environment of deposition and sediment storage. Nevertheless, the model results of Akahori (2007) suggest that nonperiodic eddy pulsations effect the strength of the lateral

recirculation, resulting in episodic export of sediment from the eddy zone and erosion of the eddy bar surfaces.

A three-dimensional model based on Detached Eddy Simulation technique (DES-3D) is used to simulate the flow patterns in two lateral recirculation zones situated in two consecutive fan-eddy complexes along the Colorado River in Grand Canyon. DES is a hybrid RANS and LES technique. In DES, a Reynolds Averaged Navier Stokes (RANS) closure is applied to near-bed and bank grid cells, where grid resolution is not sufficient to resolve near-wall turbulence. LES treatment is given to the flow separation and recirculation regions formed further from the bed and banks. The model study site begins 97 km downstream of Glen Canyon dam (see Figure 3.2).

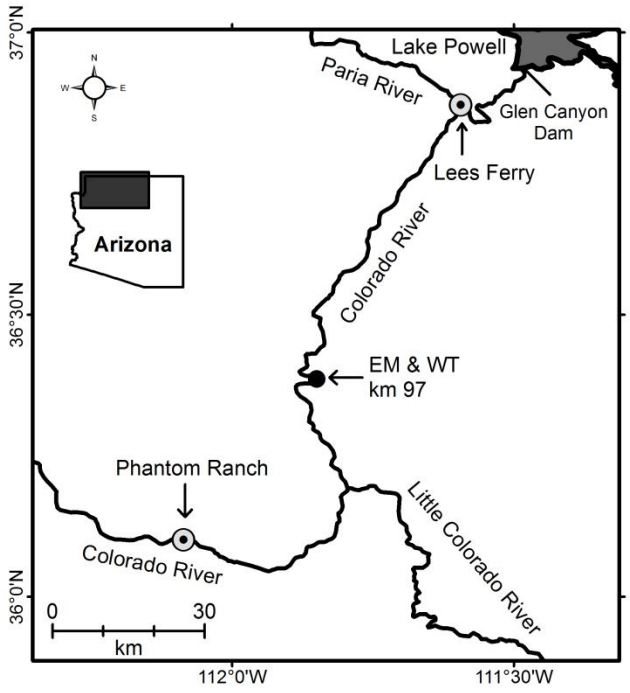

Figure 3.2. Map of the Colorado River downstream of Glen Canyon Dam to Phantom Ranch, showing the location EM and WT eddy-fan complexes

The downstream length of the model reach is 1.4 km. The upstream fan-eddy complex is generally cited in the literature as “Eminence Break” (EM) followed by the downstream fan-eddy complex “Willie Taylor” (WT) (Figure 3.3). Hereafter, these study sites will be referred by using the abbreviation EM for Eminence Break and WT for Willie Taylor. These two lateral recirculation zones have exhibited convoluted three-dimensional flow structures, large-scale flow separation, strong secondary flows and complex sediment transfer dynamics from the main channel into the lateral separation zone.

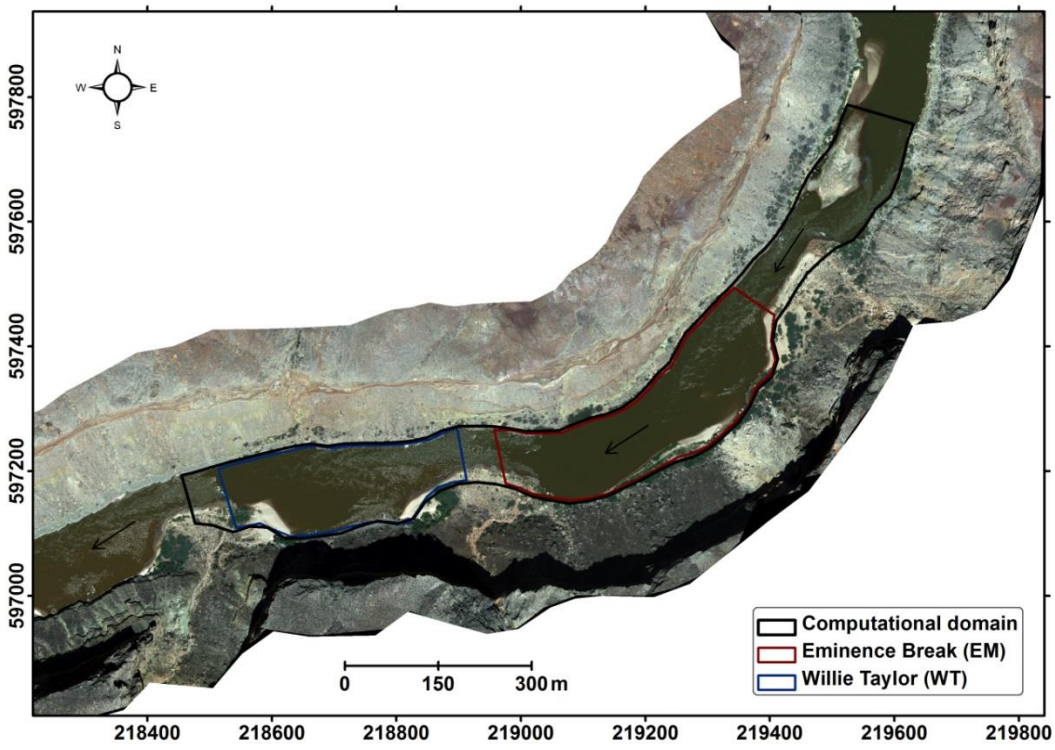

Figure 3.3. Air photo of the study river reach taken in May 25th of 2009. The domain of the computational grid is shown in black, EM and WT fan eddy complexes are delimited in red and blue, respectively.

Detailed field monitoring data were collected at EM and WT fan-eddy complexes during the controlled flood released from Glen Canyon in March 2008 (Wright and Kaplinski 2011). Observed data base includes measurements of velocity from a calibrated ADCP (Acoustic Doppler Current Profiler) at 4920 sites located within our modeling domain. Measurements followed ten river transect lines at each fan eddy complex. The transects were collected from a moving USGS boat and averaged over 10 m bins while the speed of the boat was less than 1 meter per second. The first transect is positioned at 1.27 m below the water surface and the next transects are separated by 0.33 m starting at 1.6 m below the water surface up to the river bed (see Figure 3.4 for details of cross sectional arrangements).

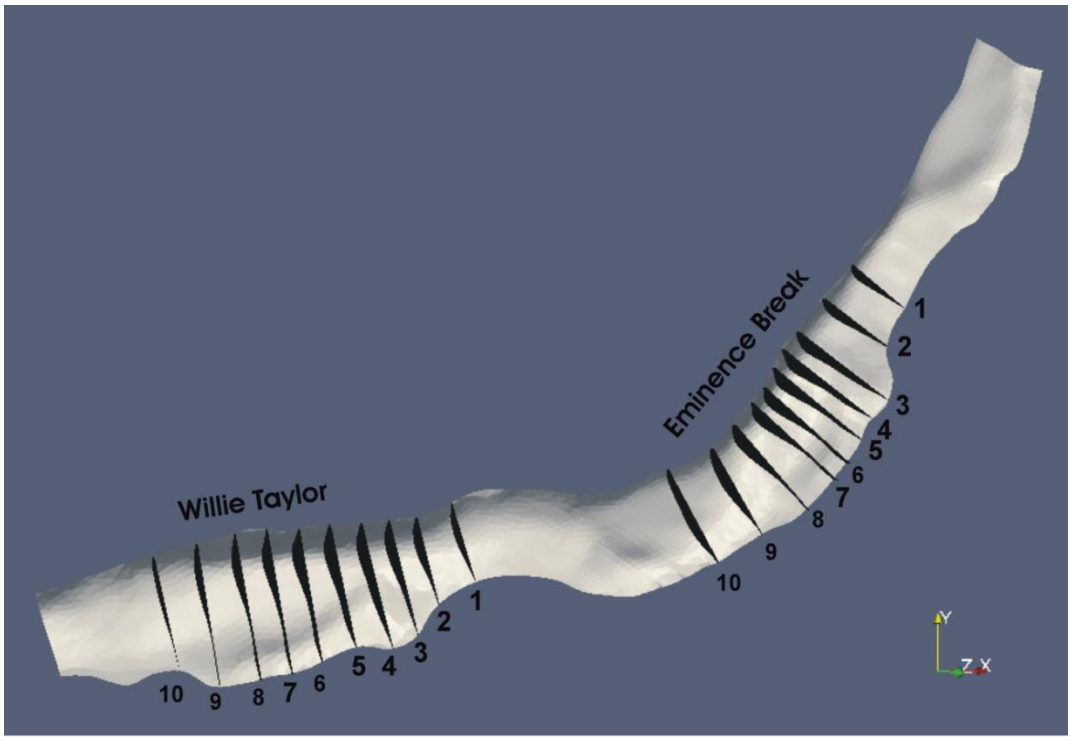

Figure 3.4. Computational domain showing the location of the cross sections corresponding to the transect lines of the ADCP surveys taken at time equals to 1000 second.

Observed data are used for four purposes: (1) building the computational domain, (2) initial and boundary conditions, (3) model result validation, and (4) reference for three dimensional flow structures.

The study area has been also selected for its ecological and economical values. The lower Colorado River basin is located downstream of Glen Canyon Dam within Marble and Grand Canyons (See Figure 3.2). The lower part of the basin provides water to the states of California, Arizona and Nevada and produces hydroelectric power. Nonetheless, benefits of water use and hydroelectric power have come with significant environment cost (Schmidt et al. 1998). Glen Canyon Dam has resulted in drastic changes in flow regimes, reduction of sediment supply and erosion of sediment deposits within lateral separation zones (Kearsley et al. 1994; Schmidt and Rubin 1995; Schmidt et al. 1999; Topping et al. 2005; Hazel et al. 2006). Lateral separation eddy bars have been identified as important environmental and recreational resources. Eddy bars are critical habitat for endangered fish species (Turner and Karpiscak 1980; Converse et al. 1998; Korman et al. 2004); they are an aeolian source of fine sediment that may preserve archaeological sites (Draut and Rubin 2008); serve as a substrate of riparian vegetation (Turner and Karpiscak 1980), and provide campsites for river rafters and tourists (Kearsley et al. 1994). Sediment transport and erosion by turbulent flow is more of a concern for sand resources in Grand Canyon than discharge fluctuations for hydroelectric power generation (Alvarez and Schmeeckle 2013). Therefore, an accurate representation and prediction of the flow and sediment patterns may help in managing the environmental resources and ecosystem services of this river.

MODEL OVERVIEW

The DES-3D model is a parallelized, unsteady and three dimensional. The computational domain comprises 5,625,000 cells. The grid distribution consists of 1500 cells in the streamwise direction, 150 cells cross-stream direction, and 25 cells in the vertical direction. This grid is approximately 1 meter by 1 meter in the horizontal dimension. The model statistics show convergence after 15 minutes of simulated time. Statistics reported here are of a further 10 minutes of simulation at a time step of 0.1 seconds. The simulated discharge matched the peak flow release of March 2008, which had duration of about 60 hours. The inlet flow discharge of the model was set to match the peak controlled flood flow discharges equal to 1200 m^3/s.

Numerical Methods and Governing Equations

The numerical algorithm is developed within the OpenFOAM environment. OpenFOAM is an open source Computational Fluid Dynamics (CFD) software written in C++. The numerical framework to resolve the flow equations uses a finite volume technique. This method performs very well at preserving quantities (such as mass and momentum) by calculating fluxes across the faces of each element. One disadvantage of the OpenFOAM finite volume technique is the difficulty of using high order schemes on an unstructured mesh. For our particular study, the model is built by a structured grid of hexahedron cells.

The LES equations are derived by applying a spatial filtering operation. Components of the equations that are greater than the spatial filter are termed filtered variables and are represented with an over-line. Components smaller than the spatial filter, termed sub-grid scale variables, are represented by a double prime.

The continuity and Navier Stokes equations are the governing equations for the flow field. These equations are shown below in terms of the LES decomposition:

Continuity $\frac{\partial \bar{u}_i}{\partial x_i} = 0$ (3.1)

Momentum $\frac{\partial \bar{u}_i}{\partial t} + \frac{\partial}{\partial x_j}\left(\overline{u_i u_j}\right) = -\frac{1}{\rho}\frac{\partial \bar{p}}{\partial x_i} + \frac{\partial}{\partial x_j}\left((\nu' + \nu'_t)\frac{\partial \bar{u}_i}{\partial x_j}\right)$ (3.2)

Where $\bar{u}_i$ and $\bar{p}$ are the filtered velocity and pressure components, ρ is the density, ν is the molecular viscosity, ν_t is the eddy viscosity and S_{ij} is the rate-of-strain tensor. The term containing the molecular viscosity and eddy viscosity $(\nu' + \nu'_t)$ represents the unresolved sub-grid (SGS) stress tensor, and it is modeled using the Spallart Allmaras (S-A) turbulence closure. The S-A model has the advantage of being a non-zonal technique, implying that one single momentum equation (equation 3.2) is used with no *a priori* declaration of RANS versus LES zones. The length scale $(\tilde{d})$ of the S-A model is equal to the minimum of the distance to the bed or banks, *d*, and the length scale, proportional to the local grid spacing. Hence, $\tilde{d} = min(d, C_{DES}\Delta_G)$ provides a way to make a transition between RANS and LES by retaining RANS within the boundary layer when $\tilde{d} < d$ and applying LES to the zone away from the bed or banks when $\tilde{d} \geq \Delta_G$ (Squires 2004).

Computational Domain

To build the computational domain, a program was written in OpenFOAM to automatically construct the block-hexagonal grid between a triangulated surface extracted from a digital elevation model of the river reach and a calculated water surface elevation.

The water surface elevation was calculated using a two-dimensional depth-averaged flow model also written in OpenFOAM.

A one-parameter hyperbolic tangent stretching function was employed along the vertical axis to distribute the vertical cell space(*s*). The purpose of this stretching function is to maximize the accuracy at simulating the smallest eddies protruding from the river bed. The stretching function allows the near-bed cells to be finer and gradually increase towards the surface water level.

The one-parameter hyperbolic tangent stretching function is defined as:

$$s(i) = 1 + \frac{tanh[\delta(iI-1)]}{tanh(\delta)} \tag{3.3}$$

Where *s* is the space between each cell, δ is the stretching factor, *i* is the cell number, and *I* is the total number of cells. The stretching factor used for developing this model is equal to 1.5 over 25 vertical cells.

Domain decomposition is employed to break up the grid in sub-domains each assigned to multiple computational processors to reduce computational workload. Open MPI provides communication between the networking of processors allocated at ASU Advanced Computing Center (A2C2 – Saguaro supercomputer). The model has shown very good scalability up to at least 128 processors.

The current grid resolution is appropriate because it guarantees fully developed turbulence and reproduces the vortex structures that otherwise are not captured by coarser grids in three-dimensional DES models, as it is shown in Video 3.1 (See Appendix C) and Figure 3.5(a). Results from a coarser grid resolution (800,000 cells) demonstrate the

insufficiency of this grid spatial resolution to reproduce vortex structures and recirculation flows (see Video 3.2 in Appendix C and Figure 3.5(b)).

(a)

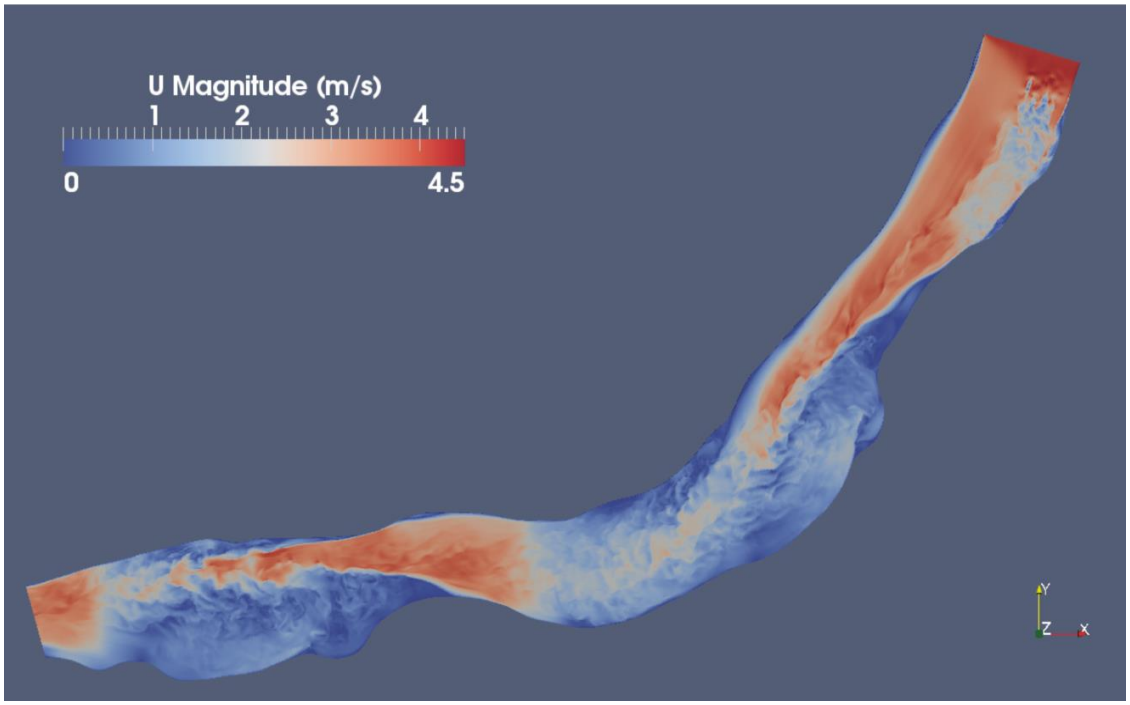

(b)

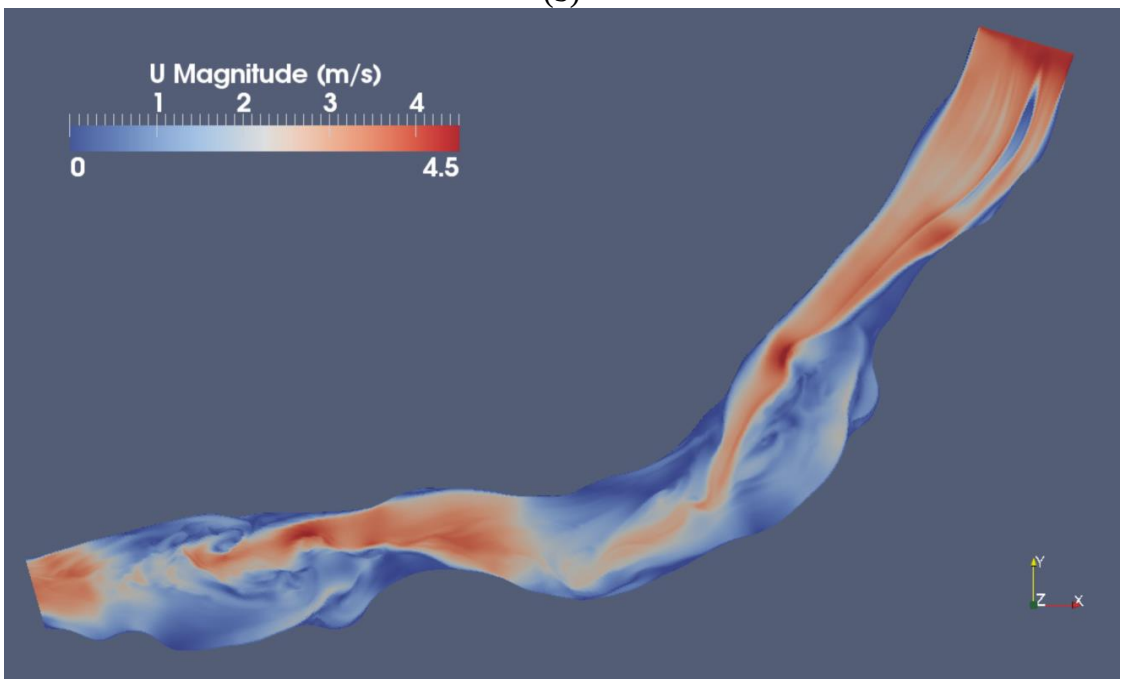

Figure 3.5. Snapshots of instantaneous water surface velocity magnitude for (a) fine grid (5,625,000 cells) and (b**)** coarser grid (800,000 cells) taken at time equals to 1000 second.

Boundary and Initial Conditions

The boundary roughness is imposed by means of a rough wall extension of the S-A model. The S-A model was designed originally for smooth bed applications. A wall viscosity approach, utilizing a local bed roughness scale is used to account for the hydraulically rough-bed. The wall distance *d* is modified to include the rough wall extension as follows: $d = d_{smooth} + 0.03k_s$. The turbulent viscosity values (ν'_t), for roughness walls, are now expected to be non-zero at the bed. The rough wall function (Boeing extension formulation) replaces the wall condition $\tilde{v} = 0$ by $\frac{\partial \tilde{v}}{\partial n} = \frac{\tilde{v}}{d}$ where *n* is a normal wall distance variable and $\tilde{v}$ is a transported quantity associated with the eddy viscosity (Aupoix and Spalart 2003).

The velocity boundary conditions are no-slip at the bed and free slip (zero stress) at the water surface and all lateral boundaries. A constriction at the inlet boundary is used to cause perturbation to guarantee fully developed turbulence. The solver algorithm of velocity-pressure coupling is Pressure Implicit Splitting of Operators (PISO) for time dependent flows. PISO is a pressure correction scheme used to calculate the pressure distribution correction to drive the local velocity field towards a result that satisfies both momentum and continuity (Ferziger and Peric 2002). A gravitational term is included in the two-dimensional model used to determine the water surface elevation for the three-dimensional model. However, gravitational force is not included in the solved equations of motion. As such, the pressure solution includes non-hydrostatic pressure and the pressure necessary to drive the flow.

RESULTS: MODEL VALIDATION

A common technique to evaluate a fluvial model is by scatter plot comparisons between observed and simulated data (e.g Lohmann et al. 1996; Nicholas and Sambrook Smith 1999; Zealand et al. 1999; Cigizoglu 2004; Kang and Sotiropoulos 2011). This scatter plot comparison is often used when field data are scarce. The estimation of advanced skill metrics for validation of high resolution distributed flow and sediment models usually requires long-term, temporally-continuous, and spatially-distributed field monitoring data. Other geosciences such as hydrology and climatology have made significant advances in the development of skill metrics to validate numerical model predictions (Gupta et al. 2008; Yilmaz et al. 2008; Wilks 2011). These fields have evolved rapidly in the context of focused efforts by the scientific community to resolve pressing societal issues such as climate change and flood and drought forecasting. As a consequence, the availability of on-the-ground data and remotely sensed information for these purposes is also more extensive (e.g. Horel et al. 2002; Dunn et al. 2012; Wahl and Smerdon 2012), leading to significant advances in model verification and calibration. Accordingly, research studies, in this particular field, are oriented to the use of statistical skill metrics to quantitatively assess hydrologic and climatologic model results (e.g Sharif et al. 2004; Gupta and Kling 2011; Martinez and Gupta 2011; Moreno et al. 2014). Among the most common statistical skill metrics are the Mean Squared Error (*MSE*), Nash-Sutcliffe Efficiency Index (*NSE*) and Pearson correlation coefficient, Maximum Likelihood Estimates (*MLE*), Kolmogorov-Smirnov test, the Mean Absolute Error (*MAE*), Mean Absolute Percent Error (*MAPE*), Mean Forecasting Error (*MFE*), and the statistical moments of density functions. The metrics chosen to perform a validation

depend on (a) the set of diagnostic measures (including type and number), (b) model variables to be validated, and (c) the scale of the model outputs. The type of validation performed can be temporally- and/or spatially-distributed and/or point-to-point; and it will be constrained by the set of diagnostic measures (data set) and by the temporal and spatial scales of the model (Wilks 2011). In this section, a framework for validation of CFD models in rivers is suggested, as commonly adopted from hydrology and climatology. These framework and skill metric techniques are aimed at evaluation of the spatially-distributed velocity field.

The forecasting capabilities of the three-dimensional DES flow model are assessed using a point-to-point verification method and a spatial distribution analysis of the magnitude and direction of velocity throughout the model domain. The data set is obtained from ADCP measurements (see details in the introduction section) taken twice a day. A temporal validation is not feasible to perform in this case, because data and simulations are not temporally compatible. On one hand, data were not collected continuously over the 60 hours of peak discharge. Furthermore, in model application, it is assumed that 10 minutes of simulation are sufficient to compute the statistics of the flow. Consequently, a point-to-point comparison of time-averaged quantities is the most suitable option for this model validation. Accordingly, time-averaged simulated velocities are compared against time-averaged observed velocity data at 4920 collocated points along transects (see location of transect lines in Figure 3.4). These points are selected from the computational domain to exactly match the river locations. Simulated velocity data are collected at each point by averaging the results of 10 minutes of simulation at every time step (equal to 0.1 seconds).

Velocity magnitude and direction are evaluated individually with different metrics. The spatiotemporal properties of velocity magnitudes are assessed based on probability density and cumulative distribution functions and six skill metrics. The skill metrics include four absolute error metrics: Mean Absolute Error (*MAE*), Mean Forecast Error (*MFE*), Root Mean Square Error (*RMSE*) and Pearson correlation coefficient (*R*); and two relative error metrics: Mean Absolute Percentage Error (MAPE) and Median Absolute Percentage Error (*MdAPE*). Velocity directions are evaluated by computing the dot product between simulated and measured velocity unit vectors (see Appendix D for details regarding the equation of each skill metric).

Six forecasting metrics were selected as they can provide a holistic diagnosis of the model. A model validation based on one or two metrics could lead to misinterpretation as some forecasting metrics could present drawbacks depending on the simulated data distribution. The use of six metrics helps to compensate for shortcomings in the metrics. For instance, the *MAE* metric equally weights the differences between simulated and observed values, which tend to amplify the error in surface velocities. In compensation, the *MAE* skill metric is contrasted against relative error metrics such as *MAPE* and *MdAPE* that normalized the errors by the observed value. These metrics are a simple way for validation, but they also present shortcomings in the near-bed velocities due to small values in the denominator. The *MFE* is a useful metric to measure the tendency of the model to under-forecast or over-forecast, however this metric does not assess the spatial distribution of the simulated data. *RMSE* and *R* coefficient are estimated to support the *MAE*, *MAPE* and *MdAPE* and *MFE*. The *RMSE* and *R* coefficient metrics are essential to measure the standard deviation of the error and the correlation between

the observations and simulations respectively. Finally, the direction of the velocity vector is well represented by one skill metric; the dot product evaluates the angle between each measured and simulated velocity angle.

Analysis of the Probability Density and Cumulative Distribution Functions

The probability distribution functions of both observed and simulated data are positively skewed with a step pattern presented on the right limb of the distributions (see Figure 3.6(a)). This step effect is an artifact caused by the measurement of velocities at discrete depth intervals. In general, the distributions illustrate a good fit between of the observed and simulated density and cumulative functions (Figure 3.6(a) and Figure 3.6(b)). Table 3.1 illustrates such statistical similarities through the moments of the distributions. The mean of the observations versus simulations is equal to 1.47 and 1.51; the variance is reported as 0.796 (observations) and 0.790 (simulations); the skewness presents the largest difference between velocity magnitudes with 0.559 (observations) and 0.481 (simulations). In other words, the mean and variance differ by 2.7% and 0.8% respectively, while the skewness differs on 14%. The difference in skewness is reflected by the slight displacement of the simulated value relative to the observed probability distribution function. This behavior may be related to the nature of the method used for field measurements versus the method used for simulated data collection as field data are averaged over 10 m bins and assigned to specific coordinates, while the simulated data are collected punctually at each model coordinate (see Figure 3.6(a), Figure 3.6(b) and Table 3.1).

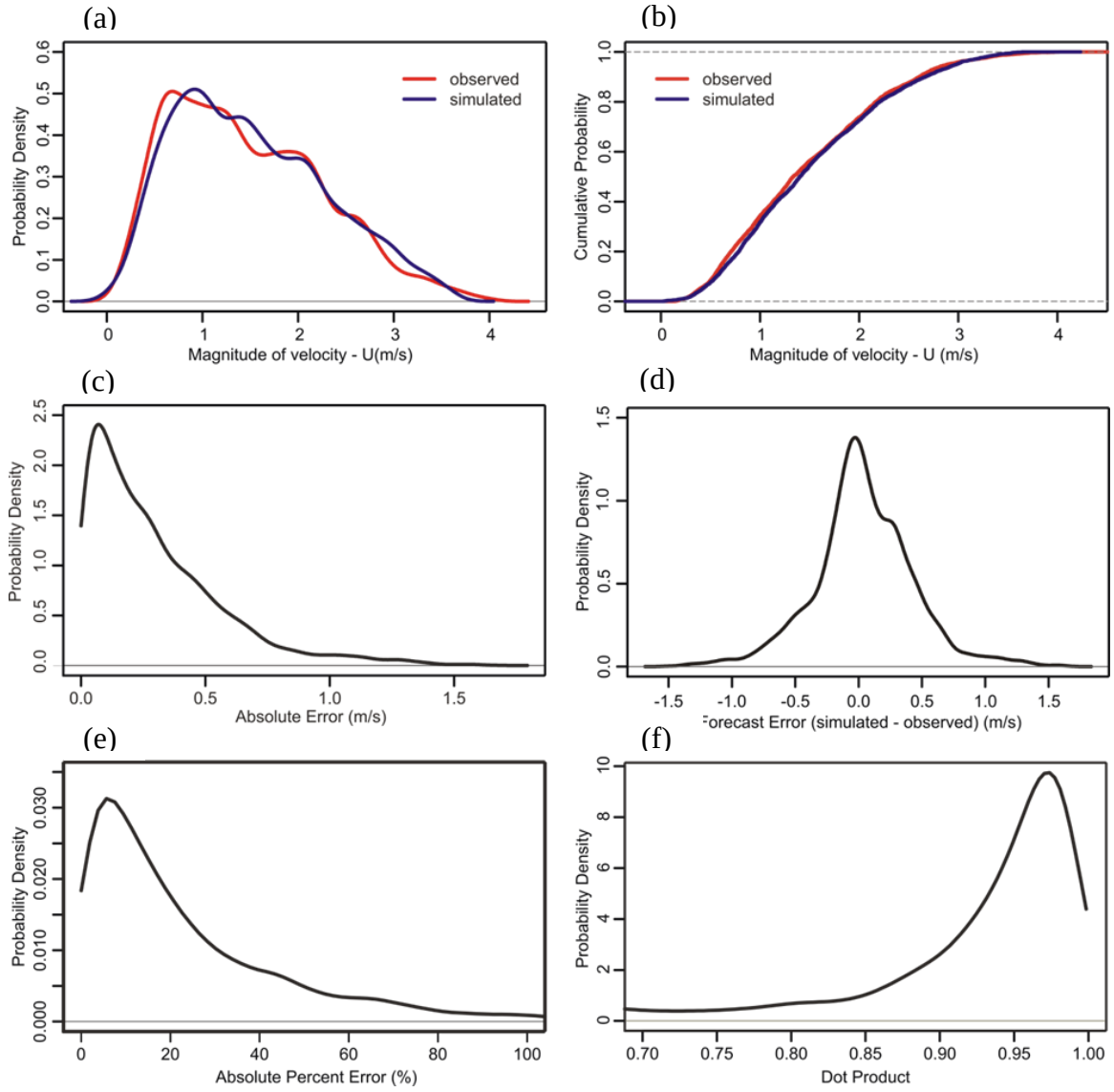

Figure 3.6. Statistical comparison of model velocity values and field measurements: **(a)** Probability density function of 4920 ADCP velocity measurements in red, and the DES-3D time-averaged velocity magnitude of the collocated 4920 points in blue. **(b)** Cumulative probability function of the observed measurements in red versus simulated results in blue. (**c)** Probability density function of the Absolute Error (m/s). **(d)** Probability density function of the Forecast Error (m/s). (**e)** Probability density function of the Percent Error (%). (**f)** Probability density function of the Dot Product between the measured and modeled velocity vectors.

Table 3.1. Summary of the statistics used for model validation[a].

Metrics	Min	1st Quartile	Median	Mean	Standard deviation	Skewness	3rd Quartile	Max
Observations	0.128	0.812	1.334	1.470	0.796	0.559	2.041	4.013
Simulations	0.019	0.870	1.402	1.510	0.790	0.481	2.065	3.651
Absolute error (m/s)	0.00002	0.091	0.223	0.296[b]	0.270	1.543	0.421	1.672
Forecasting error (m/s)	-1.672	-0.275	-0.021	-0.04[c]	0.398	-0.081	0.167	1.522
Percent Error (APE) (%)	0.001	7.023	16.250[d]	29.0[e]	45.81	6.990	35.047	953.48
Dot product	-0.761	0.854	0.944	0.834			0.973	0.999

[a] *RMSE*=0.4m/s, Pearson correlation coefficient (*R*)=0.874, [b]*MAE*=0.296 m/s, [c]*MFE*=-0.04 m/s, [d]*MdAPE*=16.25 %, [e]*MAPE*=29%

Absolute Forecasting Error Metrics

Model results exhibit good fit with observed and simulated values as indicated by error and skill metrics. For example, the correlation coefficient (*R*=0.874) shown in Table 2.1 indicates a high linear correlation between observed and modeled flow velocity, while the *RMSE* (0.4 m/s) and *MAE* (0.29 m/s) are relatively small values considering the range of measured velocities from 0.13 m/s to 4m/s. The sample distribution of the absolute error values range from 0 to 1.7 m/s with 75 percent of the data (3rd quartile) less than 0.42 m/s (see Figure 3.6(c)). Absolute error values above the upper fence equal to 0.91 m/s are considered outliers (see Table 3.1). The mean forecast error (*MFE*) is found to be -0.04 m/s meaning a small underestimation of values (Figure 3.6(d)).

The difference between observed and modeled velocity is not spatially uniform. Errors tend to be greater near the separation zone in the near-bed grids and along the right channel margin (Figure 3.7). At EM, the absolute error ranges from 0.8 m/s to 1 m/s near the separation zone and from 0 to 0.4 m/s in the eddy and throughout most of the main

channel (Figure 3.7(a)). Absolute errors are lower at WT, and range from approximately 0 to 0.22 m/s throughout most of the model domain (Figure 3.7(b)). Based on the absolute error metric, the DES-3D model demonstrates higher predictive capabilities at WT in comparison with EM.

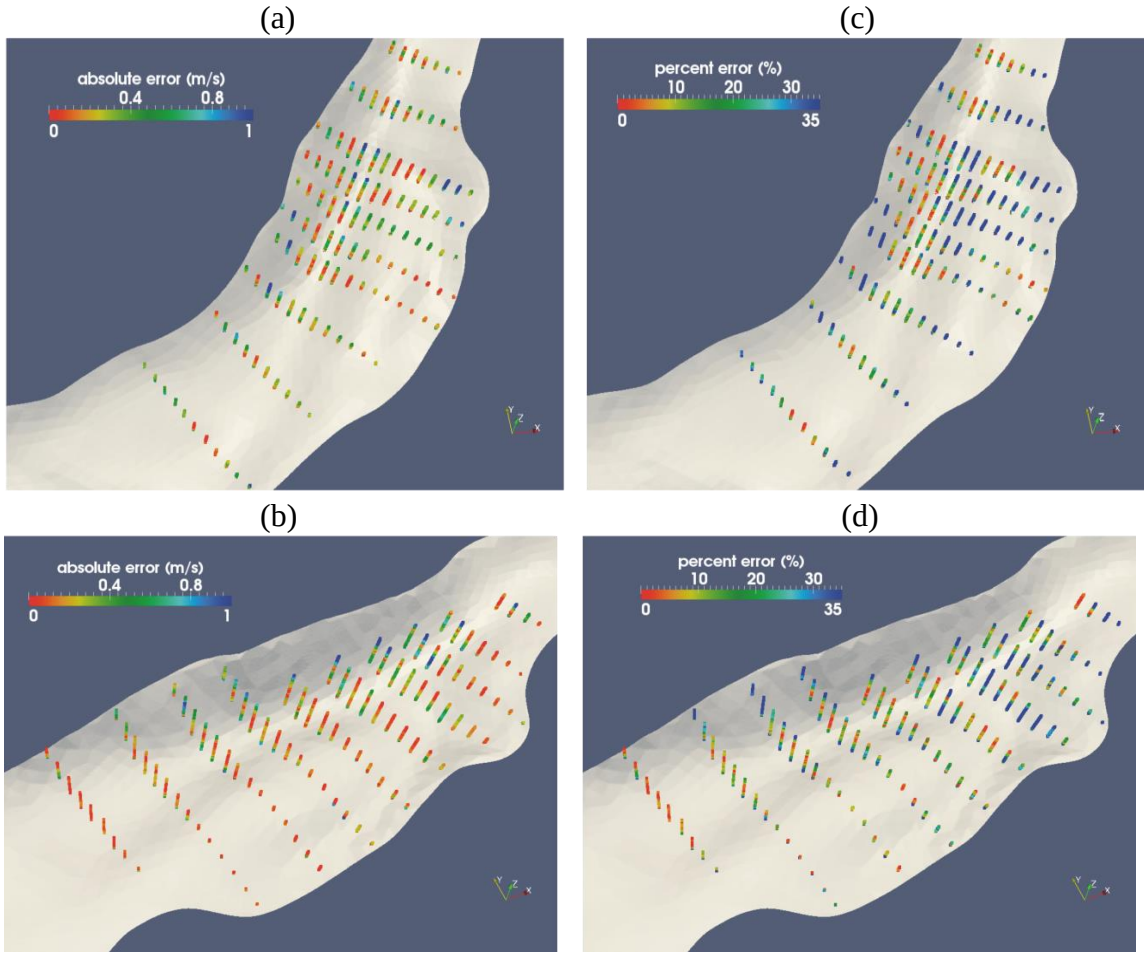

Figure 3.7. Spatial variability of Absolute and Percent Errors. (a) Spatial variability of Absolute Error (m/s) calculated using the DES-3D models at 4920 collocated points along 10 transect lines at EM fan eddy complex and, **(**b) 10 transect lines at WT fan eddy complex. The bar scale indicates 0 in red and 1 m/s (upper fence above 0.91m/s) in blue. (c) Spatial variability of the Percent Error (%) calculated using the DES-3D models at 4920 collocated points along 10 transect lines at EM fan eddy complex and, (d) 10 transect lines at WT fan eddy complex. The bar scale indicates 0 in red and 35% (3rd quartile) in blue.

Regarding the outlier values, Figure 3.7(a) and Figure 3.7(b) report few values above the upper fence (0.91m/s). At both eddy fan complexes, most of these values are located near the water surface, along the main channel, close to the left shore and opposite to the lateral separation zone (right shore) (Figure 3.7(b)). At the EM site, a few outlier values are also found downstream of the separation zone within the lateral separation zone and near the water surface. Outlier values of absolute error are likely to occur near the water surface since velocity values are the highest which could possibly lead to higher differences between measured and simulated velocities. This trend is not observed in the spatial distribution of Absolute Percent Error (*APE*) since this metric is weighted by the measured velocity (see Figure 3.7(c) and Figure 3.7(d)).

Relative Error Metrics

The probability density function of the Absolute Percent Error (*APE*) is positively skewed, which may be caused by outliers associated with measured velocities that are small or close to zero. Small values of measured velocities found in the field data sample support our hypothesis. The smallest measured velocities are considered below the first quartile with values ranging between 0.13 m/s and 0.81 m/s (see Table 3.1). To avoid the influence of these outlier values, the best estimate for the *APE* is probably the *MdAPE* (16.25%) instead of *MAPE* (29%), because this metric does not include the heavy right tail of the *APE* data distribution. As a result, it is appropriate to report the percent error in velocity magnitude as less than 17% based on the *MdAPE* (see Figure 3.6 and Table 3.1) for the entire domain.

The spatial distribution of *APE* at EM ranges from 0 to 25% upstream of the separation zone in the first rapid (transect 1), and downstream of the reattachment bar

(transect EM 9 and EM 10) (See Figure 3.7(c)). Results above 35% are found along the separation zone, transect EM 2, along the separation bar, transect EM 3, and at the reattachment bar, transect EM 8. The distribution of *APE* values at WT range between 0 to 20% at the eddy recirculation zones in the primary eddy (transects WT 6, WT 7 and WT 8), and near the reattachment zone (transect WT 9) (Figure 3.7(d)). *APE* values ranging from 25% to 35% can be found at the first rapid and separation zone (transects WT 1 and WT 2), and the secondary eddy zone and return current (transects WT 3, WT 4 and WT 5) (Figure 3.7(d)). The results of the spatial distribution of *APE* are consistent with the pattern observed through the absolute error metric. Prediction of the DES – 3D model in WT fan eddy complex is better than EM based on the spatial variability of the *APE* and absolute error.

The analysis of outliers demonstrates that at both fan eddy complexes the *APE* values above the 35% are positioned near the separation and reattachment bars in shallow waters and near-bed grid cells of the main channel. High values of *APE* could be possibly associated with relatively small measured velocity values, found close to the river bed.

Validation of the Direction of Velocity Field

The probability density function of the dot product between the observed and simulated vectors shows negative skewness (see Figure 3.6(f)). The dot product values range from -0.76 to 0.99. Values less than 0.86 represent 25 % of the distribution and values below 0.68 (lower fence) are considered outliers. Similar to the *APE* density distribution, the most useful estimator is the median of the dot product (equal to 0.94), because this metric discards the influence of the outliers. The corresponding angle to dot product value of 0.94 is 19.3 degrees. Hence, the time and spatially-averaged difference

between the simulated and measured velocity vectors is equal or less than 19.3 degrees for the entire domain for half of the vectors (see Table 3.1 and Figure 3.6(f)).

RESULTS: FLOW STRUCTURES

Lateral Recirculation Flow Features

The objective of this section is to assess the capabilities of the DES – 3D model in capturing the major recirculation currents present in the fan-eddy complex (see Figure 3.1). The assessment is based on a comparison of the DES - 3D model (Figure 3.8(a) and Figure 3.8(b)) against a two-dimensional depth-averaged closure flow model (Figure 2.8(c) and Figure 3.8(d)). The two-dimensional depth-averaged flow model was developed within OpenFOAM environment and employs a shallow water equation with a friction coefficient to solve the flow field. For comparative purposes, results from the DES – 3D model are time- and depth-averaged to display velocity vectors in a two dimensional view. The center of rotation (eddy eye) and reattachment point determined from the measurements made during the 2008 controlled flood are used as fixed reference points (Figure 3.8). Likewise, the red and yellow dots symbolize the eddy eyes (approximate center of lateral separation eddy rotation) and reattachment points estimated from the modeling.

Results obtained from the DES-3D model capture the flow deceleration at the expansion from rapid to pool at both sites (see Figure 3.8(a) and Figure 3.8(b)). Consequently, the diffusion of the velocity field along the main channel in the transition from the rapid to pool is well simulated by the DES-3D model at both sites. Conversely, the 2D depth-averaged model does not reproduce this process since relatively high

velocities are a pattern along the main channel in the transition to the pool (see Figure 3.8(c) and Figure 3.8(d)). These high velocities are more evident at WT, while low diffusion of the velocity field is observed at EM.

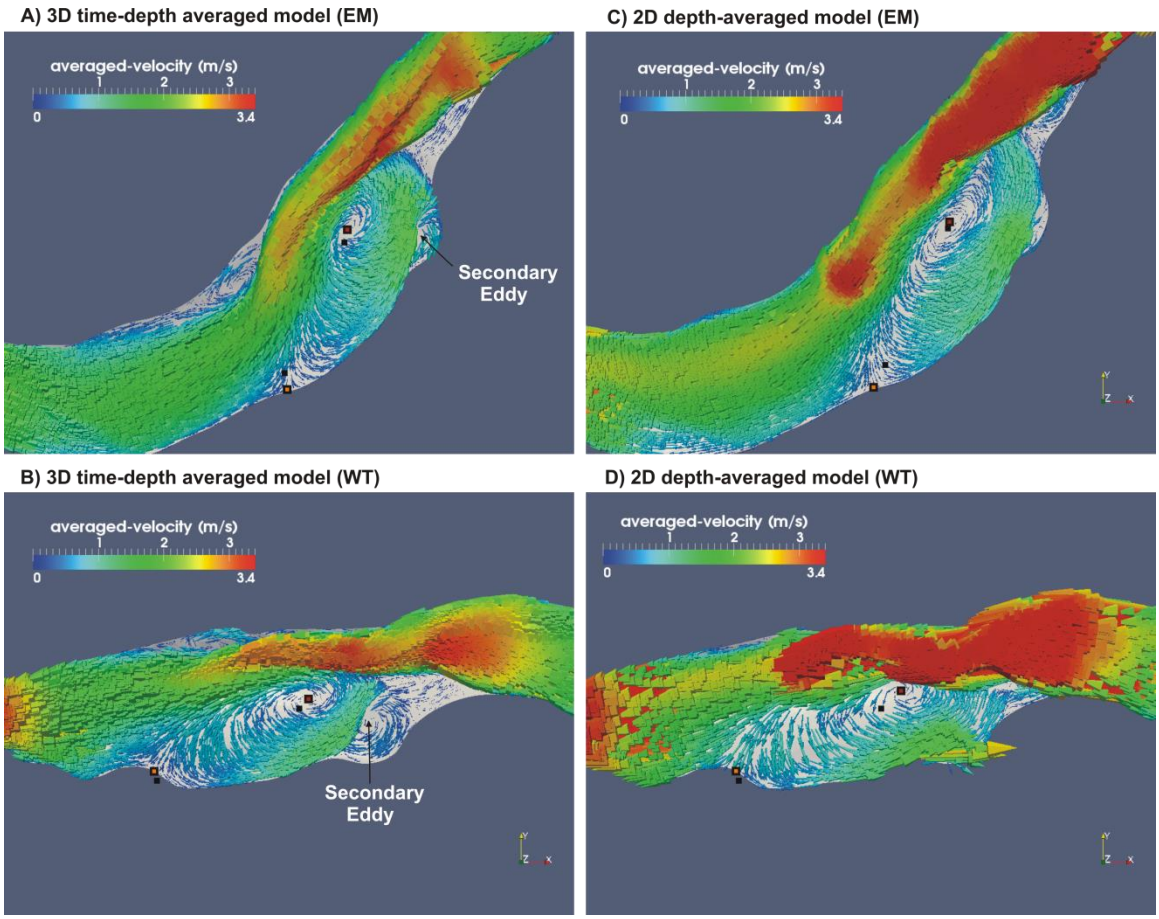

Figure 3.8. Comparison of lateral recirculation flows between the three-dimensional DES model and the two-dimensional depth-averaged model. (a) Three-dimensional DES model at EM; (b) Three-dimensional DES model at WT. (c) Two-dimensional depth averaged model at EM; and (d) Two-dimensional depth averaged model at WT. Notes: the DES – 3D model is time- and depth-averaged to display a two-dimensional front view. Black dots represent the eddy eye and reattachment point determined from the field observations. The red and yellow dots symbolize the eddy eyes and reattachment points estimated from the modeling.

The DES – 3D model reproduces the main recirculation zone or primary eddy and the secondary eddies at both sites (Figure 3.8(a) and Figure 3.8(b)). The size and shape of these primary and secondary eddies are exhibited differently at each site. For instance,

EM exhibits a large primary eddy characterized by a strong return channel and a relatively small secondary eddy (see Figure 3.8(a)). On the other hand, WT exhibits a relatively smaller and thinner primary eddy constrained by a downstream debris fan that determines the length of the primary eddy and the location of the reattachment point. Furthermore, the return current is a short and narrow transition to a very strong secondary eddy. In addition, the modeling results corroborate the presence of a tertiary and smaller eddy in WT, downstream from the separation zone (Figure 3.8(b)) observed in the field during the peak of the 2008 controlled flood and reported in Wright and Kaplinski (2011).

Relative to the DES – 3D model, the 2D turbulence closure model predicts one primary large and elongated eddy at EM. The width of the return current is narrower and the secondary eddy is hardly captured at EM (Figure 3.8(c)). WT results show the highest discrepancies between models. The 2D model does not capture the strong secondary recirculation zone at WT, which is well predicted using the DES-3D (Figure 3.8(d)). Instead, the secondary eddy is replaced by high flow velocities found mainly near the separation bar. This abnormal flow behavior occurs mainly along the return current where the flow tends to accelerate from the reattachment zone towards the separation zone (Figure 3.8(d)).

The eddy eyes and reattachment zone points are identified very close to the observed points at both sites using the DES-3D model. This implies a correct simulation of the total length and size of the lateral separation zones by the DES-3D (Figure 3.8(a) and Figure 3.8(b)). The 2D turbulence-closure model also demonstrates an accurate prediction of the EM eddy eye and WT reattachment zone (Figure 3.8(c) and Figure

3.8(d)). However, the EM reattachment zone is found downstream of the observed point, which indicates an oversized primary eddy (Figure 3.8(c)). The eddy eye at WT is identified upstream of the observed eddy due to the lack of a secondary recirculation zone using the 2D model (Figure 3.8(d)).

In general, the DES-3D model is more precise at predicting the flow patterns of the lateral recirculation zone in comparison with a two-dimensional depth-averaged turbulence closure model. In contrast, the two-dimensional depth-averaged turbulence closure model captures an oversized steady primary eddy and it does not reproduce the secondary eddy and the return current at both sites.

Three Dimensional Flows and Eddy Structures

The purpose of this section is to describe the flow field in three dimensions based on the DES-3D model. To identify the flow properties, several simulation videos and figures were produced focusing on: (1) Cross-sectional panels (Figure 3.9(a) and Figure 3.9(b)), (2) velocity vector structure (Videos 3.3 and 3.4 and Figure 3.10), (3) directional distributions (Figure 3.11), and (4) vorticity and Q-criterion (Videos 3.5, 3.6 and 3.7 and Figure 3.12 and 3.13).

Cross-sectional Panel View

The cross sectional views in Figures 3.9(a) and Figures 3.9(b) identify flow patterns based on the magnitude and direction of the cross-stream and vertical velocity components in relation to the downstream velocity and location.

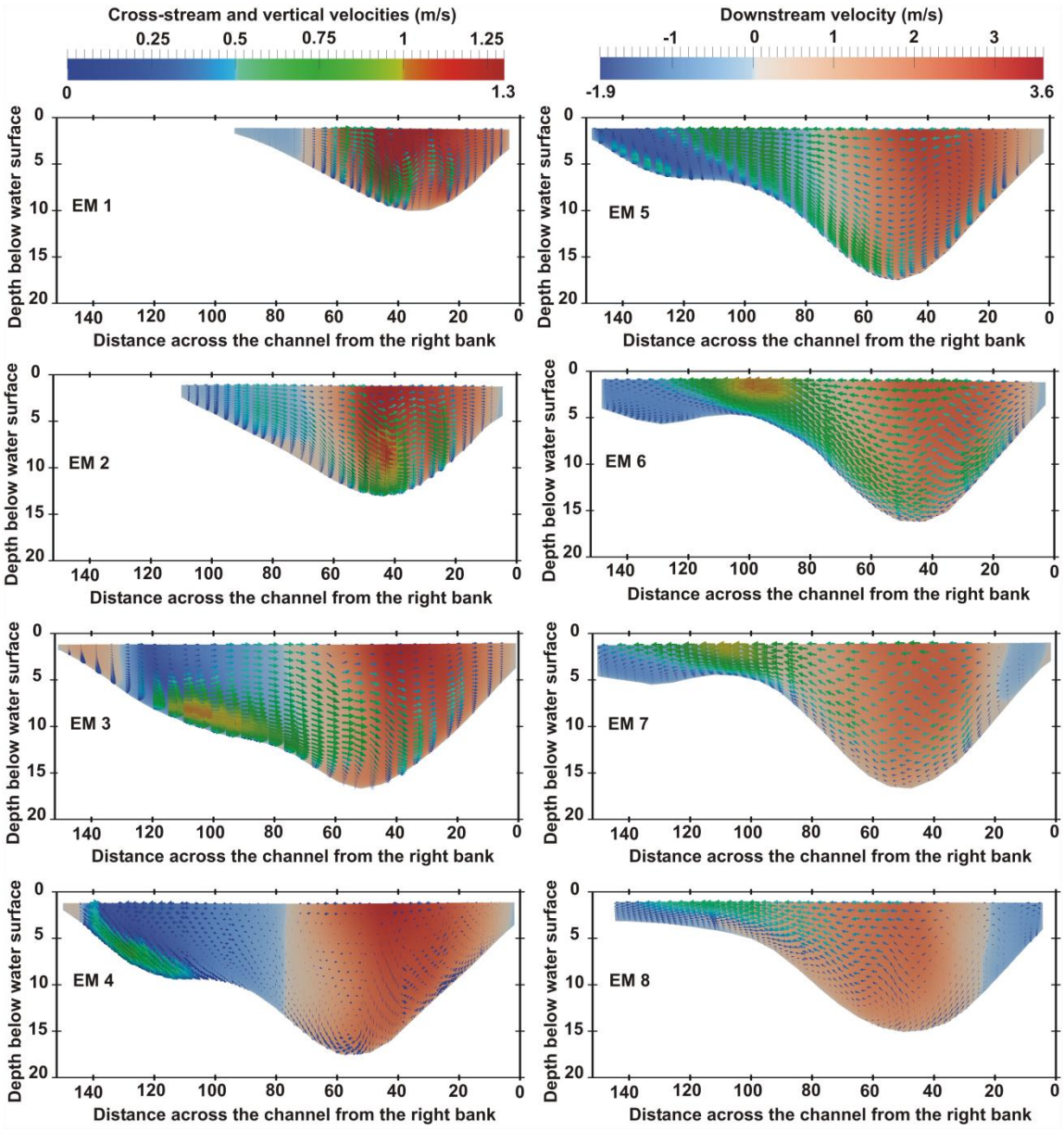
Cross-stream and vertical velocities (m/s)
0.25 0.5 0.75 1 1.25
0 1.3
Downstream velocity (m/s)
-1 0 1 2 3
-1.9 3.6
EM 1
EM 2
EM 3
EM 4
EM 5
EM 6
EM 7
EM 8
Depth below water surface
Distance across the channel from the right bank
0 5 10 15 20
140 120 100 80 60 40 20 0

(a)

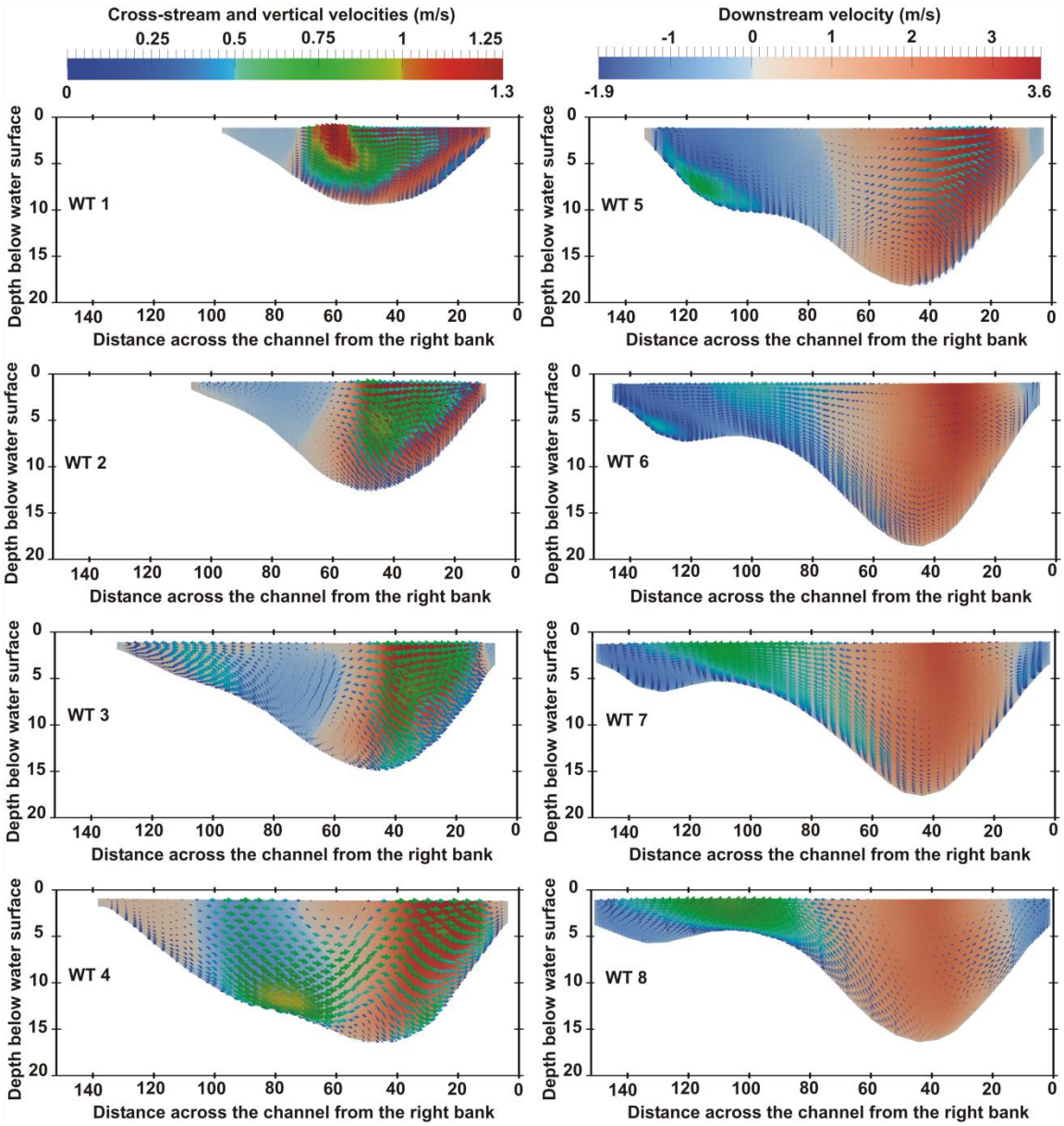

(b)

Figure 3.9. Cross-sectional panel views of the mean velocity field estimated by the 3D - DES model along (a) EM and (b) WT eddy-fan complexes. The cross-sections are corresponding to the transect lines of the ADCP surveys. Cross-stream and vertical velocity components are displayed as arrow vectors; zero velocity is shown in blue and the maximum velocity equal to 1.3 m/s in red. The downstream velocity component is displayed as solid color with red and positive meaning downstream direction and, blue and negative upstream direction. Notes: cross sections EM 9 and EM 10 are not shown since they are far downstream of EM eddy-fan complex.

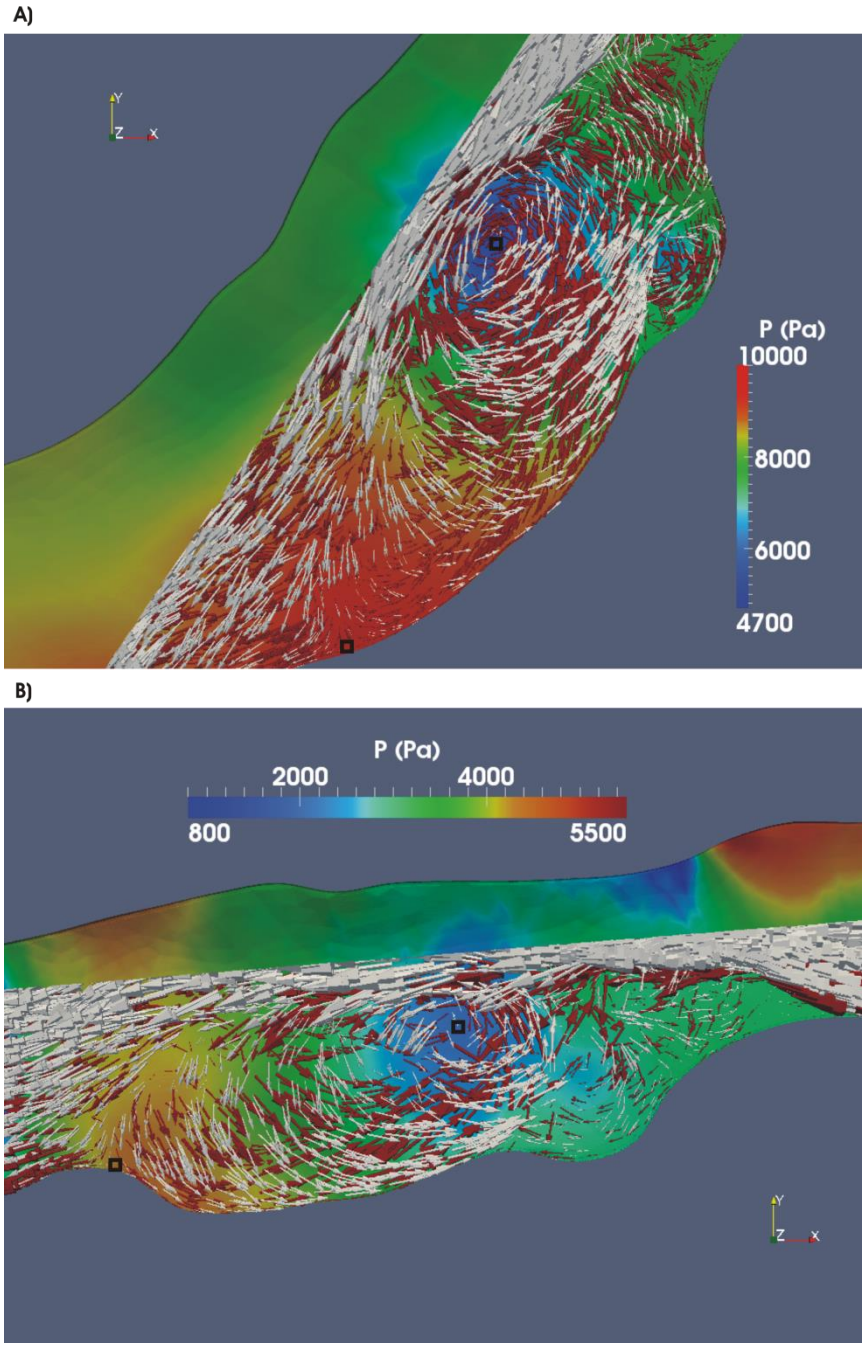

Figure 3.10. Snapshots of the mean surface velocity vectors, in white, versus mean near-bed velocity vectors, in red, at (a) EM and (b) WT eddy-fan complexes taken at time equals to 1000 second. Also shown the non-hydrostatic component of the pressure. The length of mean surface velocity vectors ranges from 0 to 4.5 m/s, and the length of the near –bed velocity vectors are scaled five times larger than the surface velocity vectors.

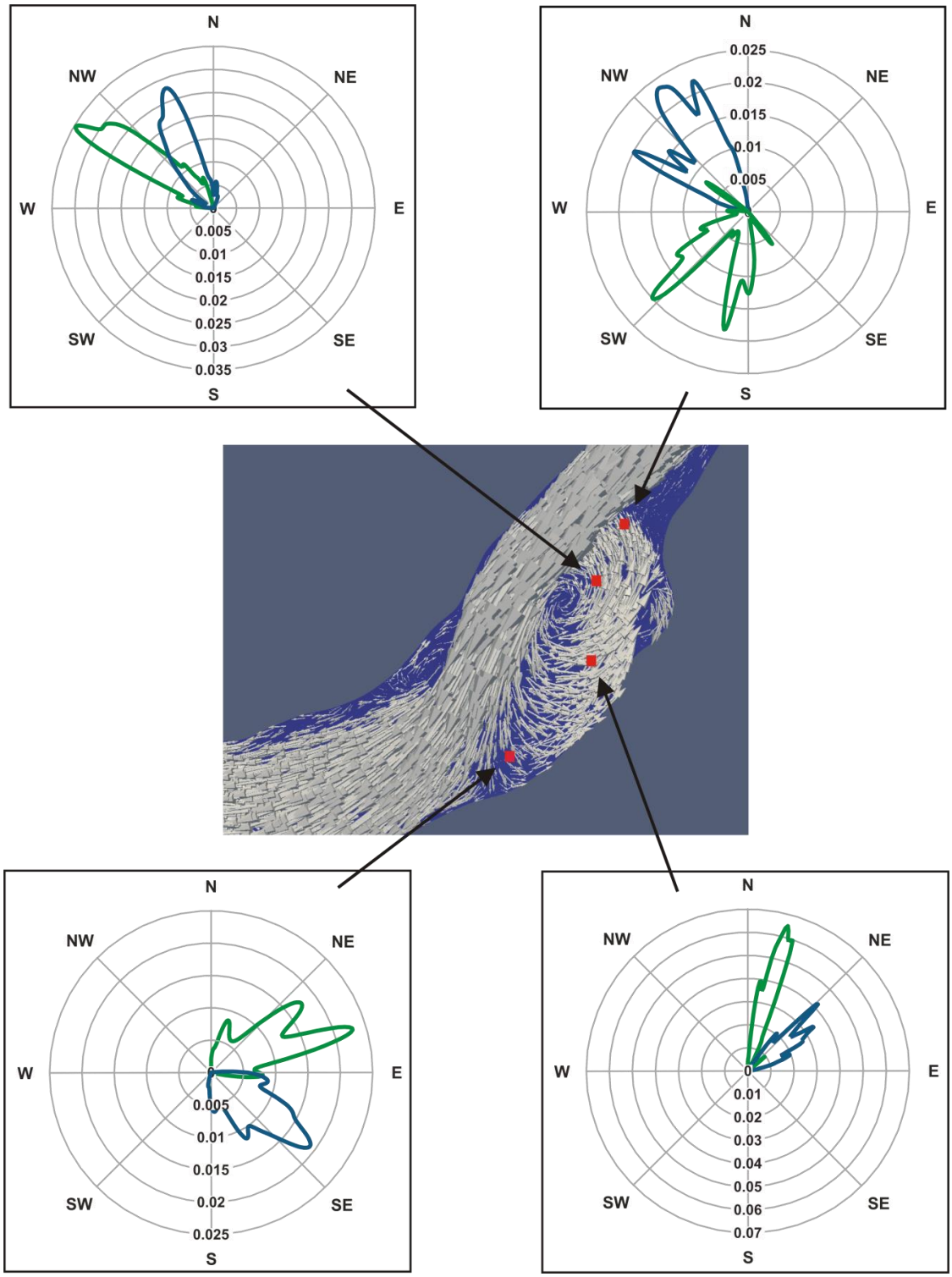

(a)

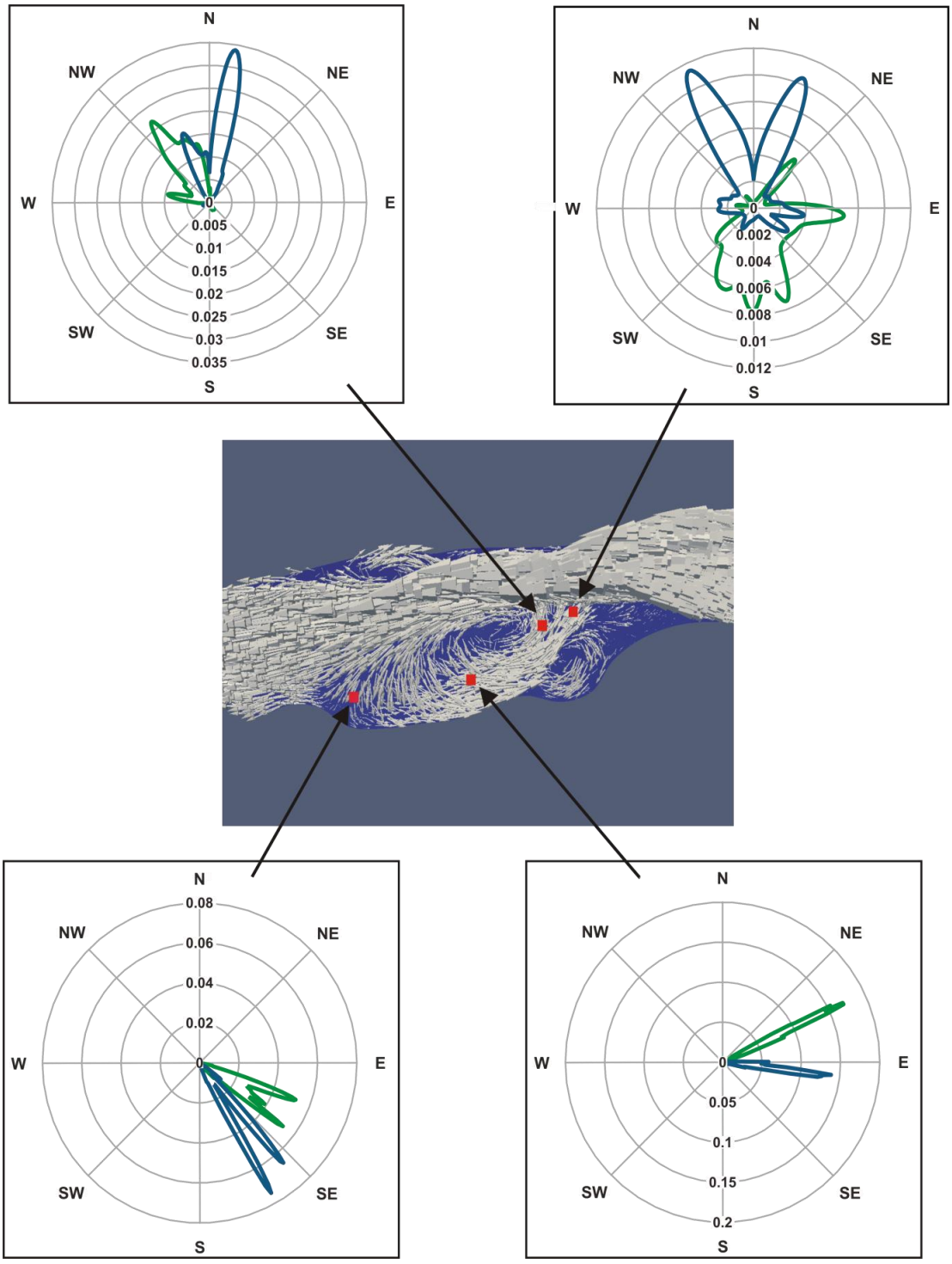

(b)

Figure 3.11. Directional distribution functions of near bed velocities, in green, and surface velocities, in blue, at (a) EM and (b) WT eddy-fan complexes.

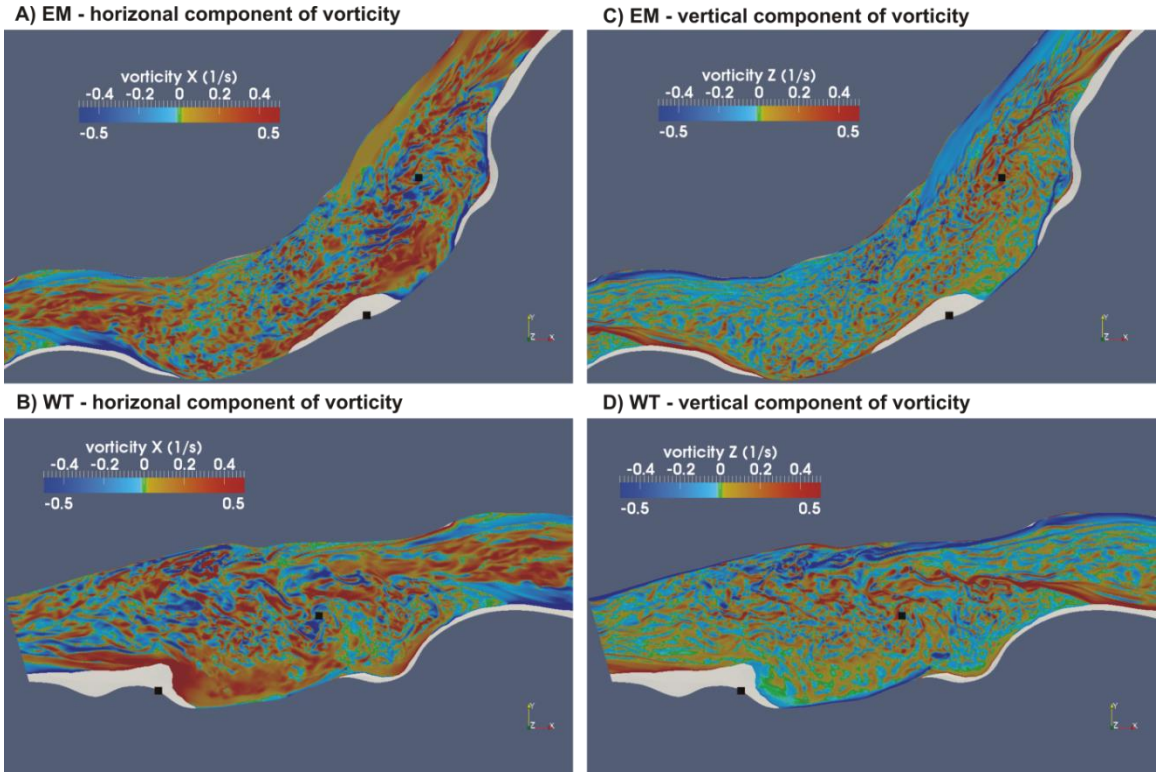

Figure 3.12. Snapshots of vorticity structures at EM and WT eddy-fan complexes taken at time equals to 1000 seconds. (a) Vertical component of vorticity at EM eddy-fan complex. (b) Vertical component of vorticity at WT eddy-fan complex. (c) Horizontal component of vorticity at EM eddy-fan complex. (d) Horizontal component of vorticity at WT eddy-fan complex.

The locations of the cross-sections (illustrated in Figure 3.4) correspond with the ADCP transect surveys. Cross-sectional panels are perpendicular to the main direction of flow allowing the decomposition of the velocity field into three vector components. The downstream (normal) velocity component is displayed as a color background, where downstream velocity is positive-red and upstream velocity is negative- blue. The cross-stream and vertical velocity components are displayed as parallel vectors to the cross-section views and the magnitude is shown in a color palette from blue to red. Cross sections 9 and 10, shown in Figure 3.4, are excluded from this analysis since they are far downstream of the eddy-fan complexes.

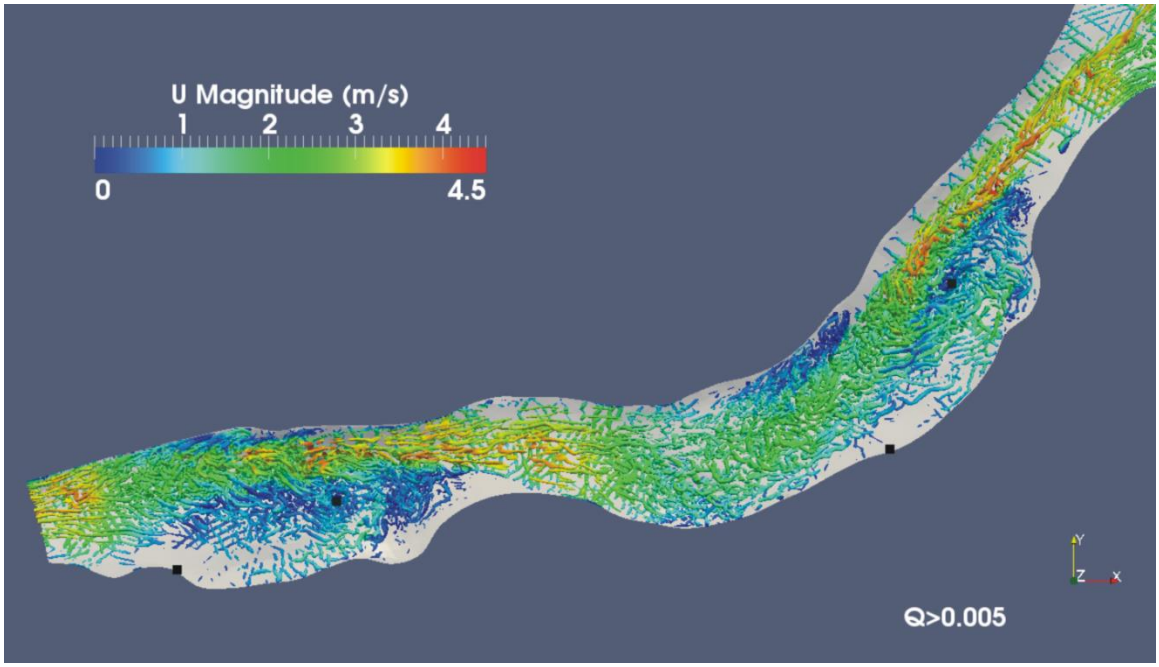

Figure 3.13. Snapshot of instantaneous contours of Q-criterion displayed by the velocity magnitude taken at time equals to 1000 second. Notes: Q>0 means that rotation dominates over shear stress.

Exchange between the main channel and recirculation zone is key to understanding bar sedimentation. In the rapids, water depth is shallow and the velocity magnitude is high. Flow separation begins in the initial sections at the left bank (EM1-EM2 and WT1-WT2). Cross stream velocity vector magnitudes are small and the upstream velocity is very weak in the separation zone. No exchange of flow between the separation zone and the downstream main channel is observed in the first two cross-sections at both sites. WT 3 exhibits a strong secondary eddy compared with EM 3. A small zone of divergence is formed at the return current directed towards the secondary eddy at WT3. This small divergence is evidenced by cross stream velocity vectors moving from the return current towards the left bank. WT3 and WT4 shows the presence of a tertiary eddy since the left bank is defined by downstream velocity followed by a transition to the secondary eddy defined by the upstream velocity.

EM 3 and WT 4 show flow exchange between the main channel and the lateral separation zone. Cross-stream velocity vectors are observed across the entire cross sections at EM3 and WT4 moving from the separation zone towards the main downstream channel, forming a zone of convergence between the return current and the main downstream channel flow. By conservation of mass, this convergence zone is compensated by increasing the downstream velocity magnitude. Cross-stream velocities are highest near the bed decreasing towards the water surface (see EM 3 and WT 4). This pattern occurs because the near bed velocities are oriented towards the eddy eye while surface velocities tend to recirculate. Figures 3.10 and 3.11 better illustrate this pattern.

The eddy eye is located near EM4 and WT5. Cross-stream velocity vectors decrease, indicating that there is little advective exchange of flow between the main channel and the lateral recirculation zone at the region near the eddy eye. Instead, this zone is dominated by high downstream velocities in the channel and a strong return flow in the lateral separation zone.

The cross-sections EM5 to EM8 and WT6 to WT8 encompass the reattachment zone. The cross-stream velocity vectors are oriented towards the lateral recirculation zone coming from the main channel. This pattern exhibits a zone of divergence of flow from the main channel to the reattachment zone. Although, a dividing streamline (actually a dividing surface) could be drawn between the points of separation and reattachment, flow convergence by the return current brings fluid (and sediment) from the eddy to the dividing streamline.

Downstream the eddy eye, velocity in the main channel decreases. By conservation of mass an increase on the cross-stream velocity magnitudes leads to

decreased downstream velocities. In comparison with the convergence of flow occurring near the dividing streamline downstream of separation, the divergence of flow approaching reattachment occurs more gradually. This pattern is observed on smaller values of cross stream velocity magnitudes near the reattachment zone (see panels EM5 to EM8 and WT6 to WT8) compared with the cross-stream velocity magnitudes shown for the separation zone upstream of the eddy eye (see panels (EM2 to EM3 and WT3 to WT4). Model results presented in this section are consistent with former cross-sectional flow panels plotted by Wright and Kaplinski (2011).

Velocity Vector Structures

The DES-3D model simulates the vertical profile of horizontal velocity vectors, allowing the identification of secondary flow structures. The differences between the velocity vector structures near the bed versus surface velocity vectors are captured in Videos 3.3 and 3.4 and Figure 3.10. These vector structures are analyzed in relation to the mean pressure field averaged over 10 minutes of simulation. For purposes of visualization, near-bed velocity vectors are scaled five times larger than surface velocity vectors. Figure 3.10 and especially Videos 3.3 and 3.4 demonstrate that the low pressure system formed near the center of the recirculation zone steers near-bed velocity vectors toward the low pressure center more than surface velocity vectors. This phenomenon occurs because the near-bed velocities are slower. Therefore, the momentum is weaker and cannot overcome the pressure force driving the near-bed velocity vectors towards the eddy eye. In contrast, surface velocities have the highest momentum; as a consequence, the same pressure forces have much less effect on the direction of the velocity vectors. As

a result, an inward vertical Ekman spiral is produced at the primary eddy centered in the eddy eye.

Rose diagrams have the purpose of displaying the directional distributions of near-bed and surface velocities (Figure 3.11(a) and Figure 3.11(b)). Four points are selected to represent the distribution of direction along the separation zones. These points are representative sites of the separation zone, reattachment zone and the return current. The direction of velocity is calculated with respect to the north using east (x) and north (y) component of velocities. The distribution functions are generated using 6000 values during 10 minutes of simulation. The results demonstrate the capabilities of the model to reproduce short-term temporal changes of the direction of the velocity vector. Higher temporal variability of velocity direction is observed at the separation and reattachment zones at EM and at the separation zone and return current at WT. The rose diagrams (Figure 3.11(a) and 3.11(b)) confirm the inward vertical Ekman spiral observed in Videos 3.3, 3.4 and Figure 3.12(a), 3.12(b), since in both figures and at every location, the direction of near-bed velocities tends to be more deflected towards the eddy eye than the direction of surface velocities. In other words, there is a consistent difference in the pattern of the near-bed velocity directions (in green), which are pointing toward the eddy, and surface velocity direction (in blue).

Vorticity Patterns

The patterns of vorticity of turbulence structures are illustrated in Video 3.5 and Figure 3.12. Large scale turbulence structures, with vorticity predominantly in the vertical direction, are produced at the shear layer between the main channel and the separation zone (see Video 3.5 and Figure 3.12(a), 3.12(b)). These turbulence structures

rapidly become three-dimensional downstream with no preferred orientation of vorticity. Vorticity patterns are also identified by the Q-criterion methodology (*Hunt and Durbin*, 1999) (see Video 3.6 and Figure 3.13). The Q-criterion identifies coherent vortex structures, as opposed to identifying structures by vorticity magnitude which is always large near boundaries with shear. Vortex structures displayed in Video 3.6 and Figure 3.13 do not indicate any orientation preference, confirming the pattern observed in Video 3.5 and Figures 3.12(a), 3.12(b).

High magnitudes of horizontal vorticity are predominant in shallow waters where the water depth is not sufficient to develop vertical vortices or three-dimensional vortices (see Video 3.7 and Figures 3.12(c), 3.12(d)). Therefore, high magnitudes of horizontal vorticity are predominant in the river shores. The largest values of horizontal vorticity magnitudes are found at the reattachment zones and reattachment eddy bars, at both sites, which are featured by shallow water depth (Nadaoka and Yagi 1998).

DISCUSSION

Three-dimensional turbulence-resolving hydrodynamic models, such as this DES-3D model, are valuable tools to identify and assess flow patterns that occur in lateral separation zones. Similar patterns have been identified by other authors using field data and/or laboratory experiments, thus providing confidence in the modeling results. The results of this study are consistent with the cross-sectional field data of Wright and Kaplinski (2011) (see Figure 3.9).

The DES-3D model results can simulate the nonperiodic eddy pulsations at shorter timescales than found by Rubin and McDonald (1995). Nonperiodic eddy pulsations, especially pulsations in the strength and direction of the return current, could

be an important mechanism for exporting sediment out of the lateral recirculation zone. Rubin and McDonald (1995) concluded that eddy pulsations are caused by (1) external forces, such as, the water stage fluctuations produced from the Glen Canyon dam operation and (2) intrinsic behavior, such as, eddy vortices. Our DES-3D model does not include fluctuations in water level, but the nonperiodicity pattern produced by eddy vortex structures was well-captured as observed in Figure 3.11.

Lateral separation zones are known to efficiently trap sand when it is sufficiently supplied to a reach of the river from upstream. McDonald and Nelson (1996) hypothesized that turbulence structures having vertical vorticity are produced along the shear layer, advected downstream, and vertically sheared. These vertically sheared structures subsequently produce episodic inrushes of near-bed fluid and sediment to the lateral recirculation zone along the dividing streamline. Their hypothesis was also supported by laboratory flume measurements employing a simple expansion (McDonald and Nelson 1996). The DES-3D model also produces structures with vertical vorticity, but these structures rapidly transform into structures that do not have a preferred orientation of vorticity. Given the discrepancy between the model results reported here and the laboratory results and limited field results of McDonald and Nelson (1996), further field measurements addressing these structures are appropriate.

Future work should couple this DES-3D model with a sediment transport and morphodynamic model. Sedimentation patterns and bed evolution in complex channel morphologies with the presence of large-scale flow separation, secondary recirculation and free shear layers still remains a modeling challenge. Some available three and two-dimensional quasi-steady models also tested at EM and WT fan-eddy complexes have

over-predicted the sediment within the eddy zone. These quasi-steady models have performed poorly in simulating the process of exporting sediment from the eddy zone into the main channel, resulting in over-supply of sediment within the lateral recirculation zone, especially near the eye of the eddy (Sloff et al. 2009; Logan et al. 2010; Sloff et al. 2012). These studies suggest that mass failure may play a role in exporting sediment from the lateral separation eddy. Temporal variance of the strength and direction of the return current approaching the dividing streamline, produced in the current results, may also increase sediment export.

Turbulence-resolving models may do better at predicting channel change in complex channels. By coupling the hydrodynamic and the sediment transport model, the flow field velocity is assumed to be equal to the suspended sediment velocity. Therefore, based on the fluid behavior, it is possible to anticipate certain sediment transport patterns. For instance, it can be anticipated that the export of sediment from the eddy zone will occur at the convergence zone (observed in Figure 3.9) and sometimes at the reattachment zone (based on the nonperiodicity behavior). In contrast, the transfer of sediment from the main channel into the eddy zone will occur mainly along the divergence zone downstream of the eddy eye (see Figure 3.9). Short-term flow temporal variability indicates that the sediment input could be relatively constant in time while the export of sediment could be driven by pulsations since the model shows higher variability of directional distribution functions at the convergence zone and less variability at the reattachment zone. On the other hand, other complex behaviors of the sediment transport are difficult to anticipate directly from the DES-3D flow model. For instance, the effects of secondary flows and helicoidal flows in the sediment transport and bed changes are

more complex and it would be necessary to test the DES-3D sediment and morphodynamic model to infer some conclusions.

Overall, this first step done towards the understanding of sediment transport patterns and bed evolution is promising. The flow field demonstrated more accuracy than previous quasi-steady models due to the fact that LES avoids the parameterization of Reynolds stress tensors allowing the explicit representation of turbulent flow. This may lead to a better prediction of the sediment transport and channel changes.

SUMMARY AND CONCLUSIONS

This research study comprises the development, validation and result analysis of a three-dimensional, turbulence-resolving model at the scale of a river reach, using a Detached Eddy Simulation technique. The model has been tested in lateral separation zones featured by complex three-dimensional flow structures, flow separation, secondary flow, return currents and free shear layers. These lateral separation zones are located at two fan eddy complexes, named Eminence Break and Willie Taylor, along the Colorado River. The results are summarized in the following paragraphs:

A point-to-point verification was used to assess the ability of the model to reproduce ADCP flow measurements taken during the High Flow Experiment of 2008 in the Colorado River. The skill metrics used to evaluate the model show a good fit between the observed and simulated density functions. The four absolute error metrics are found to be: 0.4 m/s and 0.874 for the *RMSE* and correlation coefficient respectively, and 0.296 m/s and 0.04 m/s for the *MAE* and *MFE*. The two absolute metrics values are 16.25 % and 29 % for the *MdAPE* and *MAPE*. For the case of the direction of the velocity vectors, differences between simulated and observed values are equal or less than 19.3 degrees

averaging the entire validation data set within the computational domain. These skill scores indicate relatively small values of the forecasting errors and high correlation structures between spatial and probability density functions of observations and simulated data. These results demonstrate the good predictive capabilities of the DES-3D model.

Nonetheless, the validation is favorable but not ideal. Better assessment could be obtained with more field data, since the validation was based on only 4920 points of the 5.4 million cells simulated. The diagnosis (validation) suggests that the DES-3D model should introduce bed channel changes. The model was developed using a fixed computational domain at river bed and water level. Therefore, this condition introduces validation errors at the near-bed grid because most of the near-bed simulated velocities do not match the location of the observed near-bed velocities after erosion and deposition processes occur. River bed erosion decreases the river bed elevation leading to a stretch of the velocity profile that produces changes in the location of velocity magnitudes. Hence, the near-bed simulated velocities, usually close to zero in magnitude, sometimes are compared with non-near bed observed velocities which are higher in magnitude. Despite these facts, the DES-3D model results compare favorably with measured velocity based on six forecasting metrics employed to evaluate magnitude and direction of the velocity field.

In comparison with a two-dimensional model, the DES-3D model predicted a wider range of turbulent flow structures that more closely resembled structures observed in the field. The DES-3D model reproduces the size and position of the primary lateral recirculation flows, secondary lateral recirculation flows, and the strength of the return current. On the other hand, the two-dimensional turbulence-closure model captures a

strong recirculation zone characterized by one steady primary eddy cell, failing to predict the secondary recirculation zones and the strength of the return current. The steady primary eddy cell reproduced by the two-dimensional turbulence-closure model may be the cause of the oversupply of sediment in the eddy zone predicted with similar and quasi-steady models mentioned in the introduction and discussion sections.

Three-dimensional flow structures were simulated using the DES-3D model. Large vorticity structures produced at the free shear layer become three-dimensional with no preferred orientation further downstream. Significant differences are found between near-bed and surface velocity vector directions which generate an Ekman inward spiral at the primary eddy at both sites along the vertical axis centered in the eddy eye. Finally, the model was able to capture eddy pulsations due to eddy vortex structures. These pulsations occurring mainly between the return current and the main channel are expected to be an important mechanism of sediment export from the lateral separation eddy.

Overall, the flow structures captured with the DES-3D model are consistent with field observations reported in the study of Wright and Kaplinski (2011). The predictive capability of this model elucidates the possibility to apply it as a tool to further test future controlled flood releases and operating scenarios from Glen Canyon Dam.

In summary, this research provides a framework that incorporates turbulence-resolving models to the study of complex river configurations. Computational Dynamic Models based on LES and DES techniques are significantly more accurate than two and three-dimensional quasi-steady models. Nevertheless, LES/DES techniques are substantially more computational expensive requiring parallelization with the use of multiple processors of a supercomputer. In cases such as the lateral recirculation zones,

observed in the Colorado River, computational expenses of turbulence-resolving model are required and justifiable since other two and three-dimensional quasi-steady models have proven difficulties in predicting flow, sediment transport and channel changes in this complex system. Finally, this research is fundamental because the same methodology and principles apply to other types of river configurations. Lateral separation zones are a subaqueous phenomenon manifested in any abrupt change in river channel width and depth. Sharp meanders, channel constrictions, many engineering structures, vegetation, and certain types of bedforms (e.g., dunes and ripples) cause large scale flow separation, primary, secondary eddy cells and return currents.

CHAPTER 4

CONCENTRATION OF SUSPENDED SEDIMENT IN LATERAL SEPARATION ZONES: FIELD SCALE DETACHED EDDY SIMULATION MODEL.

INTRODUCTION AND BACKGROUND

Computational modeling constitutes a fundamental tool for the prediction of turbulence, sediment transport and geomorphologic changes in river systems. Fluvial models have significantly advanced over the last five decades. A number of two- and three-dimensional models are currently available to estimate turbulence and sediment transport. Depth-averaged, two dimensional models typically rely on simple closures relating boundary stress to roughness and depth-averaged velocity (Lane et al. 1999). Two-and three-dimensional steady and quasi-steady fluvial models operate by using time-averaged or ensemble time-averaged derivatives at scales greater than an integral-time scale. The studies of Sinha et al. (1998) and Nikora et al. (2007) exemplify these steady and quasi-steady models. In relatively simple channels these models have predictive capability. However, their predictive skill can be low in the presence of river settings with strong curvatures featured by flow separation, secondary flows and free shear layers, where a direct solution of the turbulent flow field plays an important role in the accuracy of flow and sediment transport prediction (Keylock et al. 2012; Chang et al. 2013).

Turbulence-resolving models can predict with better fidelity the turbulence and sediment transport processes in complex channel settings, resolving the time-dependent eddy structures larger than the grid scale, while the sub-grid-scale (SGS) turbulence is modeled (Zedler and Street 2001; Tseng and Ferziger 2004; Keylock et al., 2005; Kirkil

et al. 2009; Keylock et al. 2012). As computational capabilities advances, parallelized, turbulence-resolving models can now be developed and applied to convoluted fluvial morphodynamic problems.

In this research, a parallelized, three-dimensional turbulence-resolving model is coupled with a continuum sediment transport model developed and tested in lateral separation zones. The DES decomposition of the DES-3D sediment model follows the same procedure of the DES-3D flow model (see Chapter 3), where variable fields greater than the grid scale are fully resolved and the sub-grid-scale (SGS) variables are modeled using the rough wall extension of the Spalart-Allmaras model. The model resolves large-scale turbulence using DES and, simultaneously, integrates the sediment advection-diffusion equation, wherein advection is provided by the DES velocity field minus the particles settling velocity, and diffusion is provided by the SGS or RANS eddy viscosity. (Ferziger 1976; Tseng and Ferziger 2004; Squires 2004; Spalart et al. 2006; Spalart 2009; Shur et al. 2011a).

This work is a follow-up of Chapter 3 that presents a development and validation of a DES-3D flow model to study lateral separation zones in the Colorado River in Grand Canyon along two eddy fan complexes named Eminence Break (EM) and Willie Taylor (WT). Results of the DES-3D flow model shows predictive capabilities based on error analysis between field observations and numerical simulations (see Chapter 3).

This chapter implements the results and numerical domain of the DES-3D flow model to couple a sediment transport model, to estimate the sediment fluxes, concentration patterns and grain size distribution in the eddy zones. The structure of this chapter is summarized as follows. The model description section presents the numerical

methodology that encompasses the grid and spatial discretization, simulation time, governing equations and boundary and initial conditions. Analysis and results investigates the concentration patterns, deposition fluxes and grain size distribution for a base case scenario. Synthetic and future scenarios are also included in this analysis. Finally, discussion, future work and conclusions are provided in final sections.

MODEL DESCRIPTION

Grid and Spatial Discretization

The numerical domain is the same as the domain developed for the DES-3D flow model described in Chapter 3. This domain was discretized as a structure grid of cells. The grid was generated as a structured block of hexagonal cells using a code developed within OpenFOAM environment. The algorithm generates the grid domain using a triangulated surface extracted from a digital elevation model of the river reach. A two-dimensional depth-averaged model also developed within OpenFOAM was used to generate the water surface elevation of the computational domain.

The final grid consists of 5,625,000 hexahedral cells. In the vertical direction, the near-bed grid cells were imposed to be equal to five centimeters to avoid non-orthogonal faces at the bed. Above the first near-bed grid cell, a vertical hyperbolic tangent-stretching function was employed to distribute the vertical cell space assigning smaller space to near-bed cells. This hyperbolic function aims to maximize the accuracy at simulating the smallest eddies protruding from the river bed. The span-wise and stream-wise spacing was equal or less than one meter approximately.

The grid domain was decomposed into 150 sub-domains, and each sub-domain was assigned to its own computational processor. Open MPI provided communication between computational processors. The simulations were conducted at the Advanced Computing Center in Arizona State University (A2C2 – Saguaro supercomputer).

Simulation Time

The DES-3D flow model statistics are computed using 1000 seconds of simulated time, while the DES-3D sediment model uses 10000 seconds (equal to 2 hours and 45 minutes). Thus, the sediment model is 10 times more computationally-expensive than the DES-3D flow model because it requires significantly more simulation time to achieve convergence. The model convergence is measured based on the stability of grain size distribution (see grain size distribution section). The spin-up phase is 15 minutes and the net model time is 2 hours and 30 minutes. Therefore, 30 times of flow at the reach-averaged velocity through the numerical domain, inlet to outlet, was required for model convergence. 6 days of processing time on the A2C2 supercomputer were required to simulate these 2 hours and 45 minutes.

Governing Equations

The DES-3D flow model is coupled to a continuum formulation of the sediment continuity equation. The flux form of the Smith and McLean suspended sediment boundary condition is used to estimate the erosion and deposition rates (see next section on Boundary Conditions). The DES decomposition of the sediment model follows the same procedure of the flow model (see Chapter 3), where variable fields greater than the grid scale are fully-resolved and represented with an over line and SGS variables are represented by a double prime, in Equations 4.1 to 4.3.

The governing equations are illustrated below in terms of the DES decomposition:

Continuity $\frac{\partial \bar{u}_i}{\partial x_i} = 0$ (4.1)

Momentum $\frac{\partial \bar{u}_i}{\partial t} + \frac{\partial}{\partial x_j}\left(\overline{u_i u_j}\right) = -\frac{1}{\rho}\frac{\partial \bar{p}}{\partial x_i} + \frac{\partial}{\partial x_j}\left((\nu' + \nu'_t)\frac{\partial \bar{u}_i}{\partial x_j}\right)$ (4.2)

Advection Diffusion $\frac{\partial \bar{c}}{\partial t} + \frac{\partial}{\partial x_j}\left((\vec{u} - \vec{w}_s)\bar{c} - \vec{w}_s c_a - (\nu' + \nu'_t)\frac{\partial \bar{c}}{\partial x_j}\right) = 0$ (4.3)

The variables and parameters of Equations (4.1) and (4.2) are the filtered velocity and pressure components, $\bar{u}_i$ and $\bar{p}$, and the density of the water , ρ. The molecular viscosity and eddy viscosity $(\nu' + \nu'_t)$ represent the unresolved flow sub-grid (SGS) stress tensor, modeled using the Spallart Allmaras (S-A) turbulence closure.

The variables of Equation (4.3) are the filtered sediment concentration field $\bar{c}$, and the filtered sediment velocity equal to the DES velocity minus the settling velocity $(\vec{u} - \vec{w}_s)$. The SGS scalar flux term is equal to the molecular viscosity and eddy viscosity $(\nu' + \nu'_t)$, which are computed through the rough wall extension of the Spalart-Allmaras model turbulence closure model, in the same fashion that the SGS model is handled in the equations of fluid motion (Equation 4.2).

Pressure Implicit Splitting of Operators (PISO scheme) for unsteady models was employed as the numerical method scheme. PISO is a pressure correction scheme used to calculate the pressure distribution correction to drive the local velocity field towards a result that satisfies both momentum and continuity. The solution progresses in time such that the Courant number is kept well below 1 in the domain. This allowed a better time-accurate resolution of the non-filtered scales (Ferziger and Peric 2002).

The DES-3D flow solver is a computational module included in the OpenFOAM solvers. The DES-3D sediment model is programed and compiled as an OpenFOAM solver for the purpose of this study. The computational code is attached in Appendix E.

Boundary Conditions

The simplest boundary condition occurs at the water surface since the flux of sediment normal to the water surface is zero; hence $\overline{F}_{sz}\,|_{z=H} = 0$, where F represents the net normal flux of sediment. Nonetheless, the complexity comes at the bed boundary condition because the normal flux of sediment shall account for the entrainment and deposition rates at the bed. A simple equation to describe the boundary condition of the net normal flux of sediment at the bed is:

$$\overline{F}_{sz}\,|_{z=b} = w_s c - w_s c_a \tag{4.4}$$

Where $w_s c$ is the deposition rate, and the concentration field, c, is directly calculated from the advection-diffusion Equation (4.3).

The entrainment sediment rate is estimated using the empirical equation of Smith-McLean (1977) (Equation 4.5):

$$w_{si} c_{ai} = \frac{c_{b_i} \gamma \left(\frac{\tau_{b_i}}{\tau_{c_i}} \right)}{\left[\gamma \left(\frac{\tau_{bi}}{\tau_{ci}} - 1 \right) \right]} \tag{4.5}$$

Where subscript, i, denotes the group of sediment grain size (see grain size distribution section), c_a is the equilibrium concentration of sediment in the cells at the bed. The entrainment flux is then the equilibrium concentration times the particle settling

velocity, $w_s c_a$. c_b is the sediment concentration of the bed equal to 0.65 (one minus the porosity); τ_b and τ_c are the boundary and critical shear stresses, respectively (Smith and McLean 1977) and γ is an empirical parameter, in this case equals to 1.3×10^{-4} (Hill et al. 1988). The value of the empirical parameter γ was selected based on measurements obtained from an experimental study in a large recirculating flume (Hill et al. 1988).

A wide range of values of this empirical parameter γ, have been estimated from field observations, differing from one up to three orders of magnitude. Some examples are found to be 1.95×10^{-3} (McLean. 1976), 2.4×10^{-3} (Smith and McLean 1977), 1.6×10^{-5} (Wilberg and Smith 1983), 1.5×10^{-2} (Kackel and Smith 1986), 2.0×10^{-5} to 5.0×10^{-4} (Drake and Cacchione 1988).

The empirical parameter γ, equals to 1.3×10^{-4} was selected for this model because it was calculated in a laboratory setup (Hill et al. 1988). Nevertheless, an explanation for employing this parameter must be justified by using model calibration to find a specific value that leads to better modeling results of the simulated entrainment sediment rate.

Initial Conditions

Depth integrated concentrations of suspended sediment collected at one location in the main channel downstream of EM are used as input values to the model. Rouse profiles matching the depth integrated concentrations, collected during the peak of the controlled flood of 2008 (Wright and Kaplinski 2011) were imposed at the inlet. The concentration resulting from averaged rouse profiles was set as constant value at the inlet of the domain. Downstream of the inlet, the concentration adjusts to an accurate vertical

profile driven by the flow velocity field since these two fields are coupled in this DES-3D sediment model.

The initial condition for the flow is the same as the initial condition of the DES-3D flow in Chapter 3 (Alvarez et al. submitted). The inlet flow discharge of the model was set to match the peak controlled flood of 2008, equal to 1200 m3/s (~42,000 cfs).

Grain Size Distribution

The range of sediment grain sizes is an important aspect to be considered in the sediment transport model since sediment velocity, and erosion and deposition patterns are highly dependent on the grain size distribution. Five groups of sediment sizes are employed in the DES-3D sediment model, which requires five coupled-solutions of the advection-diffusion equation (Equation 4.3).

In the case of one group of sediment grain size, the value of concentration at the bed minus the pore space is equal to $c_b = 1 - \lambda = 0.65$; where λ is the porosity of the non-moving bed. For the case of a sediment grain distribution, the concentration at the bed is the sum of each grain size group such that $c_{b_i} = (1-\lambda) f_i$, where f_i corresponds to each group fraction.

The distribution of the sediment grain size groups are estimated using a mixing layer model. The mixing layer model, based on the mass continuity equation, estimates the fraction of each group within a control volume equal to one meter, redistributing the grain sizes every time step. $c_{b\,i}$ is calculated as the deposition of sediment, into the mixing layer minus the erosion of sediment from the bed. At each time step, $c_{b_i} = (1-\lambda) f_i$, where the suffix *i* denotes the grain size group, and f_i is the fraction of

the grain size for group *i*. In this manner, the mixing layer fractions are computed after each time step as part of the DES-3D sediment model (solver details are shown in Appendix E). The details of sediment grain diameters and settling velocities are presented in Table 4.1.

The Limitations of Initial and Boundary Conditions

The shortcomings of the initial and boundary conditions are presented in this subsection. The imposed fixed numerical domain, the boundary condition of sediment supply and the initial condition of grain size distribution are limitations that decrease the predictive capabilities of the model. This subsection aims to explain these model limitations and the linkages with the simulated results. It also provides a possible methodology for modeling improvements.

Fixed numerical domain

The numerical domain is immobile during the time of simulation. This imposed boundary condition does not incorporate river channel changes due to erosion and depositional processes. A fixed numerical domain introduces errors to the simulation as the turbulent flow profile and sediment velocity are highly correlated with river topography and shear stress values significantly increase or decrease depending on riverbed roughness. Thus, predictive capabilities of the model may be affected by the fixed boundary condition.

A suggested methodology for redefinition of the numerical domain would consist on adjusting the riverbed to account for deposition fluxes. However, bed evolution can become a difficult process in structured grid cells since the mesh has to fulfill the grid topology requirements to guarantee orthogonality between grid cells. A DES-3D

sediment model and river channel change formulation has been tested in the simulated river transect. The simulations did not reach convergence; further tests need to be performed to reach cell orthogonality in the grid topology required at every time step of the simulation.

The Boundary Condition of the Sediment Supply

The boundary conditions at the bed do not impose any threshold for sediment supply. In other words, this boundary condition allows entrainment and deposition at the bed with unlimited sediment supply. Field observations show a limited supply of sediment from the bed in the rapids and considerably more supply of sediment from the bed in the main channel and the lateral separation zones (Wright and Kaplinski 2011). The field boundary conditions considerable differ from the model in the threshold of sediment supply, which leads to low model predictions of net sediment erosion and deposition. Improvements on the boundary conditions of bed sediment supply must be done to enhance the model predictive capabilities of simulating net deposition at the bed. Further modeling simulations have to be performed imposing a realistic threshold in the boundary condition of the sediment supply. The current model has the capability to initialize the boundary condition for the bedrock topography to limit the sediment supply. Field data is required to impose this boundary condition because it is unlikely to find data of bed topography. However, some approximated values could be imposed based on the final results, or post-flood conditions of river morphology reported in the study of Wright and Kaplinski (2011). This methodology needs to be combined with accurate initial conditions of the spatial distribution of sediment grain sizes.

The Initial Condition of the Grain Size Distribution

The initial conditions of the grain size distribution are imposed at the bed with identical size distribution through the simulated river transects (see table 4.1). The simulated grain sizes range from 0.088 mm to 0.3 mm corresponding to fine sand to medium sand. This distribution is a very rough simplification of the systematic grain size distribution observed in fan-eddy complexes in Grand Canyon. The pattern of grain size and sediment supply suggests that coarsest type of soil diameters (e.g gravel, pebbles, cobbles and boulders) located in the rapids, are not likely to move compared with fine grain sizes (e.g sand and gravel) found in the main channel and lateral separation zones (Mueller et al. 2014; Topping et al. 2000a; Topping et al. 2000b; Topping et al. 2005). The limitation of employing uniform grain size distribution is exemplified in the model results of net deposition patterns and grain size evolution along the river-reach transect (see section of erosion and deposition patterns and size distribution). Sand soil is observed to be depleted along the rapids causing an over estimation of erosion fluxes. In turn, eroded sediment coming from the rapids is transported downstream resulting in over supply of sediment to the main channel and lateral separation zones. Further research must address different grain size diameters, wider spectrum of grain size and a spatially distributed grain size diameters based on field observations and studies of grain size sediment patterns in Grand Canyon. The benefit of this grain size distribution model is the flexibility to input different grain size groups. However, sediment grain sizes spatially distributed along the river-reach transect have to be coded and embedded within the DES-3D model.

ANALYSIS AND RESULTS

The objective of this section is to assess the capabilities of the DES-3D sediment model to predict erosion and deposition patterns during the simulated time of 10000 seconds. Results aim to understand the linkages of sediment transport and concentration patterns between lateral separation zones, main channel and channel constrictions. The ultimate goal is to infer the processes of exporting and importing sediment in the lateral separation zones, important to predict the supply of sediment within the primary eddy.

Table 4.1. Grain size distribution parameters.

Mean Diameter (mm) (*)	**Percent of grain size distribution (%) (a)**	**Settling Velocity (m/s) (b)**	**Critical shear stress (m^2/s^2) (**)**
0.088	15	0.0051	0.00011
0.12	25	0.0086	0.00013
0.16	25	0.0135	0.00015
0.2	25	0.0189	0.00016
0.3	10	0.0336	0.00020

(*) The mean diameter and grain size distribution were obtained from a depth-averaged concentration sample taken during 2008 controlled flood in one point downstream EM (the data are unpublished and provided by Scott Wright and Matt Kaplinski from U.S. Geological Survey, Sacramento, California and Northern Arizona University, Flagstaff, Arizona).
(**) The settling velocity and critical shear stress are estimated using the USGS Sediment-Transport Applet: Particle settling velocity and critical shear stress (compiled by Chris Sherwood, 2014).

Modeling results are organized in five subsections describing the following processes: (1) Concentration patterns at the bed; (2) Erosion and deposition patterns; (3) Spatial average deposition fluxes; (4) Sediment grain size distribution; and (5) Synthetic scenarios.

Concentration Patterns at the Bed

High correlations of concentration values at the bed and velocity patterns are observed when comparing Figure 4.1 and Figure 3.5 of Chapter 3. In canyon rivers,

channel constrictions exerted by tributary debris fans lead to streamlines convergence in the rapids and streamlines divergence of flow along the pools in the main channel (Figure 3.5, Chapter 3). The results show that concentration increases in constrictions and rapidly decreases downstream in the pools (Figure 4.1), which evidence a dominant pattern of the advection over the diffusion operator (Equation 4.3). Therefore, concentration patterns are observed to be correlated with the velocity of the fluid (Figure 4.1 and equation 4.3). Concentration values at the main channel range between 0.0025 and 0.018, while the values at the rapids are equal or higher than 0.025 (Figure 4.1).

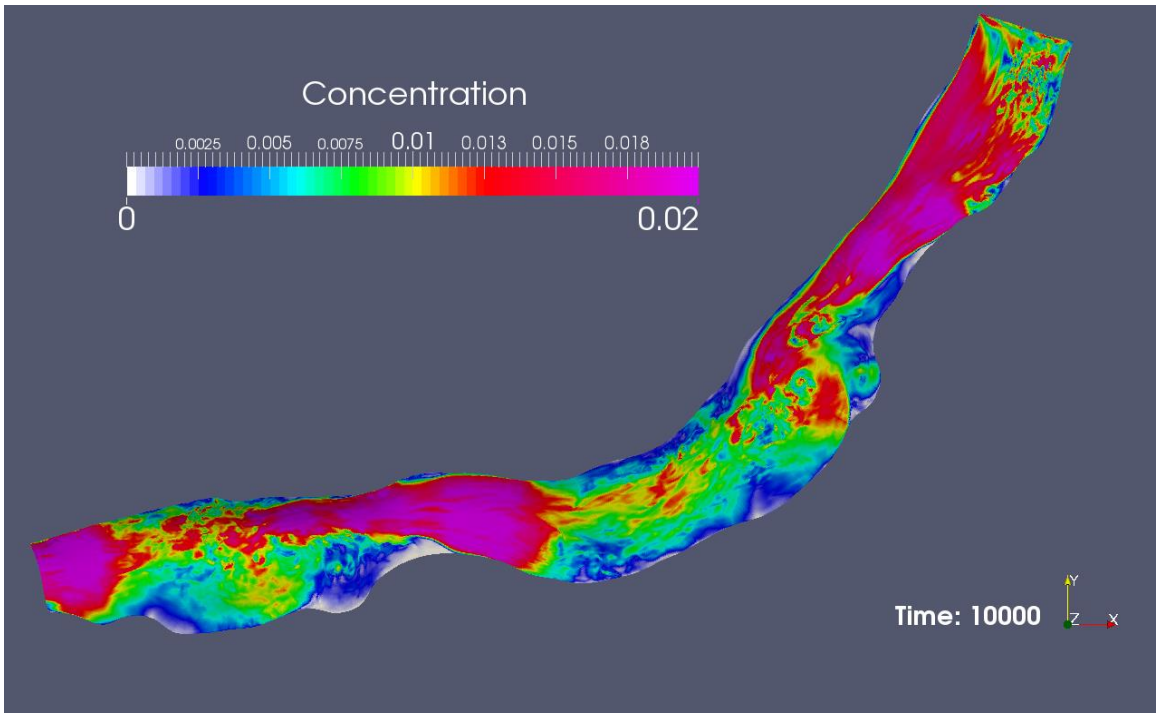

Figure 4.1. Concentration of sediment at the bed along the simulated transects. Concentration values are unit less (volume/volume).

The model spin up phase is equal to 1000 seconds (see model overview section). After the spin-up phase, a strong pattern of unsteady pulsations of concentration is observed at the exchange of concentration between the primary eddy zone and the main channel. These pulsations occur at the reattachment zone and at the convergence zone

formed in the interception between the outlet of the return current and the main channel. The secondary eddy also shows a pattern of unsteady pulsations in the export and import processes from and to the primary eddy (Videos 4.1.a and 4.1.b, Appendix F).

The highest concentration values are found in the return current, close to the eddy eye. These values oscillate between 0.012 up to 0.015 in time. A decrease of concentration is presented in the reattachment zone, with values fluctuating from 0.004 to near-zero values (Videos 4.1.a and 4.1.b, Appendix F).

Differences in concentration and fluid velocity patterns between the secondary eddies at EM and WT are observed (see Videos 4.1.a and 4.1.b) and found to be correlated with the differences in the morphology of these fan-eddy complexes. EM is featured by a smaller secondary eddy with significantly higher concentration values in this secondary eddy when compared with WT (see Videos 4.1.a and 4.1.b).

Erosion and Deposition Patterns

The purpose of this section is to describe and analyze the patterns of deposition in the eddy zone and to understand the sediment transfer from the lateral separation zone to the main channel and vice versa.

Deposition flux is the resultant of the subtraction between normal deposition and entrainment rates to and from the bed, multiplied by the surface area of the bed, as stated by the Gauss theorem. The net deposition is estimated by adding the deposition fluxes at every time step (see Figure 4.2). Negative net deposition values mean net erosion from the bed, while positive values mean net deposition at the bed. Net erosion is displayed in the color scheme from yellow to blue, while net deposition flux uses yellow to red

(Figure 4.2). The same color schemes of Figure 4.2 are applied to Video 4.2 (Appendix F).

The predictive-capability of the DES-3D sediment model is assessed by the accurate estimation of the processes of import and export of sediment at the lateral separation zones at both sites. Export of sediment from the primary eddy zone to the main channel is observed following a pattern of high frequency pulsations of positive deposition flux values. This export of sediment from the eddy zone occurs at the convergence zone between the primary eddy cell and the main downstream channel flow (Video 4.2). The import of sediment into the eddy zone occurs mainly at the reattachment zone, downstream of the primary eddy. In comparison with the export of sediment from the eddy zone, the import of positive deposition flux from the main channel occurs at lower frequency pulsations (Video 4.2).

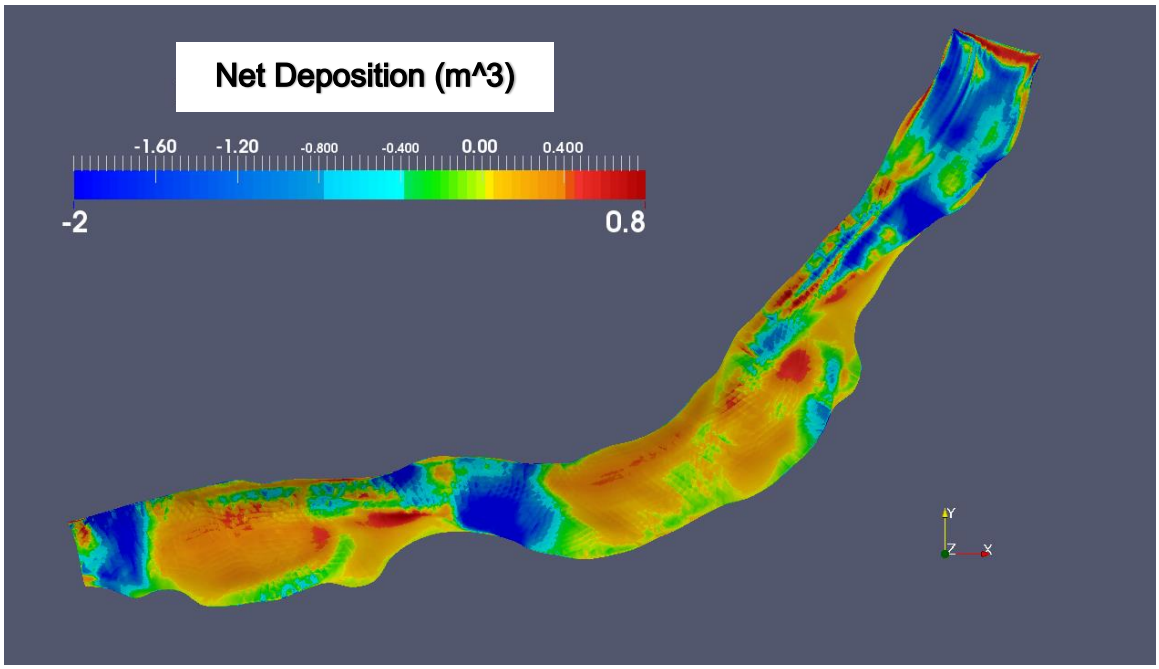

Figure 4.2. Net deposition at the bed after 10^4 seconds of simulation. Net erosion (negative sign) is displayed using the color palette yellow to blue. Net deposition (positive sign) is displayed using the color palette yellow to red.

Net negative deposition is observed at the inlet of both rapids due to the high shear stress present in the convergence of streamlines in the rapids. This negative deposition is more accentuated in WT (Figure 4.2). The sediment eroded from the rapids is transported to the main channel and to the lateral separation zones. This transfer of sediment occurs in low frequency pulsations (Video 4.2).

Positive net deposition is observed at the separation and reattachment zones, showing relatively constant values during the entire simulation (Figure 4.2 and Video 4.2). This prevalence of positive net deposition in the separation and reattachment zones plays a fundamental role in the replenishment of eddy bars, as these zones are the principal storage of fine sediment deposits. The deposition in the reattachment zone is significantly larger as compared with the deposition in the separation zone (Video 4.2 and Figure 4.2), as a result, the reattachment bar is larger than the separation bar. These sandbar size differences are shown in Figure 3.3.

Spatially Averaged Deposition Fluxes

The lateral separation zones of EM and WT are selected from the domain shown in Figure 4.3(a). The deposition fluxes of every discrete cell at the bed are averaged within the selected domain (EM and WT) at each time step of the simulation. Mean and standard deviation are plotted with the objective of visualizing the deposition flux spatial distribution in Figure 4.3(b).

At EM, a spatial balance between erosion and deposition flux values is shown through the fluctuations of the spatial mean about a zero value. A near-zero value of the spatial mean may not be interpreted as a temporal process of non-erosion or deposition in

the lateral separation zone. Contrarily, the standard deviation envelop indicates a wide range of temporal and spatial variability of the distribution of deposition flux values.

At WT, the spatial averaged distribution behaves similarly to EM, except for the higher mean spatial values. A positive mean value means that averaged deposition fluxes are higher than averaged erosion fluxes, at each cell. Nonetheless, these results do not imply a uniform pattern of deposition in the WT eddy zone. The wide standard deviation envelop proves a high dispersion in the distribution of deposition flux values showing high spatial variation at each time step (Figure 4.4).

In summary, this subsection illustrates the highly variable spatial distribution of deposition fluxes in both lateral separation zones during this simulation period.

Grain Size Distribution

An assessment of the grain size distribution at the bed is shown in this section. Such an evaluation is carried out by using: (a) the information provided in Table 4.1, (b) the analysis derived from the output visualization (see Figure 4.5), and (c) the boxplots derived of each grain size group for both fan eddy complexes (see Figure 4.6).

The grain size distribution solver is a novel tool developed in this DES-3D sediment model as it allows the discretization of all the variables by group size (see Table 4.1 for grain distribution properties). The default condition makes the sum of the total percentage accumulated from the grain size distribution, at each time step, equal to 100% (see Appendix E for the code details).

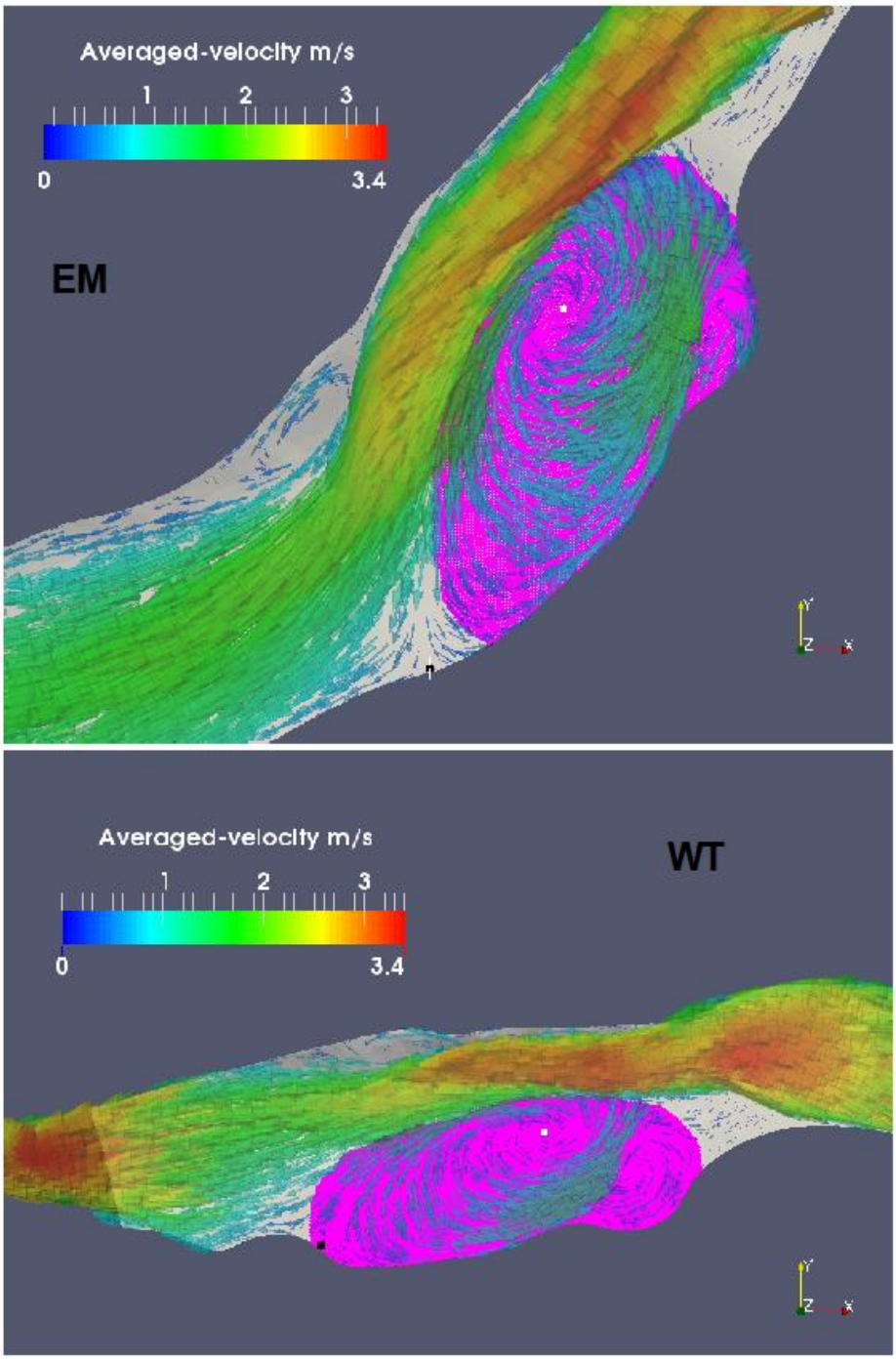

Figure 4.3. Selected domains of (a) EM and (b) WT. Lateral separation zones, shown in dark pink are used to estimate spatial averaged rates of erosion and deposition. The lateral separation zone was selected based on the results from time -and depth-averaged DES-3D flow model shown in Figure 3.8(a) and 3.8(b) in Chapter 3.

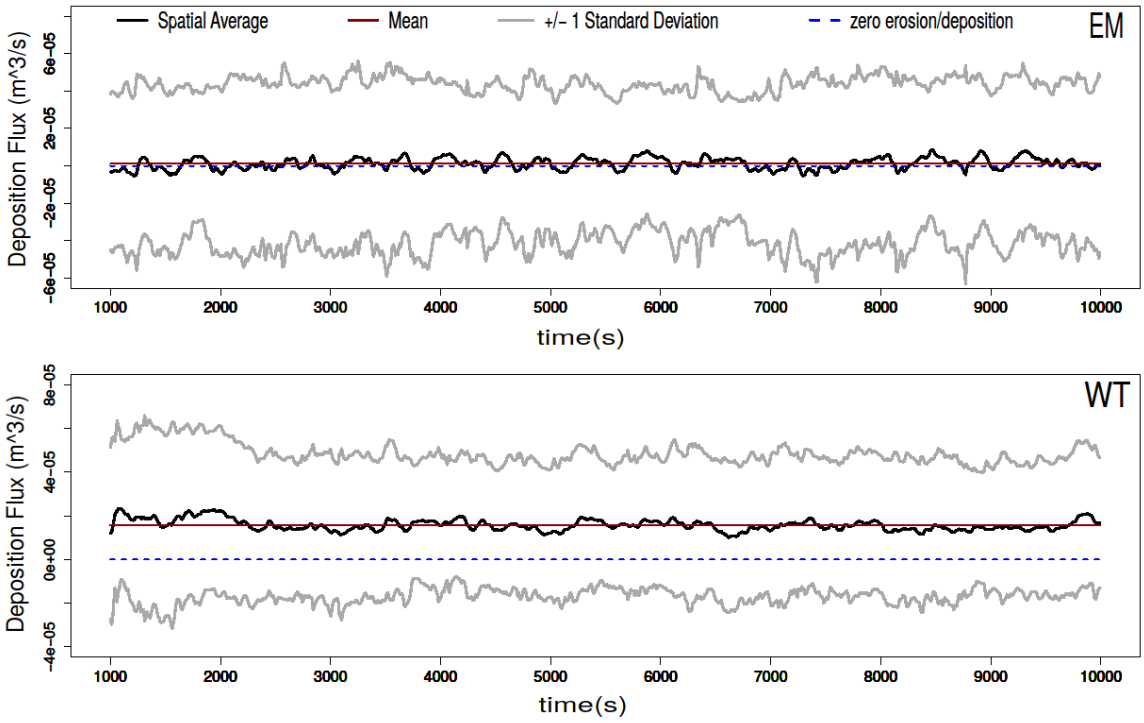

Figure 4.4. Spatial averaged deposition fluxes at the lateral separation zones in (a) EM and (b) WT. Line colors represent averaged values in red, mean-averaged value in dark red, zero erosion or deposition in dashed-blue and one standard deviation in grey. Statistics are estimated from the selected domains shown in Figure 4.3.

The comparison between grain sizes is organized by percentages and the range of values in which each particle rearranges after the 10000 seconds simulation. This analysis is based on the last time step of simulation as at the end of the simulation the bed grain size distributions are relatively stable. The grain size distribution imposed initially is explained in detailed in Table 4.1. Mean diameters for group 1 to 5 were distributed as (15, 25, 25, 25 and, 10 percent). These initial conditions are a rough approximation of the concentration sample taken 0.6 meters above the bed during the 2008 controlled flood in one point downstream of EM. However, no other data are available for the purpose of assessing this model module.

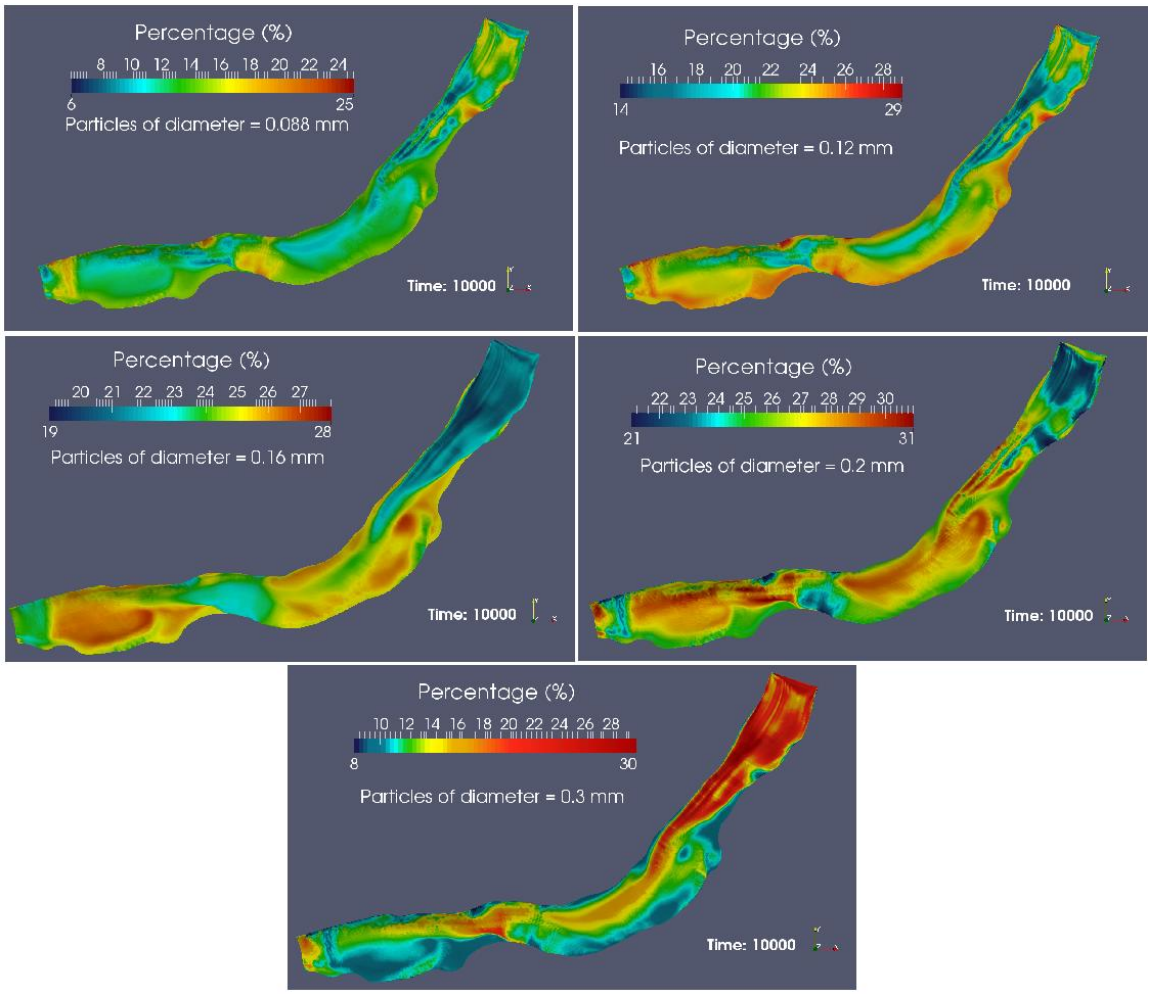

Figure 4.5. Grain size distribution of each group of sediment particles at the bed, after 10000 seconds of simulated time along the river-reach transect. Note: each sediment particle group has its own color-scale palette as a function of its own range of values.

The finest diameter, group 1, decreases downstream along the river reach compared with the initial condition (Figure 4.5). The group 1 grain size diameter of 0.088 mm is classified as very fine sand or sand silt. The model predicts depletion of very fine sand throughout the river reach at the modeled high discharge of 1189 m^3/s.

The percentage of sediment of group 1 increases up to 25% in the left side of the WT rapid, as illustrated in Figure 4.5. This sediment grain size value of 25% detected in the WT rapid is considered an outlier as observed from the probability density function in

the lateral separation zone (Figure 4.6). This outlier value can be an artifact of the imposed boundary conditions. The lack of bedrock topography, unlimited sediment supply and fine grain size distribution lead to this anomaly on the observed fraction of group 1 at the right side of the WT rapid.

Grain size groups 2,3, and 4 (0.12, 0.16, and 0.2mm) are classified as fine sand and show more spatial variability in grain size percentage than groups 1 and 5. All of these grain sizes are eroded at the inlet transect and the rapids, and transported to the lateral separation zone. Deposition occurs mainly in the primary zone and separation and reattachment zones (Figure 4.5).

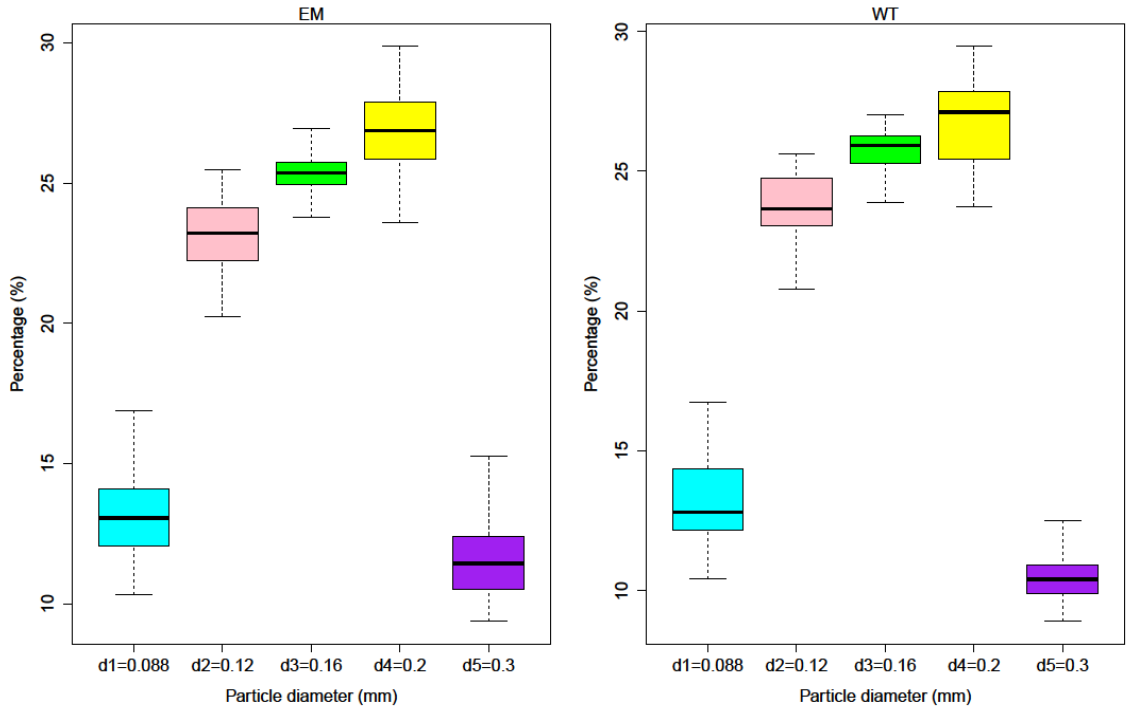

Figure 4.6. Boxplots of grain size distribution in lateral separation zones at EM and WT. Eddy zones data are selected from Figure 4.3. Boxplots illustrate mean, quartiles and fences. Outliers have been excluded for visualization purposes.

Several differences between the group 2, 3 and 4 are observed. Group 2 – 0.12mm, started as 25%. This group contributed to the replenishment of the reattachment

and separation zones in a range of 24% to 26%. The reattachment and separation zones are important because of the eddy bars are formed in these zones (Figure 4.5, Chapter 3-Figure3.1). The contribution of this group to the lateral separation varies between 21% and 26% based on the boxplot shown in Figure 4.6. Additionally, the percentage of group 2 in the rapids and in the left thalweg varies between 18% and 29%. These results must be an artifact, similar to the pattern observed in group 1.

Group 3 and Group 4 with grain size particles of 0.16 mm and 0.2 mm illustrate a strong pattern of permanency in the eddy bars with 26% to 31% (Figure 4.5). The highest fraction is found at the primary eddy bar with 28% to 31% of group 3 and group 4 respectively. The percentage of distribution of group 3 at the separation and reattachment bars ranges between 26% and 28%, while group 4 ranges between 25% and 27%. The distributed values of group 3 have little dispersion ranging between 24% and 26% in the lateral separation zones (Figure 4.6). On the other hand, the standard deviation of group 4 is higher compared with group 3 and the percentages of values in the density function are higher compared with the initial condition. Accordingly, particle diameter equal to 0.2 mm corresponding to group 4 provides the major percentage of values to the lateral separation zones. In the rapids, these two groups have the propensity to erode showing values ranging between 21% and 24% (Figure 4.5).

Finally, group 5 (0.3mm) corresponds to a medium sand and it arranges along the river-reach transect mainly at the inlet, rapids and main channel. The grain size distribution started as 10% and the distribution increases at the inlet transect, main channel and rapids with percentages varying from 16% to 30% (Figure 4.5). On the other hand, the contribution to the lateral separation zone is very slight with fractions ranging

between 8% and 10% (Figure 4.5 and Figure 4.6). This pattern may be caused due to the high shear stress values required to transport this type of soil in suspension compared to finer particle size groups. Thus, medium sand remains mostly at the bed (Figure 4.5 and Figure 4.6).

Concluding, the general pattern of grain size distribution along the river-reach transect can be summarized as follows: (1) sand silt soil decreases downstream compared to the initial condition showing a pattern of depletion throughout the simulated river-reach, (2) fine sand soil present the most changes in the grain size distribution during the simulated time and the groups 3 and 4 (particles 0.16 mm and 0.2 mm) have the most contribution to the lateral separation zones, and (3) medium sand is not likely to move along the river-reach transect.

Synthetic Scenarios

The aim of this section is to test the DES-3D sediment model responses to two synthetic cases other than the base scenario. The base scenario reproduces, as realistic as possible, the initial and boundary conditions of the field (see section of Model Description). On the other hand, synthetic scenarios are not based on field data, but aim to analyze hypothetical or future conditions. The overall goal is to research the response of the lateral separation zone to different concentration fluxes at the inlet.

The simulated outputs consist of two scenarios each of 2 hours and 45 minutes of duration. Scenarios 1 and 2 correspond to 50% and 200% of the initial concentration value (Figure 4.7 – cross-section transects) respectively.

Concentration fluxes were estimated along six river cross sections, at every 1000 seconds (Figure 4.7), starting near the inlet and moving towards upstream of the EM

rapid (Figure 4.8). Results show that concentration fluxes become relatively similar along the transition from transect T1 to T6. Thus, the dependence of concentration fluxes of erosion at the bed, rather than the imposed initial conditions along the river-reach transect upstream the rapids, is clearly observed in the cross sections shown in Figure 4.7.

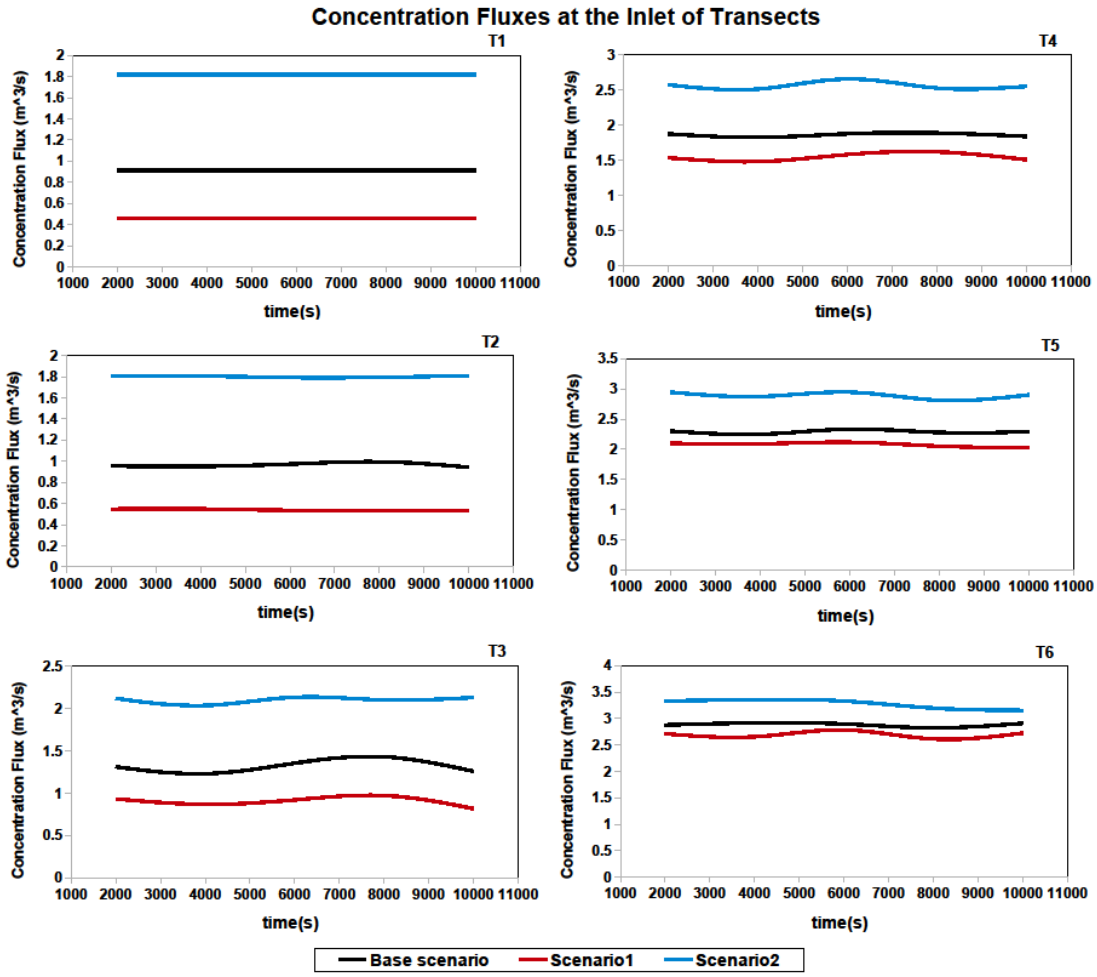

Figure 4.7. Patterns of concentration fluxes at the six cross-section transects (T). The locations of the transects are shown in Figure 4.8. Plots are set using data outputs every 1000 seconds. The black line denotes the base scenario, red line, scenario 1 and blue line, scenario 2.

The concentration fluxes at the inlet of the lateral separation zones also reveal a similar pattern. Despite the distinct initial conditions, the concentration values in the EM and WT rapids are relatively similar and independent of the initial condition imposed at the domain inlet of the river-reach transect (Figure 4.9). In other words, the unlimited supply of sediment from the bed is controlling the sediment transport at the river transect along the boundary inlet to the input of the lateral separation zones.

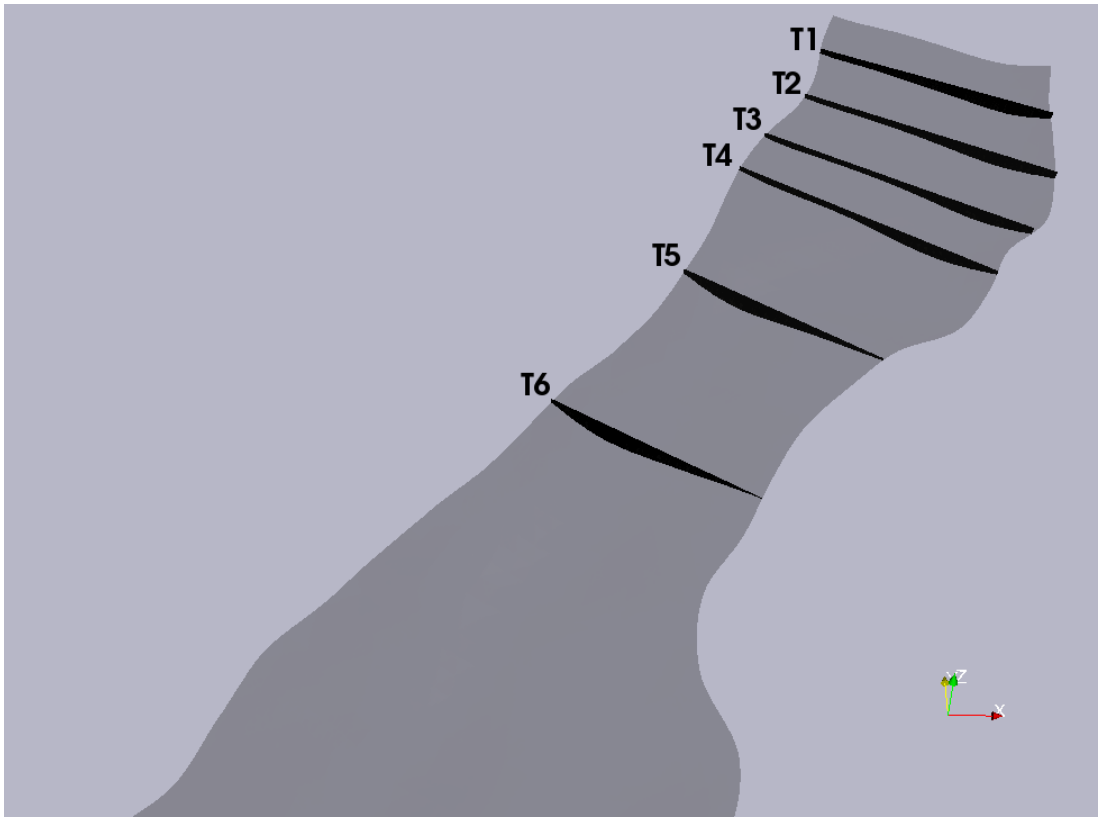

Figure 4.8. River cross-sections employed to compare concentration fluxes between the base case scenario and the two synthetic scenarios from the inlet of the simulated river-reach to the rapid of EM.

Simulation of lateral separation zones using synthetic scenarios is possible only if the concentration flux values are preserved at the inlet of the eddy zone. Preservation of concentration fluxes at the inlet of the lateral separation zones was not feasible to reach

from these synthetic scenarios due to the unlimited supply of sediment from the bed and the inaccurate imposition of sediment grain sizes. As a result, synthetic scenarios estimate similar values of concentration fluxes at the inlet of EM and WT with respect to the base case scenario (Figure 4.9). Therefore, the current model does not show capabilities to reproduce synthetic or future scenarios as shown in the results of this section.

The lessons learned from these results lead us to propose an alternative for the solution of this problem. The boundary condition at the bed needs to be modified as suggested in subsection of Limitations of Boundary and Initial Conditions, to restrict the supply of sediment from the bed, and to input a different sediment grain size to be more similar to field observations. Some improvements on the simulations may be achieved by setting the concentration fluxes at the rapid, rather than at the domain boundary inlet, to control the input of deposition fluxes into the main channel and the lateral separation zone. The step perturbation imposed at the inlet velocity to ensure fully developed turbulence should be modified for a cycled velocity field to decrease the bed erosion at the inlet of the river-transect.

DISCUSSION

Model Validation

Validation of the DES-3D sediment model can be performed employing a qualitative method to identify the zones of simulated net deposition (Figure 4.2) in comparison with postflood field bathymetry (surveys are reported in Wright and Kaplinski 2011).

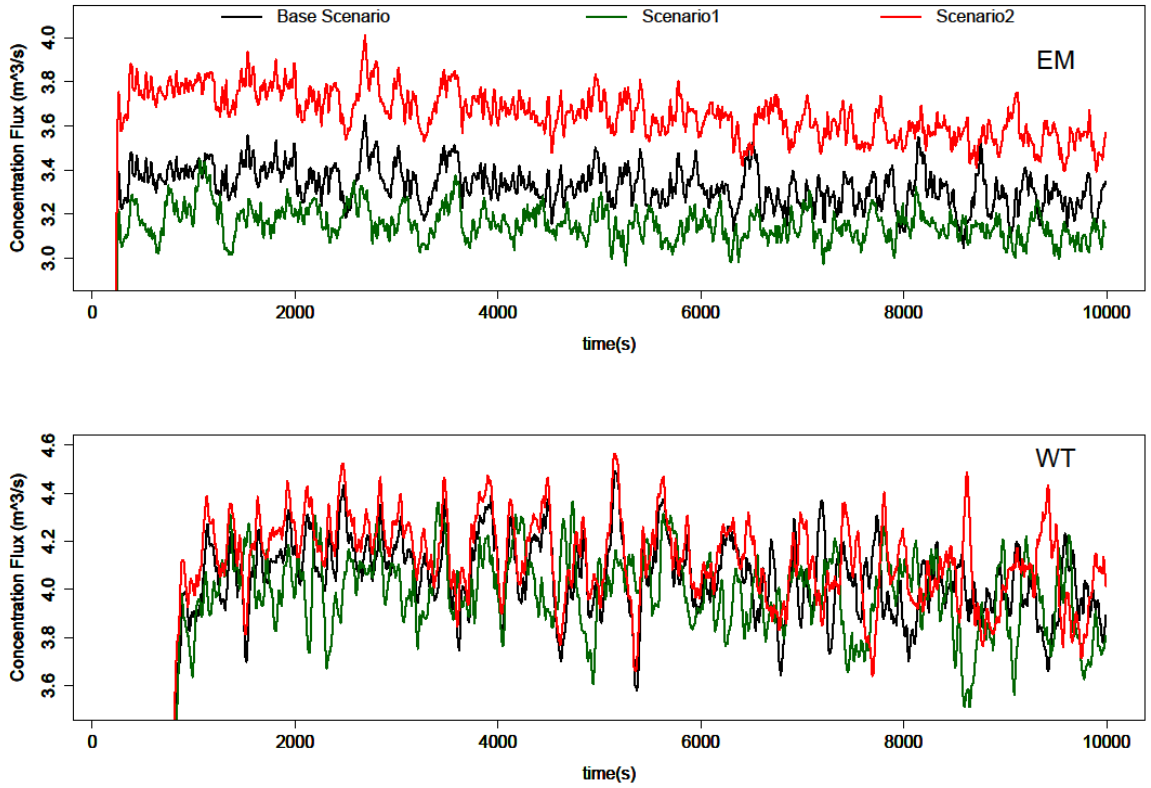

Figure 4.9. Comparison of concentration fluxes in a cross-section imposed at the inlet of the lateral separation zone, at both eddy fan complexes. Results are output every recorded step (10 seconds) of each simulation scenario. Black line represents the base case scenario, green line, scenario 1 and dark-red, scenario 2. The first 1000 seconds (not shown here) were used to spin-up the model before realistic runs are attained.

The current model needs improvements to enhance its predictive capabilities before a qualitative validation process can be conducted. Otherwise, model results would show high error values, indicating low predictability of net deposition. The field results, presented in the study of Wright and Kaplinski (2011), show a pattern of entrainment in the main channel and the convergence zone between the return current and main channel, while deposition occurs in the separation and reattachment zones and the left side banks. Modeling results partially differ with observations since results show high net erosion

values at the rapids. The eroded sediment is transported downstream resulting in over estimation of sediment at the lateral separation zones and main channel (see Video 2).

The current DES-3D sediment model can be improved by imposing different and spatially-distributed sediment grain sizes. Sand soil should be imposed as bed boundary condition at the lateral separation zones and main channel. On the other hand, pebble and cobble grain sizes should be set as bed boundary conditions at the rapids, to avoid the over estimation of net erosion observed in the results of this DES-3D-sediment model. Thus, an improvement of model predictability to simulate the redistribution of sediment during the controlled flood can be achieved. After this phase, a quantitative validation process could be developed through an assessment based on other studies of fine sediment distribution (e.g Mueller et al. (2014), Topping et al.2000a, Topping et al.2000b).

Capabilities and Limitation of the DES-3D Sediment Model

Chapter 2 has shown that dam discharge ramp rate is probably not the main factor in the process of erosion in the sandbar faces. Instead mass loss of sandbar is mostly dependent on sediment transport by turbulent flow (Alvarez and Schmeeckle 2013). A DES-3D sediment model is employed to study the flow and sediment dynamics of lateral separation zones, recognizing the important role that these processes play in the erosion and replenishment of eddy bars.

Several previous two-and three dimensional quasi-steady models have achieved a general estimation of turbulent flow fields and sediment transport at EM and WT. However, these previous models did not achieve enough predictive capabilities at simulating the pulsations in charge of the import and export of sediment within the eddy

zone, resulting in over prediction of sediment supply (Sloff et al. 2009; Logan et al. 2010; Sloff et al. 2012). This DES-3D sediment model is developed to enhance and improve predictions of sediment supply within the lateral separation zones. The DES-3D technique provides a fully resolved simulation of turbulence and sediment transport larger than the sub-grid scale at the river-reach scale, which preclude the steady flow condition that may play a role in the over prediction of deposition of sediment in the lateral separation zone.

Turbulence resolving models may not be suitable to simulate rivers at large spatial scale during long term periods. This study evidences that the scope of spatial and temporal scales are limited. Better fidelity in river numerical model requires higher computational cost. With parallelization, this fully-resolved DES sediment model was feasible to run and converge. However, 150 processors during 6 days of real time were required to run the model to output a simulated time equal to 2 hours and 45 minutes in a river transect of 1.4 kilometers and a domain grid of 5.4 million cells.

The computational expenses of this model were necessary and reasonable for the objectives of studying unsteady, resolved turbulent structures coupled with a continuum sediment transport model at high spatial and temporal resolutions. Nevertheless with the current computational capabilities, expenses can be significantly reduced by simplifying the grid domain and coarsening temporal scales. Therefore, this flow and sediment turbulence resolving model may not be suitable yet to simulate rivers at large spatial scales and long term simulations due to the communication issues and efficiency limitations of supercomputers at the current time. However, this limitations of the DES-3D model working at larger spatial and longer temporal scales, might be overcome when

future computational power allows massive and fully distributed simulations in short time. The DES-3D model can also be adjusted employing a time factor to simulate longer-time scales (see the future work section).

FUTURE WORK

Future work might pursue the application of the DES-3D sediment model coupled with a bed evolution model to study river channel changes. The suggested study can be novel as it addresses the timescale difference between the high temporal-resolution of this DES-3D model and long term scale of a morphodynamic model. The DES-3D model, developed in this research work, is computational expensive, but might be able to simulate long-term processes occurring on time scales of days. The proposed DES-3D morphodynamic model may have some important capabilities. For instance, the model may be capable to simulate the entire three days of flood controlled discharge released from the Glen Canyon Dam in 2008.

The challenge of developing a DES-3D morphodynamic model rely on adjusting a time scale factor to allow the coupling of patterns observed in the DES-3D sediment model (at the scale of hours) with geomorphologic processes occurring at time scale of days. A suggested methodology is to employ an iterative procedure to calculate the flow and sediment rates at every time step, re-mesh the topographic domain to account for erosion and deposition, and finally, apply the time scale factor to match the temporal bed changes. The benefit of a DES-3D geomorphologic model is the data available for validation. A validation and calibration of the DES-3D geomorphologic model can be performed by comparing the simulated channel change with Digital Elevation Model (DEM) observations taken during the Flood Controlled Released of 2008.

SUMMARY AND CONCLUSIONS

The development and implementation of a coupled flow turbulence and sediment resolving model is presented in this chapter. This model is referred to as DES-3D sediment model. The model employs a Detached Eddy Simulation (DES) technique to fully-resolve the governing Navier Stokes equations coupled to a continuum formulation of the advection-diffusion equation above the grid scale, while the (SGS) fields are modeled using the Spallart Allmaras closure model. The numerical methodology is described in detail comprising the grid domain and time of simulation, governing equations, initial conditions and the grain size distribution. This current model employs a fixed riverbed boundary condition and therefore, this current model does not incorporate bed evolution. The code used to compile the concentration and sediment transport fields is attached in Appendix E

The DES-3D sediment model has been applied to lateral separation zones located at two fan eddy complexes, named Eminence Break and Willie Taylor, along the Colorado River. Results are presented as it follows: (1) concentration patterns at the bed, (2) erosion and deposition patterns, (3) spatial average rates of erosion and deposition, (4) grain size distribution, and (5) synthetic scenarios.

The simulated results show a pattern of unsteady pulsations in the exchange of concentration between the primary eddy and the main channel. This exchange occurs at the convergence zone (located at the dividing surface between the return current and main channel) and divergence zone (formed in the reattachment zone). The unsteady pulsations of concentration are more accentuated at the convergence zone, but still evidenced at the divergence zone. Along the simulated river-reach, the concentration

values increase in the constrictions and decrease in the main channel, which is correlated with the flow streamlines convergence in the rapids and streamlines divergence of flow along the main channel.

The processes of deposition fluxes highly determine the predictive capabilities of the DES-3D model to accurately simulate the deposition at the eddy. At the lateral separation zone, high frequency pulsations of deposition fluxes are observed in the import and export of sediment between the primary zone and the main channel. At both rapids, net erosion is observed due to the high shear stress present in these constrictions. At the reattachment and separation zones, positive net deposition is observed with relatively constant values. The net deposition and deposition flux values play an important role in the replenishment of sand bars, since these are zones of storage of fine deposits.

The estimation of grain size distribution has several utilities since it discretizes the concentration values and net sediment by soil group size. Five particle size groups corresponding sand-silt, fine-sand and medium sand were tested during the simulation. The analysis shows the redistribution of the grain size at the end of the simulation compared with the initial condition. The general pattern suggested that the smallest soil particles (silt-sand, mean diameter equal to 0.08 mm) tend to deplete along the simulated river-reach transect. On the other hand, fine sand-soil (mean diameter ranging from 0.12mm to 0.2 mm) has the most redistribution during the simulation. High percentage of sand-soil contributes to the formation of eddy bars. The last group corresponding to medium sand (0.3 mm) remains in the inlet and main channel and shows low redistribution after the simulation.

The simulated results evidence some limitation of this current DES-3D sediment model, mostly based on the prescribed initial and boundary conditions. The unlimited supply of sediment at the bed, and the non-spatially distributed sediment grain sizes lead to some drawbacks on the estimation of erosion and sediment fluxes in the base case and synthetic scenarios. The erosion patterns at the rapids were not well captured, resulting in over prediction of net erosion. Further work needs to address better fidelity on the initial and boundary conditions that reflect the patterns observed in the field, specifically the sediment supply and grain size distribution at the bed. Some methodologies were suggested in previous sections of this chapter to enhance predictive capabilities of the DES-3D sediment model.

Overall, the purpose of developing a DES solver within OpenFOAM to simulate sediment transport at the scale of the river-reach was achieved. The model has potential predictive capabilities to simulate the behaviors of concentration, deposition fluxes and grain size distribution in the lateral separation zones at EM and WT. The model runs and convergences well after 2 hours and 45 minutes of simulation and shows positive advances towards the application of turbulence and sediment resolving models in at the scale of a river reach.

CHAPTER 5

SYNTHESIS AND FUTURE WORK

This chapter presents a synthesis and summary of the main conclusions found and explained in detail in Chapters 2, 3 and 4. Overall, this thesis presents a quantitative analyses based on laboratory data and numerical modeling to advance the state of knowledge of turbulence, sediment transport and sandbar failures. The methodology combines a full-scale laboratory model and the development and application of a parallelized, three-dimensional turbulence-resolving model coupled to a continuum formulation of sediment transport.

Chapter 2 presents the study of the effects of imposed restrictions on dam discharges in sandbar failures, using a full-scale laboratory model. The study area are the sandbar beaches located along the Colorado River downstream the Glen Canyon Dam. From 1964 to 1991, Glen Canyon Dam was operated to supply electricity at peak demand. The Glen Canyon Environmental Studies Report (U.S Department of the Interior, 1988) stated that these large stage fluctuations were eroding sandbars. Subsequently, the policies for operation of Glen Canyon Dam were modified, transitioning from the interim dam operation regime (1991 to 1996) to the Modified Low Fluctuation Flow (MLFF). Minimum releases were constrained to 226.5 m^3/s by day and 141.5 m^3/s by night, maximum releases to 708 m^3/s and maximum daily fluctuations within 24 hours to 226.5 m^3/s. Discharge ramp rates were confined to113 and 42.5 m^3/s /h along the rising and falling limbs respectively (U.S. Department of the Interior, 2008). The laboratory experiments simulate historical downramp rates comprising the unrestricted downramp rates and the MLFF operation criteria.

Chapter 3 and Chapter 4 present the development and validation of parallelized, three-dimensional, flow turbulence and sediment resolving models at the scale of a river reach, using a Detached Eddy Simulation technique. These models have been applied to study the flow structures and sediment transport in lateral separation zones located in two pools along the Colorado River during the peak controlled flood of 2008. The development and validation of the three dimensional turbulence resolving model is shown in Chapter 3, while the three dimensional flow and sediment coupled-turbulence resolving model is presented in Chapter 4.

FULL-SCALE LABORATORY EXPERIMENTS OF SANDBAR EROSION BY RIVER STAGE FLUCTUATIONS

Chapter 2 shows the results of the study of sandbar slope stability in Marble and Grand Canyons. These sandbars extend from the Glen Canyon dam along the Colorado River to the river kilometer 363. The experimental work has the purpose of evaluating whether the restriction of maximum ramp rates, imposed in the dam operation criteria, plays a role in the mitigation of sandbar mass loss due to mass failure and seepage erosion. A total of 22 laboratory experiments were conducted using a full-scaled physical model to simulate a range of river stage and groundwater fluctuations that occur or can occur in 47 sandbars located along the Colorado River from Glen Canyon to Diamond Creek. The experiments tested 3 different slope categories: low slopes (12 degrees), intermediate slopes (18 degrees and 22 degrees) and steep slopes (26 degrees).

The results from the laboratory experiments allowed concluding that mass failure and seepage erosion highly depends on the effect of sandbar slope steepness rather than the effect of river stage fluctuations. In other words, once a bar reaches the equilibrium

slope (14 degrees), it becomes insensitive to mass failures. In absence of other processes, any river stage fluctuation would rapidly erode newly deposition in steep sandbar beaches until the equilibrium slopes is reached and, at that time, erosion by mass failure and seepage processes largely ceases.

This chapter of the dissertation reveals that restricting maximum ramp rates in the operation of Glen Canyon Dam does not play a primary role in the continued erosion of Marble and Grand Canyon sandbars. Further, greatly increased diurnal dam discharge ramp rates, above the current dam operation criteria, should have little effect on the mass loss. Furthermore, a large increase in dam discharge downramp rates results only in moderate increases in stage ramp rates at individual sites. Other factors, such as the waves below the water surface and the sediment transport by turbulent flow could be the critical factors in determining the long-term erosion of sandbars. Chapter 3 and Chapter 4 are dedicated to study the turbulent flow and sediment transport as main processes responsible for erosion of sandbars.

Finally, it is important to remark that the conclusions reached in this section of the thesis are based on laboratory work which simplifies the erosion processes of the Colorado River sandbars. The laboratory experiments do not simulate significant cross-bar terrain variations that can locally increase groundwater exfiltration. Furthermore, the complex and layered grain size structure of sandbars material is largely simplified through the use of a more homogeneous sand mixture that could affect the spatial variability of some soil parameters like hydraulic conductivity and the internal friction coefficient.

TURBULENCE RESOLVING MODELING OF LATERAL SEPARATION ZONES ALONG A CANYON-BOUND RIVER USING DETACHED EDDY SIMULATION TECHNIQUE

Chapter 3 encompasses the development, application and validation of a parallelized, three-dimensional, turbulence-resolving model at the scale of a river reach, using a Detached Eddy Simulation technique. The forecasting capabilities of the three-dimensional DES flow model are assessed using ADCP flow measurements taken during the 2008 controlled flood release from Glen Canyon Dam. A point-to-point verification method and a spatial distribution analysis of the magnitude and direction, often employed in atmospheric and hydrological research, is used for model validation. Time-averaged simulated velocities are compared against time-averaged observed velocity data at 4920 collocated points. The spatio-temporal properties of simulated velocity magnitudes are assessed based on probability density and cumulative distribution functions and six skill metrics.

The skill metrics include four absolute error metrics: Mean Absolute Error (MAE), Mean Forecast Error (MFE), Root Mean Square Error (RMSE) and Pearson correlation coefficient (R); and two relative error metrics: Mean Absolute Percentage Error (MAPE) and Median Absolute Percentage Error (MdAPE). Velocity directions are evaluated by computing the dot product between simulated and measured velocity unit vectors. These skill metrics show a good fit between observed and simulated density functions. The relatively small values of the forecasting metrics and the high correlation coefficient between observations and simulated results also confirm the predictive capabilities of the model.

The simulation of main recirculation currents present in the lateral separation zones is compared with a two-dimensional depth-averaged closure flow model. The DES-3D model predicted a wider range of turbulent flow structures that more closely resembled structures observed in the field. The DES-3D reproduces the size and position of the primary and secondary lateral recirculation flows and the strength of the return current. The two-dimensional turbulence-closure model captures a strong recirculation zone characterized by one steady primary eddy cell, failing to predict the secondary recirculation zones and the strength of the return current.

Three-dimensional flow structures were simulated based on cross-sectional panels, velocity vector structures, directional distributions, and vorticity and Q-criterion. Large vorticity structures produced at the free shear layer becoming three-dimensional with no preferred orientation further downstream. Significant differences are found between near-bed and surface velocity vector directions which generate an Ekman inward spiral at the primary eddy at both sites along the vertical axis centered in the eddy eye. Finally, the model was able to capture eddy pulsations due to eddy vortex structures.

In summary, the flow structures captured with the DES-3D model are consistent with field observations. The predictive capability of this model elucidates the possibility to apply it as a tool to further testing flood release discharge scenarios or future operation criteria from the Glen Canyon Dam.

CONCENTRATION OF SUSPENDED SEDIMENT IN LATERAL SEPARATION ZONES: FIELD SCALE DETACHED EDDY SIMULATION MODEL

The DES-3D flow model is coupled to a continuum formulation of the sediment continuity equation. The flux form of the Smith and McLean suspended sediment

boundary condition is used to calculate erosion and deposition rates. The DES decomposition of the DES-3D sediment model follows the same procedure of the DES-3D flow model (see Chapter 3), where variable fields greater than the grid scale are fully resolved and the sub-grid-scale (SGS) variables are modeled using the rough wall extension of the Spalart-Allmaras model. Thus, the model resolves large-scale turbulence using DES and simultaneously integrates the sediment advection-diffusion equation, wherein advection is provided by the DES velocity field minus particle settling velocity, and diffusion is provided by the sub-grid or RANS eddy viscosity.

The DES-3D sediment model is applied to the same lateral separation zones (EM and WT) and it uses the same numerical domain of the DES-3D flow model. This model is 10 times computational more expensive than the flow model with a time of simulation of 10000 seconds. 30 times of flow at the reach-averaged velocity through the numerical domain, inlet to outlet, was required for statistical convergence. 6 days of processing time on the A2C2 supercomputer were required to simulate these 2 hours and 45 minutes. The model estimates the grain size distribution throughout the river-reach transect using a mixing layer model. Five groups of sediment sizes are employed in the suspended-sediment model, which implies five coupled-solutions of the advection-diffusion equation.

The concentration pattern, deposition fluxes, sediment grain size distribution and synthetic scenarios were studied using this model. Results show that concentration is exchanged between the lateral separation zone and main channel following a pattern of unsteady fluctuations. The concentration values increase in the rapids and decrease in the

main channel, which is correlated with the flow streamlines convergence in the rapids and streamlines divergence along the main channel.

The accurate simulation of deposition fluxes highly determines the supply of sediment in the lateral separation zones. High frequency pulsations of deposition fluxes are observed in the import and export of sediment between the primary zone and the main channel. These high frequency and unsteady pulsations observed in the interaction between the eddy zone and the main channel is an indicative of unsteady exchange of sediment fluxes, which might be the key factor for accurate prediction of supply of sediment in the eddy zone.

The grain size distribution shows a pattern of depletion of sand silt throughout the main channel, while fine sand provides the major contribution to the lateral separation zones and the medium sand is not likely to move during the simulation. The advantage of this grain size distribution tool is the flexibility to input different grain size groups. Future work may address different grain size diameters and a wider distribution to study the redistribution of other type of soil particles along the simulated river-reach.

The DES-3D sediment model shows some difficulties at predicting the erosion and sediment patterns due to the limitations carried by the initial and boundary conditions. The unlimited supply of sediment at the bed, and the non-spatially distributed sediment grain sizes lead to drawbacks in the accuracy of the simulation of deposition fluxes at the rapids. Further work needs to be developed to achieve better fidelity on the simulation of erosion and deposition patterns, and the systematic patterns of grain size distribution occurring at the fan eddy complexes. Some methodologies were suggested in Chapter 4 to enhance predictive capabilities of the DES-3D sediment model.

Synthetic scenarios were performed in the same river-reach varying the initial condition of concentration. Results indicate that regardless of the initial condition, the unlimited supply of sediment from leads to high concentration fluxes, resulting in non-differences between scenarios at the inlet of the eddy zone. As a consequence, an inter-comparison of synthetic scenarios was not feasible to achieve at this developing phase of the model and future improvements must be done, specifically on the accurate simulation of sediment supply from the bed.

It is important to address the limitations of this model in terms of computational expenses. The DES model can be more accurate than other two and three-dimensional quasi-steady models but requires significantly higher computational cost. With parallelization, this fully-resolved DES sediment model was feasible to run and converge. However, 150 processors during 4 days of real time were required to run the model to output a simulated time equal to 2 hours and 45 minutes in a river transect of 1.4 kilometers and a domain grid of 5.4 million cells. This model may not be suitable to simulate long river transects at this current time, but long-term simulations might be achieved using a time scale factor (see section of future work).

FUTURE WORK

This research elucidates a framework for integrating turbulence-resolving models to the study of complex river configurations. Computational Dynamic Models (CFD) based on DES techniques are significantly more accurate than two and three-dimensional quasi-steady models. Nevertheless, DES techniques are substantially more computational expensive requiring parallelization with the use of multiple processors of a supercomputer. In cases such as the lateral recirculation zones, observed in the Colorado

River, computational expenses of turbulence-resolving model are essential as other two and three-dimensional quasi-steady models have proven difficulties to predict flow, sediment transport and channel changes in this complex system.

The results found this research work elucidate new lines of investigations. For instance, future work can be oriented to the application of this DES-3D model to other types of river configurations featured by flow separation zones, e.g. sharp meanders, channel constrictions, many engineering structures, riparian ecosystem that are featured by large scale flow separation, secondary eddy zones and free shear layers.

The DES-3D sediment model can be expanded to study river channel changes. The model can be coupled to a morphodynamic model to quantify the long term deposition fluxes and, therefore, changes in river morphology. The methodology suggested for river channel changes consists in employing a time scale factor to rescale the deposition fluxes at the bed and thus, estimate long-term changes in net deposition. This process demands several iterations to find the time scale factor to achieve model convergence at a reasonable computational expense. DES techniques are relatively new in fluvial numerical modelling and few authors have incorporated a time scale factor to rescale the temporal deposition fluxes. The research study done by Logan et al. (2010) introduced a time scale factor to their sediment transport model to study lateral separation zones (Logan et al. 2010). However, this study does not specify a methodology to determine a time scale factor. After this factor is estimated, the numerical domain has to be redefined for channel changes. The redefinition process of the mesh to adjust for riverbed evolution can become a difficult process in structured grid cells because the mesh has to fulfill the grid topology requirements to guarantee orthogonality in cells.

REFERENCES

Akahori, R., 2007. *Modeling sediment transport in eddy recirculation zones of the Colorado River in Grand Canyon*, Ph.D thesis, 206 pp, Arizona State University.

Alvarez, L.V., Schmeeckle, M.W., 2013. Erosion of river sandbars by diurnal stage fluctuation in the Colorado River in the Marble and Grand Canyons: full-scale laboratory experiments, *River Res. Applic. 29*, 839-854, doi: 10.1002/rra.2576.

Aupoix, B., Spalart, P., 2003. Extensions of the Spalart-Allmaras turbulence model to account for wall roughness. *Int. J. Heat Fluid Flow. 24*, 454-462, doi: 10.1016/S0142-727X(03)00043-2.

Bauer, B.O., Schmidt J.C., 1993. Waves and sandbar erosion in the Grand-Canyon - applying coastal theory to a fluvial system. *Ann. Assoc. Am. Geogr*. 83: 475-497. DOI: 10.1111/j.1467-8306.1993.tb01946.x

Best, J.L., 1988. Sediment transport and bed morphology at river channel confluences. *Sedimentology*, 35, 481; 481-498; 498, doi: 10.1111/j.1365-3091.1988.tb00999.x.

Beus, S.S, Avery C.C., Stevens, L.E., Kaplinski, M., Cluer B.L., 1992. The influence of variable discharge regimes on Colorado River sand bars below Glen Canyon Dam: Final Report to the National Park Service. Northern Arizona University, Flagstaff, Arizona.

Bradbrook, K.F., Lane, S.N., Richards, K.S, Biron, P., Roy, A., 2000a. Large eddy simulation of periodic flow characteristics at river channel confluences. *J. Hydraul. Res.*, 38, 207-215, doi: 10.1080/00221680009498338.

Bradbrook, K.F., Lane, S.N., Richards, K.S., 2000b. Numerical simulation of three-dimensional, time-averaged flow structure at river channel confluences. *Water Resour. Res.* 36, 2731-2746, doi: 10.1029/2000WR900011.

Budhu M., Gobin R., 1994. Instability of sandbars in Grand-Canyon. *J. Hydraul. Eng-ASCE* 120: 919-933.

Budhu M., Gobin R., 1995. Seepage-induced slope failures on sandbars in Grand Canyon. *J. Geotech. Eng-ASCE* 121: 601-609.

Cao, Z., Carling, P.A., 2002. A critical reflection of computational fluid dynamics applications to fluvial sedimentary systems. *International Association of Hydrological Sciences, Publication*: 463-470.

Chang, W., Constantinescu, G., Lien, H., Tsai, W., Lai, J., Loh, C., 2013. Flow structure around bridge piers of varying geometrical complexity. *J. Hydraul. Eng.* 139, 812-826.

Cigizoglu, H.K., 2004. Estimation and forecasting of daily suspended sediment data by multi-layer perceptrons. *Adv.Water Resour., 27,* 185 – 195, doi:10.1016/j.advwatres.2003.10.003.

Cluer B.L., 1995. Cyclic fluvial processes and bias in environmental monitoring. Colorado River in Grand Canyon. *J. Geol.* 103: 411-421.

Constantinescu, G., Koken, M., Zeng, J., 2011a. The structure of turbulent flow in an open channel bend of strong curvature with deformed bed: Insight provided by detached eddy simulation. *Water Resour. Res. 47, W05515, doi:10.1029/2010WR010114.*

Constantinescu, G., Miyawaki, S., Rhoads, B., Sukhodolov, A., Kirkil, G., 2011b. Structure of turbulent flow at a river confluence with momentum and velocity ratios close to 1: Insight provided by an eddy-resolving numerical simulation. *Water Resour. Res.* 47, W05507, doi: 10.1029/2010WR010018.

Converse Y.K., Hawkins C.P., Valdez R.A., 1998. Habitat relationships of subadult humpback chub in the Colorado River through Grand Canyon: spatial variability and implications of flow regulation RID A-4530-2008. Regul. River. 14: 267-284.

Darby S.E., Thorne C.R.,1996. Numerical simulation of widening and bed deformation of straight sand-bed rivers. I: Model development. *J. Hydraul. Eng.* 122: 184‑193.

Darby S.E., Rinaldi, M., Dapporto, S., 2007. Coupled simulations of fluvial erosion and mass wasting for cohesive river banks. *J. Geophys. Res.* 112: F03022. DOI: 10.1029/2006JF000722.

Dodrill M.J., Yackulic, C.B., Gerig, B., Pine, W.E., Korman J., Finch, C., 2015. Do management actions to restore rare habitat benefit native fish conservation? Distribution of juvenile native fish among shoreline habitats of The Colorado River, *River Res. Applic,* doi: 10.1002/rra.2842

Drake D.E., Cacchione, D.A., 1988. Estimates of the reference concentration (C_a) and resuspension coefficient (γ_o) from near-bottom observations on the California shelf, *Cont. Shelf Res.*

Draut A.E., Rubin, D.M., 2008. The role of eolian sediment in the preservation of archeologic sites along the Colorado River corridor in Grand Canyon National Park, Arizona. U.S. Geological Survey, Professional Paper 1756.

Dunn, R.J. H., Willett, K.M., Thorne, P.W., Woolley, E.V., Durre, I., Dai, A., Parker, D. E., Vose, R.S., 2012. HadISD: a quality-controlled global synoptic report database for selected variables at long-term stations from 1973-2011. *Clim. Past.* 8, 1649-1679.

Ferguson, R.I., Parsons, D.R., Lane, S.N., Hardy, R.J., 2003. Flow in meander bends with recirculation at the inner bank. *Water Resour. Res.* 39, - 1322, doi: 10.1029/2003WR001965.

Ferziger, J.H., 1976. Large eddy simulation of turbulent flows. *AIAA* 76-347.

Ferziger, J.H., Peric, M., 2002. *Computational methods for fluid dynamics*. Springer, Berlin, New York, 423 pp.

Galperin, B., Orszag S.A., 1993. *Large eddy simulation of complex engineering and geophysical flows*. Cambridge University Press, 600 pp.

Garcia, M., Parker, G., 1991. Entrainment of sediment into suspension. *J. Hydraul. Eng.* 117: 414-433.

Garrett, W.B., Van De Vanter, E.K., Graf, J. B., 1993. United States Bureau of Reclamation, and Geological Survey, Streamflow and sediment-transport data, Colorado River and three tributaries in Grand Canyon, Arizona, 1983 and 1985-*86*, 93-174, 624.

Gerig, B., Dodrill, M.J., Pine, W.E.III., 2014. Habitat selection and movement of adult Humpback Chab in the Colorado River in Grand Canyon, Arizona, during an experimental steady flow release. *North. Am. J. Fish. Mana.* 12: 39-48, doi: 10.1080/02755947.2013.847880

Grams, P.E., Schmidt, J.C., 1999. Geomorphology of the green river in the eastern Uinta Mountains, Dinosaur National Monument, Colorado and Utah. *Varieties of Fluvial Forms.* A. J Miller, A. Gupta (Eds.), Wiley, Chichester, UK pp. 81-111.

Grams, P.E., Schmidt, J.C., Topping J. D., 2007. The rate and pattern of bed incision and bank adjustment on the Colorado River in Glen Canyon downstream from Glen Canyon Dam, 1956-2000. *Geo. Soc. Am Bull.*, 119, 556-575, doi: 10.1130/B259691.

Green T.R., Beavis S.G., Dietrich C.R., Jakeman A.J., 1999. Relating stream-bank erosion to in-stream transport of suspended sediment. *Hydrol. Process.* 13: 777‑787. DOI: 10.1002/(SICI)1099-1085(19990415)13:5<777::AID-HYP780>3.0.CO;2-P.

Grigoriadis, D., Dimas, A., Balaras, E., 2012. Large-eddy simulation of wave turbulent boundary layer over rippled bed. *Coast. Eng.* 60, 174-189. doi:10.1016/j.coastaleng.2011.10.003.

Gupta, H.V., Wagener, T., Liu, Y., 2008. Reconciling theory with observations: elements of a diagnostic approach to model evaluation. *Hydrol. Process.* 22, 3802-3813, doi: 10.1002/hyp.6989.

Gupta, H.V., Kling, H., 2011. On typical range, sensitivity, and normalization of mean squared error and Nash-Sutcliffe efficiency type metrics. *Water Resour. Res.* 47, W10601, doi: 10.1029/2011WR010962.

Hazel J.E, Kaplinski M., Parnell R., Kohl K., Topping D.J., 2006a. Stage-discharge relations for the Colorado River in Glen, Marble, and Grand Canyons, Arizona. U.S. Geological Survey, Open File Report 2006‑1243.

Hazel J.E., Topping D.E., Schmidt J. C., Kaplinski, M., 2006b. Influence of a dam on fine-sediment storage in a canyon river. *J. Geophys. Res.* 111: F01025. DOI: 10.1029/2004JF000193.

Hazel J.E., Grams, P.E., Schmidt, J C., Kaplinski, M., 2010. Sandbar response in Marble and Grand Canyons, Arizona, following the 2008 high-flow experiment on the Colorado River. U.S. Geological Survey, Scientific Investigation Report 2010-5015.

Hereford, R., Fairlye, H.C., Thompson, K.S., Balson, J.R., 1993. Surficial geology, geomorphology, and erosion of archeologic sites along the Colorado River, eastern Grand Canyon, Grand Canyon National Park, Arizona. U.S. Geological Survey, Open-File Report 93-517.

Hill, P.S., Nowell, A.R.M., Jumars, P.A., 1988. Flume evaluation of the relationship between suspended sediment concentration and excess boundary shear stress *J. Geophys. Res*. 93: 12,499-12,509.

Horel, J., Splitt, M., Dunn, L., Pechmann, J., White, B., Ciliberti, C., Lazarus, S., Slemmer, J., Zaff, D., Burks, J., 2002. Mesowest: Cooperative Mesonets in the Western United States. *Bull. Am. Meteorol. Soc.* 83, 211, doi: http://dx.doi.org/10.1175/1520-0477(2002)083<0211:MCMITW>2.3.CO;2.

Howard A., Dolan R., 1981. Geomorphology of the Colorado River in the Grand-Canyon. *J. Geol.* 89: 269-298.

Hunt, J.C.R., Durbin, P. A., 1999. Perturbed vortical layers and shear sheltering. *Fluid Dyn. Res.* 24, 375-404, doi:10.1016/S0169-5983(99)00009-X.

Kackel, N., Smith J.D., 1986. Geological impact of sediment transporting events on the Washington continental shelf, in Shelf Sands and Sandstones, edited by Knight R.J, McLean J.R, pp. 145-162, Canadian Society of Petroleum Geologists, Calgary, Alberta, 1986.

Kang, S., Sotiropoulos, F., 2011. Flow phenomena and mechanisms in a field-scale experimental meandering channel with a pool-riffle sequence: insights gained via numerical simulation. *J.Geophys. Res.* 116, F03011, doi: 10.1029/2010JF001814.

Kearsley, L.H., Schmidt, J. C., Warren, K.D., 1994. Effects of Glen Canyon Dam on Colorado River sand deposits used as campsites in Grand Canyon National Park, USA. *Regul. River.* 9: 137-149.

Keylock, C.J, Constantinescu, G., Hardy, R.J., 2012. The application of computational fluid dynamics to natural river channels: Eddy resolving versus mean flow approaches. *Geomorphology* 179, 1-20.

Keylock, C.J, Tokyay, T.E., Constantinescu, G., 2011. A method for characterizing the sensitivity of turbulent flow fields to the structure of inlet turbulence. *J. Turbulence*. 12, N45, doi: 10.1080/14685248.2011.636047.

Keylock, C.J, Hardy, R., Parsons, D., Ferguson, R., Lane, S., Richards, K., 2005. The theoretical foundations and potential for large-eddy simulation (LES) in fluvial geomorphic and sedimentological research. *Earth-Sci. Rev.* 71, 271-304, doi:10.1016/j.earscirev.2005.03.001.

Kirkil, G., Constantinescu, G., Ettema, R., 2009. DES investigation of turbulence and sediment transport at a circular pier with scour hole, *J. Hydraul. Eng.* 135, 888-901, doi: 10.1061/(ASCE)HY.1943-7900.0000101.

Korman J., Wiele S.M., Torizzo, M., 2004. Modelling effects of discharge on habitat quality and dispersal of juvenile humpback chub (Gila cypha) in the Colorado River Grand Canyon. *River Res. Appl.* 20: 379-400. DOI: 10.1002/rra.749.

Kosovic, B., Curry, J., 2000. A large eddy simulation study of a quasi-steady, stably stratified atmospheric boundary layer. *J. Atmos. Sci.* 57, 1052-1068,doi: http://dx.doi.org/10.1175/1520-0469(2000)057<1052:ALESSO>2.0.CO;2.

Lane, S.N., Bradbrook K.F., Richards, K.S., Biron, P.A., Roy, A.G., 1999. The application of computational fluid dynamics to natural river channels: three-dimensional versus two-dimensional approaches. *Geomorphology* 29, 1-20. doi:10.1016/S0169-555X(99)00003-3

Leopold L., 1969. The rapids and the pools. Grand Canyon. U.S. Geological Survey, Professional Paper 669-D.

Logan, B., Nelson, J., McDonald, R., Wright, S.A., 2010. Mechanics and modeling of flow, sediment transport and morphologic change in riverine lateral separation zones. 2nd Joint Federal Interagency Conference. Las Vegas.

Lohmann, D., Nolte-Holube, R., Raschke, E., 1996. A large-scale horizontal routing model to be coupled to land surface parametrization schemes. *Tellus* 48: 708‑721. doi: 10.1034/j.1600-0870.1996.t01-3-00009.x.

Major, J.J., Iverson, R.M., 1999. Debris-flow deposition: Effects of pore-fluid pressure and friction concentrated at flow margins. *Geol. Soc. of Am. Bull.* 111: 1424-1434. DOI: 10.1130/0016-7606(1999)111<1424:DFDEOP>2.3.CO;2.

Malmon, D.V., Reneau, S.L., Dunne, T., Katzman, D., Drakos, P.G., 2005. Influence of sediment storage on downstream delivery of contaminated sediment. *Water Resour. Res.* 41: W05008. DOI:10.1029/2004WR003288.

Martinez, G.F., Gupta, H.V., 2011. Hydrologic consistency as a basis for assessing complexity of monthly water balance models for the continental United States, *Water Resour. Res.* 47, W12540, doi: 10.1029/2011WR011229.

Mason, P.J., 1989. Large-eddy simulation of the convective atmospheric boundary layer. *J. Atmos. Sci.* 46, 1492-1516, doi: http://dx.doi.org/10.1175/1520-0469(1989)046<1492:LESOTC>2.0.CO;2.

McDonald, R., Nelson. J. M., 1996. Field measurements of flow in lateral Separation Eddies on the Colorado River in Grand Canyon. U.S. Geological Survey, Scientific Investigation Report 1996.

Melis, T.S., 2011. Effects of Three High-Flow Experiments on the Colorado River Ecosystem Downstream from Glen Canyon Dam, Arizona. U.S. Geological Survey, Scientific Investigation Report 1366, 147p.

McLean, S.R. 1976. Mechanics of the turbulent boundary layer over sand waves in the Columbia River, Ph,D, dissertation, Univ. of Wash., Seattle.

Miller, A. J., 1994. Debris-fan constrictions and flood hydraulics in river canyons: some implications from two-dimensional flow modelling. *Earth Surf. Process. Landforms*, 19, 681-697, doi: 10.1002/esp.3290190803.

Moreno, H.A., Vivoni, E.R., Gochis, D.J., 2014. Addressing uncertainty in reflectivity-rainfall relations in mountain watersheds during summer convection. *Hydrol. Process.*, 28, 688-704, doi: 10.1002/hyp.9600.

Mueller, E.R., Grams, P.E., Schmidt, J.C., Hazel Jr, J.E., Alexander, J.S., Kaplinski., M., 2014. The influence of controlled floods on fine sediment storage in debris fan-

affected canyons of the Colorado River basin. *Geomorphology* 226, 65-75, doi:10.1016/j.geomorph.2014.07.029.

Nadaoka, K., Yagi, H., 1998. Shallow-water turbulence modeling and horizontal large-eddy computation of river flow. *J. Hydraul. Eng-ASCE* 124, 493-500.

Nelson, J.M., Bennett, J.P., Wiele, S.M., 2003. *Flow and sediment-transport modeling, Tools in fluvial geomorphology*. Wiley, New York, Ch. 18, 539-576.

Nicholas, A.P., Sambrook Smith, G.H., 1999. Numerical simulation of three-dimensional flow hydraulics in a braided channel. *Hydrol. Process.* 13: 913‐929, doi: 10.1002/(SICI)1099-1085(19990430)13:6<913::AID-HYP764>3.0.CO;2-N.

Nikora, V., McEwan, I., McLean, S., Coleman, S., Pokrajac, D., Walters, R., 2007. Double-averaging concept for rough-bed open-channel and overland flows: Theoretical background. *Journal of Hydraulic Engineering* 133: 873-883

Papanicolaou, A.N., Kramer, C.M., Tsakiris, A.G., Stoesser, T., Bomminayuni, S., Chen, Z., 2012. Effects of a fully submerged boulder within a boulder array on the mean and turbulent flow fields: Implications to bedload transport. *Acta Geophys.* 60, 1502-1546.

Passalacqua, P., Porte-Agel, F., Foufoula-Georgiou, E., Paola, C., 2006, Application of dynamic subgrid-scale concepts from large-eddy simulation to modeling landscape evolution. *Water Resour. Res.* 42, W06D11, doi: 10.1029/2006WR004879.

Piégay, H., Bornette G., Citterio A., Hérouin E., Moulin B., Stratiotis C., 2000. Channel instability as a control factor of silting dynamics and vegetation pattern within perifluvial aquatic zones. *Hydrol. Process.* 14: 3011‐3029. DOI: 10.1002/1099-1085(200011/12)14:16/17<3011::AID-HYP132>3.0.CO;2-B.

Ray, M.R., Sarma, A.K., 2011. Minimizing diurnal variation of downstream flow in hydroelectric projects to reduce environmental impact. *J. of Hydro-environ. Res*. 5: 177‐185.

Rhoads, B.L., Kenworthy, S.T., 1995. Flow structure at an asymmetrical stream confluence. *Geomorphology* 11, 273-293, doi:10.1016/0169-555X(94)00069-4.

Rinaldi, M., Casagli, N., Dapporto, S., Gargini, A., 2004. Monitoring and modelling of pore water pressure changes and riverbank stability during flow events. *Earth Surf. Processes* 29: 237-254. DOI: 10.1002/esp.1042.

Rubin, D., McDonald, R., 1995. Nonperiodic eddy pulsations. *Water Resour. Res.* 31, 1595-1605, doi: 10.1029/95WR00472.

Rubin, D.M., Nelson J.M., Topping D.J., 1998. Relation of inversely graded deposits to suspended-sediment grain-size evolution during the 1996 flood experiment in Grand Canyon. *Geology* 26: 99-102. DOI: 10.1130/0091-7613(1998)026<0099:ROIGDT>2.3.CO;2.

Schmidt, J.C., 1990. Recirculating flow and sedimentation in the Colorado River in Grand-Canyon, Arizona. *J. Geol.* 98: 709-724.

Schmidt, J.C., Graf J.B., 1990. Aggradation and degradation of alluvial sand deposits, 1965 to 1986, Colorado River, Grand Canyon National Park, Arizona. U.S Geological Survey, Professional Paper 1493.

Schmidt, J.C., Grams, P.E., Leschin, M.F., 1999. Variation in the magnitude and style of deposition and erosion in three long (8-2 km) reaches as determined by photographic analysis. *The 1996 Controlled Flood in Grand Canyon*. Geophys. Monogr. Ser.,vol. 110, edited by R.H Webb et al., pp. 185-204, AGU, D. C.

Schmidt, J.C., Grams, P.E., Webb, R.H., 1995. Comparison of the magnitude of erosion along two large regulated rivers. *JAWRA*. 31, 617-631.

Schmidt, J.C., Rubin, D., 1995. Regulated streamflow, fine-grained deposits, and effective discharge in canyons with abundant debris fans. *Geoph. Monog Series*. 89, 177-195, doi: 10.1029/GM089p0177 .

Schmidt, J.C., Webb, R.H., Valdez, R.A., Marzolf, G.R., Stevens, L.E., 1998. Science and values in river restoration in the Grand Canyon - There is no restoration or rehabilitation strategy that will improve the status of every riverine resource. *Bioscience* 48: 735-747.

Schumm, S.A., Khan, H.R., 1972. Experimental study of channel patterns. Bulletin of Geological Society of America 88: 1755‑1770.

Sharif, H.O., Ogden, F.L., Krajewski, W.F., Xue, M., 2004. Statistical analysis of radar rainfall error propagation. *J. Hydrometeor.* 199-212, doi: http://dx.doi.org/10.1175/1525-7541(2004)005<0199:SAORRE>2.0.CO;2.

Shur, M.L., Spalart, P., Strelets, M., Travin, A., 2011a. A rapid and accurate switch from RANS to LES in boundary layers using an overlap region. *Flow Turbul. Combust.* 86, 179-206.

Sherwood, C., 2014. USGS Sediment-Transport Applet: Particle settling velocity and critical shear stress.

Simon, A., Curini A., Darby, S.E., Langendoen, E.J., 2000. Bank and near-bank processes in an incised channel. *Geomorphology* 35: 193-217.

Sinha, S.K., Sotiropoulos, F., Odgaard A.J., 1998. Three-dimensional numerical model for flow through natural rivers. *Journal of Hydraulic Engineering* 124: 13-24

Sloff, K., Nieuwboer, B., Brandy, L., Nelson, J.M., 2012. Effect of sediment entrainment and avalanching on modeling of grand canyon eddy bars, in *River Flow 2012: Proceeding of the International Conference of Fluvial Hydraulics*, CRC Press., edited by Rafael Murillo Muñoz, pp. 791-798.

Sloff, K., Wright, S., Kaplinski, M., 2009. High resolution three dimensional modeling of river eddy sandbars, grand canyon, USA, in *River Coastal and Estuarine Morphodynamics. RCEM*, CRC Press edn., edited by Carlos Vionnet, Marcelo H. Garcia, E. M. Labrubesse, and G. M. E. Perillo, pp. 883-890.

Smith, J.D., McLean, SR., 1977. Spatially averaged flow over a wavy surface *J. Geophys. Res.* 82: 1735-1746.

Spalart, P.R., 2009. Detached-eddy simulation. *Annu. Rev. Fluid Mech.*, 41, 181-20, doi: 10.1146/annurev.fluid.010908.165130.

Spalart, P., Deck, S., Shur, M., Squires, K., Strelets, M., Travin, A., 2006. A new version of detached-eddy simulation, resistant to ambiguous grid densities. *Theor. Comput. Fluid Dyn.*, 20, 181-195.

Squires, K.D., 2004. Detached-eddy simulation: current status and perspectives. *ERCOFT Ser: Direct and large-eddy simulation* 5: 465-480.

Sukhodolov, A., Uijttewaal, W.S.J., Engelhardt, C., 2002. On the correspondence between morphological and hydrodynamical patterns of groyne fields. *Earth Surf. Process.* 27, 289-305, doi: 10.1002/esp.319, doi: 10.1002/esp.319.

Topping, D.J., Rubin, D., Vierra, L.E., 2000a. Colorado river sediment transport - 1. Natural sediment supply limitation and the influence of Glen Canyon Dam. *Water Resour. Res.* 36: 515-542. DOI: 10.1029/1999WR900285.

Topping, D.J., Rubin, D.M., Nelson, J.M., Kinzel, P.J., Corson, I.C., 2000b. Colorado River sediment transport - 2. Systematic bed-elevation and grain-size effects of sand supply limitation. *Water Resour. Res.* 36: 543-570. DOI: 10.1029/1999WR900286.

Topping, D.J., Rubin, D.M., Schmidt, J.C., 2005. Regulation of sand transport in the Colorado River by changes in the surface grain size of eddy sandbars over multi-year timescales. *Sedimentology* 52: 1133-1153. DOI: 10.1111/j.1365-3091.2005.00738.x.

Tseng, Y.H., Ferziger, J.H., 2004. Large-eddy simulation of turbulent wavy boundary flow-illustration of vortex dynamics. *J. Turbul.* 5, 034, doi: 10.1088/1468-5248/5/1/034.

Turner, R.M., Karpiscak, M.M., 1980. Recent vegetation changes along the Colorado River between Glen Canyon Dam and Lake Mead. Arizona. U.S. Geological Survey, Professional Paper 1132.

Uijttewaal, W.S.J., 2005. Effects of groyne layout on the flow in groyne fields: Laboratory experiments. *J. Hydraul. Eng.* 131, 782-791.

U.S. Department of the Interior, 1988. Glen Canyon Dam Environmental Studies. Final Report. U.S. Department of the Interior, Bureau of Reclamation: Salt Lake City, Utah.

U.S Department of the Interior, 1995. Operation of Glen Canyon Dam: Final Environmental Impact Statement. U.S. Department of the Interior, Bureau of Reclamation: Salt Lake City, Utah.

U.S Department of the Interior, 1996. Record of decision, operation of Glen Canyon Dam: Final environmental impact statement. U.S. Department of the Interior, Bureau of Reclamation: Salt Lake City, Utah.

U.S Department of the Interior, 2005. Operation of Glen Canyon Dam: Final Environmental Impact Statement. U.S. Department of the Interior, Bureau of Reclamation: Salt Lake City, Utah.

U.S. Department of the Interior, 2008. Final environmental assessment experimental releases from Glen Canyon Dam, Arizona, 2008 through 2012. U.S. Department of the Interior, Bureau of Reclamation: Salt Lake City, Utah.

Van Balen, W., Uijttewaal, W.S.J., Blanckaert, K., 2010. Large-eddy simulation of a curved open-channel flow over topography. *Phys. Fluids* 22, 075108.

Viswanathan, K., Shur, M.L., Spalart, P.R., Strelets, M.K., 2007. Comparisons between experiment and large-eddy simulation for jet noise. *AIAA* 45, 1952-1966, doi: 10.2514/1.25892.

Wahl, E.R. Smerdon, J.E., 2012. Comparative performance of paleoclimate field and index reconstructions derived from climate proxies and noise-only predictors. *Geophys. Res. Lett.* 39, L06703, doi: 10.1029/2012GL051086.

Webb, R.H., Melis, T.S., Valdez, R.A., 2002. Observations of environmental change in Grand Canyon, Arizona. U.S. Geological Survey, Water-Resources Investigation Report 02-4080.

Webb, R.H., Wegner, D.L., Andrews, E.D., Valdez, R.A., Patten, D.T., 1999. Downstream effects of Glen Canyon Dam on the Colorado River in Grand Canyon: A review. In: Webb, R.H., Schmidt, J.C., Marzolf, G.R., Valdez, R.A. (Eds.), The Controlled Flood in Grand Canyon. American Geophysical Union, Washington, DC, pp. 1–21.

Wilberg, P.L., Smith, J.D., 1983. A comparison of field data and theoretical models for wave-current interactions at the bed on the continental shelf. *Cont. Shelf Res*.,2 147-162

Wiele, S.M., Smith, J.D., 1996. A reach-averaged model of diurnal discharge wave propagation down the Colorado River through the Grand Canyon. *Water Resour. Res.* 32: 1375-1386.

Wiele, S.M., Graf, J., Smith, J.D., 1996. Sand deposition in the Colorado River in the Grand Canyon from flooding of the little Colorado River. *Water Resour. Res.* 32(12), 3579-3596, doi: 10.1029/96WR02842.

Wilks, D.S., 2011. *Statistical methods in the atmospheric sciences*. Academic Press, 627pp.

Wright, S.A., Kaplinski, M., 2011. Flow structures and sandbar dynamics in a canyon river during a controlled flood, Colorado River, Arizona, *J. Geophys. Res. -Earth Surf., 116*, F01019.

Wright, S.A., Topping, D.J., Rubin, D.M., Melis, T.S., 2010. An approach for modeling sediment budgets in supply-limited rivers. *Water Resour. Res.* 46: W10538.

Yilmaz, K.K., Gupta, H.V., Wagener, T., 2008. A process-based diagnostic approach to model evaluation: Application to the NWS distributed hydrologic model. *Water Resour. Res.*, 44, W09417, doi: 10.1029/2007WR006716.

Zealand, C.M., Burn, D.H., Simonovic, S.P, 1999. Short-term streamflow forecasting using artificial neural networks. *J. Hydrol*. 214, 32‑48, doi:10.1016/S0022-1694(98)00242-X.

Zedler, E., Street. R., 2001. Large-eddy simulation of sediment transport: Currents over ripples. *J. Hydraul. Eng. -ASCE* 127, 444-452.

APPENDIX A

SUMMARY OF DOWNRAMP RATES STATISTICS

Table A.1. Summary of the downramp rates statistics during historic operation criteria and MLLF operation criteria from 1988 to 2009 at each of the 47 sandbar sites. River mile is referenced with respect to Lee's Ferry.

Site	Downramp rates - historic operation - 1988 to 1991				Down ramp rates - MLLF - 1997 to 2009			
River Mile	25th percentile	Median	Mean	75th percentile	25th percentile	Median	Mean	75th percentile
-6.5	0.06	0.10	0.10	0.14	0.04	0.06	0.06	0.07
1.2	0.07	0.12	0.12	0.16	0.05	0.07	0.07	0.08
2.6	0.07	0.12	0.12	0.17	0.05	0.07	0.07	0.09
8.2	0.03	0.04	0.04	0.06	0.01	0.03	0.02	0.03
16.7	0.07	0.11	0.11	0.15	0.05	0.07	0.06	0.08
22.0	0.13	0.21	0.21	0.29	0.09	0.13	0.12	0.15
23.6	0.12	0.20	0.20	0.27	0.08	0.12	0.11	0.14
29.5	0.10	0.17	0.17	0.24	0.07	0.10	0.10	0.12
30.8	0.11	0.18	0.18	0.25	0.07	0.11	0.10	0.13
31.9	0.06	0.10	0.10	0.14	0.04	0.06	0.06	0.07
32.2	0.06	0.10	0.10	0.14	0.04	0.06	0.06	0.07
33.3	0.09	0.15	0.15	0.21	0.06	0.09	0.08	0.11
35.1	0.11	0.18	0.18	0.25	0.08	0.11	0.10	0.13
41.3	0.08	0.13	0.13	0.18	0.05	0.08	0.08	0.09
43.4	0.09	0.15	0.15	0.21	0.06	0.09	0.09	0.11
44.5	0.08	0.14	0.14	0.19	0.06	0.08	0.08	0.10
45.0	0.07	0.12	0.12	0.17	0.05	0.07	0.07	0.09
47.6	0.07	0.12	0.12	0.17	0.05	0.07	0.07	0.09
50.2	0.08	0.14	0.14	0.19	0.06	0.08	0.08	0.10
51.5	0.08	0.13	0.13	0.17	0.05	0.08	0.07	0.09
55.9	0.05	0.09	0.09	0.13	0.04	0.05	0.05	0.07
56.6	0.06	0.09	0.09	0.13	0.04	0.06	0.05	0.07
62.9	0.05	0.07	0.07	0.10	0.04	0.05	0.05	0.06
65.2	0.03	0.05	0.05	0.07	0.03	0.03	0.03	0.04
66.1	0.04	0.06	0.06	0.08	0.03	0.04	0.04	0.05
68.8	0.03	0.05	0.05	0.06	0.02	0.03	0.03	0.04
81.7	0.05	0.07	0.07	0.09	0.04	0.05	0.05	0.06
84.6	0.05	0.08	0.08	0.10	0.04	0.05	0.05	0.06
87.6	0.06	0.08	0.08	0.11	0.04	0.05	0.05	0.07
88.1	0.05	0.07	0.07	0.09	0.03	0.04	0.04	0.05
91.8	0.05	0.08	0.08	0.10	0.04	0.05	0.05	0.06
93.8	0.04	0.06	0.06	0.08	0.03	0.04	0.04	0.05
104.4	0.05	0.08	0.08	0.10	0.04	0.05	0.05	0.06
119.4	0.06	0.08	0.09	0.11	0.04	0.06	0.06	0.07
122.7	0.06	0.08	0.08	0.11	0.04	0.05	0.05	0.07
123.3	0.06	0.09	0.09	0.11	0.04	0.06	0.06	0.07
137.7	0.05	0.08	0.08	0.10	0.04	0.05	0.05	0.06
139.6	0.06	0.09	0.09	0.12	0.05	0.06	0.06	0.07
145.8	0.07	0.10	0.10	0.13	0.05	0.06	0.06	0.08
167.2	0.04	0.06	0.06	0.08	0.03	0.04	0.04	0.05
172.6	0.05	0.07	0.07	0.10	0.04	0.05	0.05	0.06

183.3	0.05	0.08	0.08	0.11	0.04	0.05	0.05	0.06
194.6	0.05	0.07	0.07	0.10	0.04	0.05	0.05	0.06
202.3	0.05	0.07	0.07	0.09	0.04	0.05	0.05	0.06
213.3	0.08	0.11	0.11	0.15	0.06	0.07	0.07	0.09
220.1	0.03	0.05	0.05	0.07	0.03	0.03	0.03	0.04
225.5	0.05	0.07	0.07	0.09	0.04	0.04	0.04	0.05

APPENDIX B

DOWNRAMP RATES PRODUCED BY DISCHARGE RAMP RATES

The purpose of this appendix is to present data from downramp rates (in meters per hour) at the 47 NAU locations produced by discharge ramp rates (in cubic meter second per hour) at Glen Canyon Dam. The model used for this is referred as *the unsteady reach-averaged one dimensional model of diurnal discharge wave propagation* and it was developed by Wiele and Smith at the U.S. Geological Survey (Wiele and Smith 1996). Four case hydrograph scenarios were input to the model at Glen Canyon Dam which predicts the stage evolution of these hydrographs at the 47 sandbar locations. Daily maximums and minimums are restricted to 453 to 226.5 cms following current operation criteria (MLLF) for all case scenarios. Time at peaks also remains constant and ramp rates are the only value changing. Ramp rate at case 1 follows the restrictions to dam operation by the MLLF criteria, case 2 to case 4 exemplified possible unrestricted dam releases.

Table B.1. Hydrograph scenarios that served as input to the computational model at Glen Canyon Dam.

Hydrograph at Glen Canyon Dam	**Case 1**	**Case 2**	**Case 3**	**Case 4**
Daily maximum (cm)	453	453	453	453
Daily minimum (cm)	226.5	226.5	226.5	226.5
Time at peak (h)	8	8	8	8
Up ramp and downramp (cm/h)	43	100	200	400

Table B.2. Downramp rates (in meters per hour) at the 47 NAU locations produced by discharge ramp rates (in cubic meter second per hour) at Glen Canyon Dam.

Site (River Mile)	**Case 1 Downramp(m/h)**	**Case 2 Downramp(m/h)**	**Case 3 Downramp(m/h)**	**Case 4 Downramp(m/h)**
-6.5	0.116	0.154	0.191	0.312
1.2	0.033	0.041	0.049	0.067
2.6	0.098	0.138	0.163	0.253
8.2	0.083	0.101	0.116	0.175
16.7	0.098	0.107	0.121	0.175

22.0	0.162	0.188	0.235	0.314
23.6	0.118	0.138	0.153	0.237
29.5	0.143	0.167	0.168	0.275
30.8	0.130	0.138	0.192	0.230
31.9	0.081	0.085	0.094	0.132
32.2	0.075	0.079	0.087	0.123
33.3	0.101	0.117	0.129	0.162
35.1	0.108	0.124	0.136	0.191
41.3	0.057	0.064	0.071	0.099
43.4	0.094	0.100	0.109	0.148
44.5	0.108	0.106	0.124	0.185
45.0	0.090	0.094	0.102	0.139
47.6	0.077	0.088	0.095	0.123
50.2	0.089	0.087	0.094	0.130
51.5	0.077	0.081	0.087	0.117
55.9	0.057	0.056	0.061	0.077
56.6	0.067	0.076	0.076	0.101
62.9	0.065	0.068	0.073	0.094
65.2	0.050	0.056	0.060	0.068
66.1	0.072	0.080	0.080	0.106
68.8	0.069	0.073	0.073	0.096
81.7	0.073	0.077	0.076	0.100
84.6	0.066	0.074	0.079	0.093
87.6	0.051	0.051	0.053	0.068
88.1	0.037	0.037	0.039	0.049
91.8	0.062	0.062	0.065	0.087
93.8	0.080	0.079	0.088	0.106
104.4	0.078	0.078	0.086	0.104
119.4	0.077	0.077	0.080	0.100
122.7	0.047	0.051	0.049	0.058
123.3	0.032	0.032	0.031	0.035
137.7	0.003	0.013	0.011	0.149
139.6	0.079	0.076	0.082	0.104
145.8	0.064	0.096	0.094	0.121
167.2	0.085	0.085	0.087	0.095
172.6	0.076	0.077	0.079	0.093
183.3	0.080	0.081	0.079	0.099
194.6	0.040	0.038	0.037	0.036
202.3	0.058	0.058	0.060	0.069
213.3	0.078	0.079	0.078	0.092
220.1	0.046	0.046	0.047	0.052
225.5	0.037	0.037	0.038	0.041

APPENDIX C

DES-3D MODEL MOVIES DESCRIPTION

Animated movies display simulated videos, product of the post-processing data of the DES-3D model. These movies are an important core of this thesis since they capture the flow patterns and turbulence structures during the last 600 seconds of DES-3D model simulation. The last 600 seconds, of 1000 seconds of simulation, are used for all the results of this study. The first 400 seconds are used to spin-up the model. The tool used to animate the videos is paraFOAM. ParaFOAM is an open-source, multi-plataform, data analysis and visualization application. Briefly, the animated videos aim to show the processes of turbulent flow and vortex structures captured by coarse grid resolution versus the current grid, a comparison of near-bed and surface velocity vectors and large scales vorticity structures in the vertical and horizontal direction. The videos are discussed in detail in the manuscript. The captions are presented in this document and the videos are uploaded in separate zip files in avi format.

Video 3.1. Simulated video of instantaneous water surface velocity magnitude for the DES-3D model grid resolution (5,625,000 cells).

Video 3.2. Simulated video of the instantaneous water surface velocity magnitude for a coarser grid resolution (800,000 cells).

Video 3.3. Simulated video of the mean surface velocity vectors, in white, versus mean near-bed velocity vectors, in red, at EM eddy-fan complex. Also shown the non-hydrostatic component of the pressure. The length of mean surface velocity vectors ranges from 0 to 4.5 m/s, and the length of the near –bed velocity vectors are scaled five times larger than the surface velocity vectors.

Video 3.4. Simulated video of the mean surface velocity vectors, in white, versus mean near-bed velocity vectors, in red, at WT eddy-fan complex; Also shown the non-hydrostatic component of the pressure. The length of mean surface velocity vectors ranges from 0 to 4.5 m/s, and the length of the near –bed velocity vectors are scaled five times larger than the surface velocity vectors.

Video 3.5. Simulated video of vorticity, showing large scale vorticity structures in the vertical direction.

Video 3.6. Simulated video of the instantaneous contours of Q-criterion displayed by the velocity magnitude. Notes: Q>0 means that rotation dominates over shear stress.

Video 3.7. Simulated video of vorticity, showing large scale vorticity structures in the horizontal direction.

APPENDIX D

FORECASTING METRICS FOR MODEL VALIDATION

The purpose of this appendix is to provide an interpretation and formulation of the forecasting metrics employed to validate the model against ADCP flow measurements. Six metrics were used to validate the magnitude of the vector. These metrics are subdivided in two categories: absoluter error metrics and relative error metrics. The absolute error metrics are: (1) Mean Absolute Error (*MAE*), (2) Mean Forecast Error (*MFE*), (3) Room Mean Square Error (*RMSE*) and (4) Pearson correlation coefficient. The relative error metrics are: (5) Mean Absolute Percent Error (*MAPE*) and (6) Median Absolute Percentage Error (*MdAPE*). Furthermore, the dot product (7) was used as a metric to validate the direction of the velocity vectors. In the following paragraphs, the characteristics and formulation of these seven metrics.

Mean Absolute Error (*MAE*)

$$MAE = \frac{100}{n}\sum_{i=1}^{n}|\hat{u}_i - u_i| \tag{D.1}$$

Where: $\{\hat{u}_i\}$ is the simulated velocity magnitude, $\{u_i\}$ is the measured velocity magnitude, and $\{n\}$ the number of data (same variables applied to all metrics).

The *MAE* measures the average of the error or differences between the forecast and the corresponding field observation. The *MAE* is a linear metric where all the errors in the sample are weighted equally.

Mean Forecast Error (*MFE*)

$$MFE = \frac{1}{n}\sum_{i=1}^{n}\hat{u}_i - u_i \tag{D.2}$$

The *MFE* is a measured the average differences between simulated and observed values. The ideal value for *MFE* is 0. Negative values of *MFE* means that the model tends to over-forecast and vice versa, positive *MFE* values the model tends to under-forecast.

Root Mean Square Error (*RMSE*)

$$RMSE = \sqrt{\frac{1}{n}\sum_{i=1}^{n}(\hat{u}_i - u_i)^2} \tag{D.3}$$

The *RMSE* represents the standard deviation of the differences between the simulated and observed data. This metric is non-linear giving higher weight to large errors.

Pearson Correlation Coefficient (*R*)

$$R = \frac{\sum_{i=1}^{n}(\hat{u}_i - \overline{\hat{U}_i})(u_i - \bar{U}_i)}{\sqrt{\sum_{i=1}^{n}(\hat{u}_i - \overline{\hat{U}_i})^2}\sqrt{\sum_{i=1}^{n}(u_i - \bar{U}_i)^2}} \tag{D.4.}$$

Where $\{\overline{\hat{U}_i}\}$ is the mean of the simulated values and is $\{\overline{U_i}\}$ the mean of the observed values.

The Pearson correlation coefficient (*R*) can range from -1 to 1. A value of 1 indicates a positive linear correlation between the simulated and observed values. A value of 0 indicates no linear correlation between simulated and observed values. A value of -1 indicates a negative correlation between the variables, meaning that simulated values decrease while observed values increase.

Mean Absolute Percent Error (*MAPE*)

$$MAPE = \frac{100}{n}\sum_{i=1}^{n}\left|\frac{\hat{u}_i - u_i}{u_i}\right| \tag{D.5}$$

The *MAPE*, also known as mean absolute percentage deviation (*MAPD*) is a simple metric where the difference between the simulated and observed values and divided by the observed values and divided again by the number of points (in our case 4920). The *MAPE* value is 0% for a perfect fit but there is not upper limit restriction, large values of *MAPE* are interpreted as large errors. Nonetheless, problems occur with small or close to zero denominators causing large *MAPE* values.

Median Absolute Percent Error (*MdAPE*)

$$MdAPE = median\left(100\sum_{i=1}^{n}\left|\frac{\hat{u}_i - u_i}{u_i}\right|\right) \quad \text{(D.6)}$$

The *MdAPE* is the middle value of all the percentage errors. This metric presents the same problems of the *MAPE* metric. But it has the advantage of smoothing the effect of the outliers.

Dot Product

$$U_s \cdot U_o = \|U_s\|\|U_o\| cos\theta \quad \text{(D.7)}$$

Where U_s is defined as the Euclidean simulated velocity vector and U_o is defined as the Euclidean simulated observed vector and θ is the angle between U_s and U_o. A dot product equal to 1 indicates a perfect fit. The dot product is equal to zero when the angle between the two vectors is orthogonal (90 degrees). Finally, the dot product is equal to (-1) if the angle between the two vectors is 180 degrees. The mean value of dot product in the density function (see Table 3.1) determines the mean deviation of the direction of simulated velocity with respect to measured velocity.

APPENDIX E

SUSPENDED SEDIMENT MODEL CODE

The purpose of this Appendix is to release the code of the solver developed exclusively for the purposes of this study. Suspended sediment model code is shown below, embedded within the DES solver. The DES solver is not included since is an open-source tool of the OpenFOAM environment. IMPORTANT: This solver is not intended to be distributed as an open-source tool of the OpenFOAM environment. Other applications of this solver may incur in non-convergence. The solver was compiled in OpenFOAM 2.2.x and some modifications of the algorithm have to be done in other versions for compilation and application purposes.

```
// Concentration field solver
{
// Critical shear stress
label bedPatch = mesh.boundaryMesh().findPatchID("bed");
volScalarField xPos = mesh.C().component(vector::X);
volScalarField nuEff(turbulence->nuEff());
stress.boundaryField()[bedPatch]=nuEff.boundaryField()[bedPatch]*mag(U.boundaryField()[bedPatch].snGrad());
surfaceScalarField ca = 0*linearInterpolate(c);
forAll(ca.boundaryField()[bedPatch],faceI)
  {
      ca.boundaryField()[bedPatch][faceI]=0;
  if(stress.boundaryField()[bedPatch][faceI] >= tauc1.value() &&
mesh.boundaryMesh()[bedPatch].faceCentres()[faceI].z() >
zbedrock.boundaryField()[bedPatch][faceI]  )
```

```
// Group 1

// Calculation of ca using Smith and Mclean equation

        {

        ca.boundaryField()[bedPatch][faceI]=(0.65*0.00013*frac1.boundaryField()[bedPatch][fa
ceI]*

        ((stress.boundaryField()[bedPatch][faceI]-tauc1.value())/tauc1.value()))/

        (1+0.00013*((stress.boundaryField()[bedPatch][faceI]-tauc1.value())/tauc1.value()));

        }

   }

//Advection diffusion equation

   phis=linearInterpolate(U-ws1) & mesh.Sf();

   surfaceScalarField wsca = (ca*ws1) & mesh.Sf();

        solve

        (

           fvm::ddt(c1)

         + fvm::div(phis, c1)

         + fvc::div(wsca)

         - fvm::laplacian(turbulence->nut(), c1)

        );

//Calculation of erosion and deposition fluxes

   depo1.boundaryField()[bedPatch] =  (wsca.boundaryField()[bedPatch] +
phis.boundaryField()[bedPatch]*c1.boundaryField()[bedPatch])/
mesh.boundary()[bedPatch].magSf();


// Same procedure applied for each sediment grain size group
```

```
//Group 2

forAll(ca.boundaryField()[bedPatch],faceI)

  {

        ca.boundaryField()[bedPatch][faceI]=0;

  if(stress.boundaryField()[bedPatch][faceI] >= tauc2.value() &&
mesh.boundaryMesh()[bedPatch].faceCentres()[faceI].z() >
zbedrock.boundaryField()[bedPatch][faceI] )

        {

        ca.boundaryField()[bedPatch][faceI]=(0.65*0.00013*frac2.boundaryField()[bedPatch][fa
ceI]*

        ((stress.boundaryField()[bedPatch][faceI]-tauc2.value())/tauc2.value()))/

        (1+0.00013*((stress.boundaryField()[bedPatch][faceI]-tauc2.value())/tauc2.value()));

        }

  }

  phis=linearInterpolate(U-ws2) & mesh.Sf();

  wsca = (ca*ws2) & mesh.Sf();

        solve

        (

           fvm::ddt(c2)

         + fvm::div(phis, c2)

         + fvc::div(wsca)

         - fvm::laplacian(turbulence->nut(), c2)

        );

  depo2.boundaryField()[bedPatch] =  (wsca.boundaryField()[bedPatch] +
phis.boundaryField()[bedPatch]*c2.boundaryField()[bedPatch])/
mesh.boundary()[bedPatch].magSf();
```

```
// Group 3

forAll(ca.boundaryField()[bedPatch],faceI)

  {

        ca.boundaryField()[bedPatch][faceI]=0;

  if(stress.boundaryField()[bedPatch][faceI] >= tauc3.value() &&
mesh.boundaryMesh()[bedPatch].faceCentres()[faceI].z() >
zbedrock.boundaryField()[bedPatch][faceI] )

        {

        ca.boundaryField()[bedPatch][faceI]=(0.65*0.00013*frac3.boundaryField()[bedPatch][fa
ceI]*

        ((stress.boundaryField()[bedPatch][faceI]-tauc3.value())/tauc3.value()))/

        (1+0.00013*((stress.boundaryField()[bedPatch][faceI]-tauc3.value())/tauc3.value()));

        }

  }

  phis=linearInterpolate(U-ws3) & mesh.Sf();

  wsca = (ca*ws3) & mesh.Sf();

        solve

        (

           fvm::ddt(c3)

         + fvm::div(phis, c3)

         + fvc::div(wsca)

         - fvm::laplacian(turbulence->nut(), c3)

        );

  depo3.boundaryField()[bedPatch] =  (wsca.boundaryField()[bedPatch] +
phis.boundaryField()[bedPatch]*c3.boundaryField()[bedPatch])/
mesh.boundary()[bedPatch].magSf();
```

```
// Group 4

forAll(ca.boundaryField()[bedPatch],faceI)

  {

        ca.boundaryField()[bedPatch][faceI]=0;

  if(stress.boundaryField()[bedPatch][faceI] >= tauc4.value()  &&
mesh.boundaryMesh()[bedPatch].faceCentres()[faceI].z() >
zbedrock.boundaryField()[bedPatch][faceI] )

        {

        ca.boundaryField()[bedPatch][faceI]=(0.65*0.00013*frac4.boundaryField()[bedPatch][fa
ceI]*

        ((stress.boundaryField()[bedPatch][faceI]-tauc4.value())/tauc4.value()))/

        (1+0.00013*((stress.boundaryField()[bedPatch][faceI]-tauc4.value())/tauc4.value()));

        }

  }

  phis=linearInterpolate(U-ws4) & mesh.Sf();

  wsca = (ca*ws4) & mesh.Sf();

        solve

        (

           fvm::ddt(c4)

         + fvm::div(phis, c4)

         + fvc::div(wsca)

         - fvm::laplacian(turbulence->nut(), c4)

        );

  depo4.boundaryField()[bedPatch] =  (wsca.boundaryField()[bedPatch] +
phis.boundaryField()[bedPatch]*c4.boundaryField()[bedPatch])/
mesh.boundary()[bedPatch].magSf();
```

```
// Group 5

forAll(ca.boundaryField()[bedPatch],faceI)

  {

        ca.boundaryField()[bedPatch][faceI]=0;

  if(stress.boundaryField()[bedPatch][faceI] >= tauc5.value() &&
mesh.boundaryMesh()[bedPatch].faceCentres()[faceI].z() >
zbedrock.boundaryField()[bedPatch][faceI] )

        {

        ca.boundaryField()[bedPatch][faceI]=(0.65*0.00013*frac5.boundaryField()[bedPatch][fa
ceI]*

        ((stress.boundaryField()[bedPatch][faceI]-tauc5.value())/tauc5.value()))/

        (1+0.00013*((stress.boundaryField()[bedPatch][faceI]-tauc5.value())/tauc5.value()));

        }

  }

  phis=linearInterpolate(U-ws5) & mesh.Sf();

  wsca = (ca*ws5) & mesh.Sf();

        solve

        (

           fvm::ddt(c5)

         + fvm::div(phis, c5)

         + fvc::div(wsca)

         - fvm::laplacian(turbulence->nut(), c5)

        );

  depo5.boundaryField()[bedPatch] =  (wsca.boundaryField()[bedPatch] +
phis.boundaryField()[bedPatch]*c5.boundaryField()[bedPatch])/
mesh.boundary()[bedPatch].magSf();
```

```
depo.boundaryField()[bedPatch]=depo1.boundaryField()[bedPatch]+depo2.boundaryField()[bedPatch]+depo3.boundaryField()[bedPatch]+depo4.boundaryField()[bedPatch]+depo5.boundaryField()[bedPatch];

c=c1+c2+c3+c4+c5;

// Mixing Boundary Layer Model Grain Size Model

forAll(L1.boundaryField()[bedPatch],faceI)

{

L1.boundaryField()[bedPatch][faceI]=L1.boundaryField()[bedPatch][faceI]+depo1.boundaryField()[bedPatch][faceI]*runTime.deltaT().value()*exnerMultiplier.value();

if (L1.boundaryField()[bedPatch][faceI]<0)

{

L1.boundaryField()[bedPatch][faceI]=0;

}

L2.boundaryField()[bedPatch][faceI]=L2.boundaryField()[bedPatch][faceI]+depo2.boundaryField()[bedPatch][faceI]*runTime.deltaT().value()*exnerMultiplier.value();

if (L2.boundaryField()[bedPatch][faceI]<0)

{

L2.boundaryField()[bedPatch][faceI]=0;

}

L3.boundaryField()[bedPatch][faceI]=L3.boundaryField()[bedPatch][faceI]+depo3.boundaryField()[bedPatch][faceI]*runTime.deltaT().value()*exnerMultiplier.value();

if (L3.boundaryField()[bedPatch][faceI]<0)

{

L3.boundaryField()[bedPatch][faceI]=0;

}

L4.boundaryField()[bedPatch][faceI]=L4.boundaryField()[bedPatch][faceI]+depo4.boundaryField()[bedPatch][faceI]*runTime.deltaT().value()*exnerMultiplier.value();
```

```
if (L4.boundaryField()[bedPatch][faceI]<0)

{

L4.boundaryField()[bedPatch][faceI]=0;

}

L5.boundaryField()[bedPatch][faceI]=L5.boundaryField()[bedPatch][faceI]+depo5.boundaryFiel
d()[bedPatch][faceI]*runTime.deltaT().value()*exnerMultiplier.value();

if (L5.boundaryField()[bedPatch][faceI]<0)

{

L5.boundaryField()[bedPatch][faceI]=0;

}

if((L1.boundaryField()[bedPatch][faceI]+L2.boundaryField()[bedPatch][faceI]+L3.boundaryFiel
d()[bedPatch][faceI]+L4.boundaryField()[bedPatch][faceI]+L5.boundaryField()[bedPatch][faceI]
)>0)

{

frac1.boundaryField()[bedPatch][faceI]=L1.boundaryField()[bedPatch][faceI]/(L1.boundaryFiel
d()[bedPatch][faceI]+L2.boundaryField()[bedPatch][faceI]+L3.boundaryField()[bedPatch][faceI]
+L4.boundaryField()[bedPatch][faceI]+L5.boundaryField()[bedPatch][faceI]);

frac2.boundaryField()[bedPatch][faceI]=L2.boundaryField()[bedPatch][faceI]/(L1.boundaryFiel
d()[bedPatch][faceI]+L2.boundaryField()[bedPatch][faceI]+L3.boundaryField()[bedPatch][faceI]
+L4.boundaryField()[bedPatch][faceI]+L5.boundaryField()[bedPatch][faceI]);

frac3.boundaryField()[bedPatch][faceI]=L3.boundaryField()[bedPatch][faceI]/(L1.boundaryFiel
d()[bedPatch][faceI]+L2.boundaryField()[bedPatch][faceI]+L3.boundaryField()[bedPatch][faceI]
+L4.boundaryField()[bedPatch][faceI]+L5.boundaryField()[bedPatch][faceI]);

frac4.boundaryField()[bedPatch][faceI]=L4.boundaryField()[bedPatch][faceI]/(L1.boundaryFiel
d()[bedPatch][faceI]+L2.boundaryField()[bedPatch][faceI]+L3.boundaryField()[bedPatch][faceI]
+L4.boundaryField()[bedPatch][faceI]+L5.boundaryField()[bedPatch][faceI]);

frac5.boundaryField()[bedPatch][faceI]=L5.boundaryField()[bedPatch][faceI]/(L1.boundaryFiel
d()[bedPatch][faceI]+L2.boundaryField()[bedPatch][faceI]+L3.boundaryField()[bedPatch][faceI]
+L4.boundaryField()[bedPatch][faceI]+L5.boundaryField()[bedPatch][faceI]);
```

```
}

if ((depo.boundaryField()[bedPatch][faceI] < 0) && (Lmix.boundaryField()[bedPatch][faceI] ==
Lmax.value()))

{

Lnew.boundaryField()[bedPatch][faceI]=Lmax.value()-
(L1.boundaryField()[bedPatch][faceI]+L2.boundaryField()[bedPatch][faceI]+L3.boundaryField(
)[bedPatch][faceI]+L4.boundaryField()[bedPatch][faceI]+L5.boundaryField()[bedPatch][faceI]);

L1.boundaryField()[bedPatch][faceI]=L1.boundaryField()[bedPatch][faceI]+Lnew.boundaryFiel
d()[bedPatch][faceI]*fnew1.value();

L2.boundaryField()[bedPatch][faceI]=L2.boundaryField()[bedPatch][faceI]+Lnew.boundaryFiel
d()[bedPatch][faceI]*fnew2.value();

L3.boundaryField()[bedPatch][faceI]=L3.boundaryField()[bedPatch][faceI]+Lnew.boundaryFiel
d()[bedPatch][faceI]*fnew3.value();

L4.boundaryField()[bedPatch][faceI]=L4.boundaryField()[bedPatch][faceI]+Lnew.boundaryFiel
d()[bedPatch][faceI]*fnew4.value();

L5.boundaryField()[bedPatch][faceI]=L5.boundaryField()[bedPatch][faceI]+Lnew.boundaryFiel
d()[bedPatch][faceI]*fnew5.value();

frac1.boundaryField()[bedPatch][faceI]=L1.boundaryField()[bedPatch][faceI]/(L1.boundaryFiel
d()[bedPatch][faceI]+L2.boundaryField()[bedPatch][faceI]+L3.boundaryField()[bedPatch][faceI]
+L4.boundaryField()[bedPatch][faceI]+L5.boundaryField()[bedPatch][faceI]);

frac2.boundaryField()[bedPatch][faceI]=L2.boundaryField()[bedPatch][faceI]/(L1.boundaryFiel
d()[bedPatch][faceI]+L2.boundaryField()[bedPatch][faceI]+L3.boundaryField()[bedPatch][faceI]
+L4.boundaryField()[bedPatch][faceI]+L5.boundaryField()[bedPatch][faceI]);

frac3.boundaryField()[bedPatch][faceI]=L3.boundaryField()[bedPatch][faceI]/(L1.boundaryFiel
d()[bedPatch][faceI]+L2.boundaryField()[bedPatch][faceI]+L3.boundaryField()[bedPatch][faceI]
+L4.boundaryField()[bedPatch][faceI]+L5.boundaryField()[bedPatch][faceI]);

frac4.boundaryField()[bedPatch][faceI]=L4.boundaryField()[bedPatch][faceI]/(L1.boundaryFiel
d()[bedPatch][faceI]+L2.boundaryField()[bedPatch][faceI]+L3.boundaryField()[bedPatch][faceI]
+L4.boundaryField()[bedPatch][faceI]+L5.boundaryField()[bedPatch][faceI]);

frac5.boundaryField()[bedPatch][faceI]=L5.boundaryField()[bedPatch][faceI]/(L1.boundaryFiel
d()[bedPatch][faceI]+L2.boundaryField()[bedPatch][faceI]+L3.boundaryField()[bedPatch][faceI]
```

```
+L4.boundaryField()[bedPatch][faceI]+L5.boundaryField()[bedPatch][faceI]);

}

fractotal.boundaryField()[bedPatch][faceI]=frac1.boundaryField()[bedPatch][faceI]+frac2.boundaryField()[bedPatch][faceI]+frac3.boundaryField()[bedPatch][faceI]+frac4.boundaryField()[bedPatch][faceI]+frac5.boundaryField()[bedPatch][faceI];

}

forAll(Lmix.boundaryField()[bedPatch],faceI)

{

Lmix.boundaryField()[bedPatch][faceI]=L1.boundaryField()[bedPatch][faceI]+L2.boundaryField()[bedPatch][faceI]+L3.boundaryField()[bedPatch][faceI]+L4.boundaryField()[bedPatch][faceI]+L5.boundaryField()[bedPatch][faceI];

    diff.boundaryField()[bedPatch][faceI]=L1.boundaryField()[bedPatch][faceI]+L2.boundaryField()[bedPatch][faceI]+L3.boundaryField()[bedPatch][faceI]
+L4.boundaryField()[bedPatch][faceI]+L5.boundaryField()[bedPatch][faceI];

    diff2.boundaryField()[bedPatch][faceI]=mesh.boundaryMesh()[bedPatch].faceCentres()[faceI].z()-zbedrock.boundaryField()[bedPatch][faceI];

if(mesh.boundaryMesh()[bedPatch].faceCentres()[faceI].z()-
zbedrock.boundaryField()[bedPatch][faceI] >= Lmax.value() ||
Lmix.boundaryField()[bedPatch][faceI]>Lmax.value())

    {

    Lmix.boundaryField()[bedPatch][faceI]=Lmax.value();

    L1.boundaryField()[bedPatch][faceI]=frac1.boundaryField()[bedPatch][faceI]*Lmix.boundaryField()[bedPatch][faceI];

    L2.boundaryField()[bedPatch][faceI]=frac2.boundaryField()[bedPatch][faceI]*Lmix.boundaryField()[bedPatch][faceI];

    L3.boundaryField()[bedPatch][faceI]=frac3.boundaryField()[bedPatch][faceI]*Lmix.boundaryField()[bedPatch][faceI];

    L4.boundaryField()[bedPatch][faceI]=frac4.boundaryField()[bedPatch][faceI]*Lmix.boundaryField()[bedPatch][faceI];

    L5.boundaryField()[bedPatch][faceI]=frac5.boundaryField()[bedPatch][faceI]*Lmix.bou
```

```
ndaryField()[bedPatch][faceI];
        }
}
}
```

APPENDIX F

DES-3D SEDIMENT MODEL MOVIES DESCRIPTION

Animated movies display simulated videos, product of the post-processing data of the DES-3D sediment model. These movies are an important core of this thesis since they capture the flow and sediment patterns of DES-3D sediment model simulation. The tool used to animate the videos is paraFOAM. ParaFOAM is an open-source, multi-platform, data analysis and visualization application. Videos are referenced and discussed in detail in the manuscript. The captions are presented in this document and the videos are uploaded in separate zip files in avi format.

Video 4.1.a Simulated concentration field in EM fan eddy complex during the 10000 seconds of simulation time.

Video 4.1.b Simulated concentration field in WT fan eddy complex during the 10000 seconds of simulation time.

Video 4.2. Simulation of deposition fluxes during the 10^4 seconds of simulated time. Outlier values are removed from the simulation. The range of values (-0.0001 to 0.0001) allows a good visualization of the temporal patterns of erosion and deposition rate.